DESY 93-161
November 1993

ISSN 0418-9833

Investigations Toward the Development of Polarized and Unpolarized High Intensity Positron Sources for Linear Colliders

Dissertation
zur Erlangung des Doktorgrades
des Fachbereichs Physik
der Universität Hamburg

vorgelegt von
Klaus Flöttmann
aus Gütersloh

Hamburg
1993

Gutachter der Dissertation:	Dr. J. Roßbach Prof. Dr. E. Lohrmann
Gutachter der Disputation:	Dr. J. Roßbach Prof. Dr. Dr. h. c. G. A. Voss
Datum der Disputation:	23.11.1993
Sprecher des Fachbereichs Physik und Vorsitzender des Promotionsausschusses:	Prof. Dr. E. Lohrmann

Zusammenfassung

In der vorliegenden Arbeit werden Möglichkeiten zum Aufbau einer hochintensiven, polarisierten oder unpolarisierten Positronenquelle für Linearbeschleuniger für Hochenergie-Experimente untersucht.
Im Gegensatz zu einer konventionellen Positronenquelle, bei der hochenergetische Elektronen genutzt werden, um in einem dicken Target einen elektromagnetischen Schauer zu erzeugen, werden bei der untersuchten Quelle Photonen in einem dünnen Target konvertiert. Die Photonen werden in einem Wiggler oder Undulator generiert.
Eine Quelle diese Typs wurde 1979 von V. E. Balakin und A. A. Mikhailichenko zur Erzeugung polarisierter Positronen vorgeschlagen. Abgesehen von der Möglichkeit zur Erzeugung polarisierter Positronen bietet eine Quelle die auf der Konversion hochenergetischer Photonen beruht jedoch auch entscheidende Vorteile hinsichtlich der maximal zu erreichenden Intensitäten.
Zukünftige Linearbeschleuniger benötigen Positronenquellen, deren Intensität existierende Quellen um ein bis zwei Größenordnungen übersteigt.
Der erste Teil dieser Arbeit konzentriert sich auf das Intensitätsproblem.
Es ergeben sich folgende Vorteile für eine auf Konversion von Photonen beruhenden Quelle:

I In dem dünnen Target ist die Vielfachstreunung der Teilchen geringer, d. h. sie können mit höherer Phasenraumdichte erzeugt werden, wodurch die Einfangeffizienz um einen Faktor ~5 erhöht wird.

II Da das Target sehr dünn ist (< eine Strahlungslänge), besteht die Möglichkeit ein leichtes Targetmaterial mit hoher Wärmekapazität zu verwenden. Ein Vergleich verschiedener Materialien zeigt, daß die Positronendichte in einem Target aus einer Titan Legierung bis zu zehn mal höher sein kann als in einer Wolfram-Rhenium Legierung.

Nach der Optimierung aller Komponenten der Positronenquelle (d.h. Photonenquelle, Target und Einfang Optik), werden Parameter für eine hochintensive Quelle (bis zu $4 \cdot 10^{14}$ e^+/s) zusammengefaßt und einige Probleme des Betriebes diskutiert.
Der zweite Teil der Arbeit beschäftigt sich mit den Möglichkeiten einer polarisierten Quelle.
Zur Berücksichtigung der Vorgänge im Schauer wurde in das existierende Monte-Carlo Programm EGS 4 die Berechnung der Polarisationszustände integriert, so daß eine vollständige Simulation der polarisierten Quelle möglich ist. Techniken zur Optimierung der Positronenpolarisation werden diskutiert und verschiedene Photonenquellen miteinander verglichen. Es wird gezeigt, daß mit Hilfe eines helischen Undulators eine longitudinale Positronenpolarisation von bis zu 70% erreicht werden kann.
Da nur der auf der Undulatorachse liegende Teil der Undulatorstrahlung zirkular polarisiert ist, muß der Photonenstrahl kollimiert werden. Um eine ausreichende Positronenintensität zu gewährleisten, muß der Undulator daher ca. 150m lang sein, während für eine unpolarisierte Quelle ein leicht zu realisierender planarer Wiggler von ca. 40 m Länge genügt.

Abstract

In the present work possibilities for a high intensity, polarized or unpolarized positron source for linear colliders are investigated.
In a conventional source, high energy electrons are used as primary particles to generate an electromagnetic shower in a thick target. In contrast we consider a source, based on the conversion of high energy photons in a thin target. The photons are generated in a wiggler or undulator.
A source of this kind was invented in 1979 by V. E. Balakin and A.A. Mikhailichenko for the production of polarized positrons. Beside the possibility of generating polarized positrons, a source based on the conversion of photons offers also important advantages with respect to the maximum obtainable intensities.
Future linear colliders require positron sources, able to deliver intensities up to two orders of magnitude higher than existing sources.
The first part of this paper deals with the intensity problem.
The following advantages arise for a source based on photon conversion:

I The multiple-scattering of the particles is reduced in the thin target, hence the positrons are produced with higher phase-space density and the capture efficiency is increased by a factor of ~5.

II Since the target is thin (< one radiation length), one is able to use a low Z material with high heat capacity. A comparison of various materials shows that the positron density in the target can be up to an order of magnitude higher in a titanium-alloy target than in a tungsten-rhenium-alloy target.

After optimizing all components of the source (i.e. photon source, target and capture optics), parameters of a high intensity positron source (up to $4 \cdot 10^{14}$ e+/s) are summarized. Problems of the source operation are discussed.

The second part of the paper concerns the possibilities of a polarized source. In order to take care of the processes in the shower, the calculation of polarization states has been introduced into the already existing Monte-Carlo program EGS 4, so that a complete simulation of the polarized source is possible. Techniques for the optimization of the positron polarization are discussed and various photon sources are compared. It is shown that a longitudinal positron polarization of up to 70% can be reached by means of radiation of a helical undulator.
Since only the on-axis part of the undulator radiation is circularly polarized, the photon beam has to be collimated. In order to reach a sufficient positron yield, the length of the helical undulator has to be roughly 150m, while for the unpolarized source a simple planar wiggler of roughly 40 m length is sufficient.

Contents

Introduction

Future lepton colliders have to reach the energies above 300 GeV center-of-mass. Due to the strong synchrotron radiation losses in storage rings, a circular collider for these energies would be excessively large and expensive. To overcome these problems, linear colliders are investigated as an alternative concept. Somewhat different approaches are studied from groups, working on JLC (KEK), NLC (SLAC), VLEPP (BINP), CLIC (CERN), DESY/THD and TESLA. An overview of these projects is given in ref. 1.

In order to reduce the power consumption, linear colliders have to work in a pulsed mode with a repetition rate between 10 Hz and 1.7 kHz. During one rf-pulse up to 800 electron bunches and positron bunches will be accelerated in two linear accelerators, respectively, and brought into collision at the interaction point. The center-of-mass energy envisaged for the first stage of operation ranges from ~300 Gev (above LEPII) up to 500 GeV. Later it might be increased to 1 TeV and 1.5 TeV, respectively.

The high energy physics potential of linear colliders is governed by the search of the top quark, the Higgs boson and supersymmetric particles. Details can be found in ref. 38.

A common feature of all linear colliders is the requirement of a huge number of particles per second which have to be delivered from the particle sources. Source requirements of the above mentioned projects and, as reference, of the SLC project are collected in table 1.

	SLC	JLC	NLC	VLEPP	CLIC	DESY/ THD	TESLA
Ne^+/pulse [10^{10}]	5	80	63	20	0.6	360	4000
number of bunches per pulse	1	70	90	1	1	172	800
bunch spacing [ns]	-	2.8	1.4	-	-	12	1000
rep. rate [Hz]	120	150	180	150	1700	50	10

Tab. 1 Source requirements of various linear collider projects

Even if a part of the particles can be collected and recycled after the collision [ref. 2, 3], the requirements for the positron sources are still above the current SLC source at SLAC which is, up to now, the positron source with the highest intensity.

A strong limit for the intensity of positron sources is given by the thermal stress which is built up in the conversion target due to the energy deposition of the pulsed primary beam.

The superconducting TESLA proposal requires the highest positron intensity of all linear collider designs. However, due to the large bunch spacing, the thermal load problems in the target can be relaxed by means of a rotating target-wheel [ref. 4, 5]. Hence the thermal load problems are more critical for the S-band approach of DESY/THD where $3.6 * 10^{12}$ positrons per pulse with 50 Hz repetition frequency are required [ref. 6].

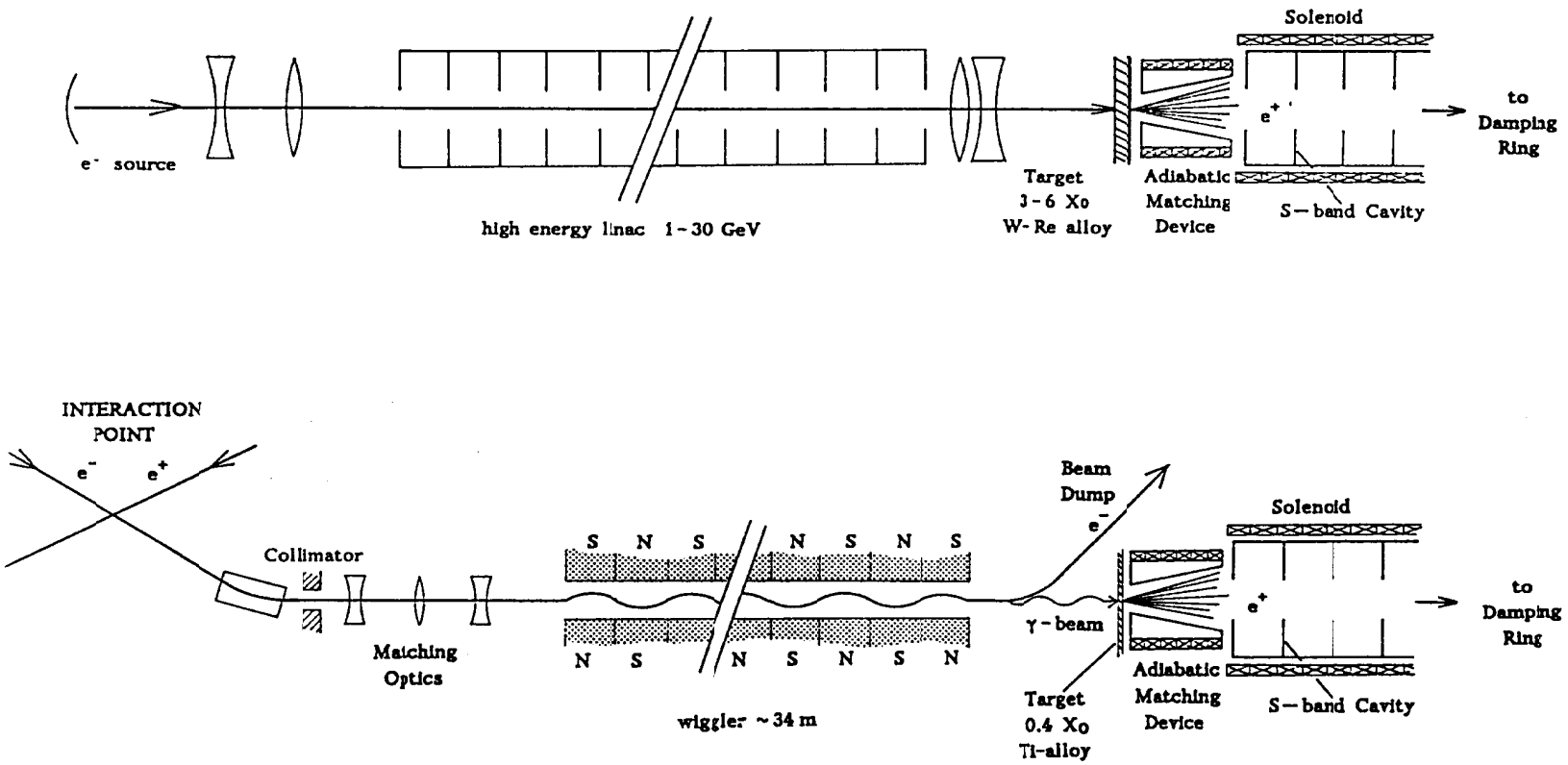

Fig. 1. 0 Schematic layout of a positron source based on conventional technology and of a source based on wiggler radiation

At SLAC a 33 GeV electron beam strikes a 6 radiation length thick target of high Z material (W - Re - alloy). Per incident electron more than 50 positrons are generated [ref. 7] from which only one is captured, accelerated and transmitted into the damping ring, so that the over all efficiency $e^+/e^- \sim 1$.
Numerical calculations show that a maximum temperature of 720^0 C will be reached, if $7 * 10^{10}$ electrons strike the rotating target; nearly 8 kW thermal energy would be deposited in this case (120 Hz rep. rate). Due to stress estimations the maximum allowable intensity is limited to $5.3 * 10^{10}$ electrons per pulse [ref. 8].
In the present paper a scheme is investigated which is based on a proposal of V.E. Balakin and A.A. Mikhailichenko for the production of polarized positrons [ref. 9]. A similar idea was proposed in ref. 10.
The schematic layout of the source is shown in fig. 1.0. The 250 GeV electron beam is used after the collision as a primary beam. Due to the strong beam-beam forces very intense γ-radiation is generated during the collision process called beamstrahlung. This results in a considerable energy spread within each bunch after the collision. However, typically more than 70% of the particles are still within a bandwidth of $\pm 3\%$. After travelling through a special matching optics [ref. 2, 11], the beam emittance is still small enough to pass the subsequent wiggler section. Here photons with a mean energy of ~20 MeV are emitted into a narrow cone which will be converted into electron-positron pairs inside the target, while the primary electrons are deflected by a dipole magnet. Before the positrons can be accelerated, they have to be captured in a matching optics, the so called adiabatic matching device. This part of the source is similar to that of a conventional source. The positrons have to be stored for a short time (some ms) in a damping ring (at E = 3-5 GeV), in order to reduce the emittance by means of radiative damping, before they can be accelerated in the main linac and brought into collision with the opposite electron beam.
Beside the possibility to generate polarized photons inside the undulator which are converted into polarized positrons, undulator or wiggler radiation can also be used to design a high intensity source which is able to fullfill the requirements of the DESY/THD proposal [ref. 11, 12].
In the proposed scheme a very thin target (< one radiation length) can be used. Thermal load problems in the target are reduced due to two effects:

- one is able to use a low Z material with high heat capacity
- the divergence of the positron beam is small, hence one gets a high capture efficiency of the optics behind the target.

The first part of this paper concentrates on problems connected with a high intensity source. Our standard electron beam energy will be 250 GeV except for ch. 1.6.3 where the operation at various energies will be discussed. In ch. 1.6 design parameters for an unpolarized DESY/THD source and a TESLA source will be given. The second part of the paper deals with the possibilities of a polarized source.

1.0.0 A high intensity positron source based on wiggler radiation

After a brief discussion of the effects in electromagnetic cascades, the influence of the photon spectrum on the positron spectrum will be investigated. In the following chapter suitable target parameters will be determined, while the first elements of the optics behind the target will be optimized in ch. 1.5.

1.1.0 Properties of electromagnetic cascades

A high energy photon passing through a material can create an electron positron pair in the field of a nucleus (pair production). These charged particles again lose energy on their way through the material via collision and radiation processes. The collisions account for the majority of heat deposition in the material, while photons generated by radiation processes i. e. bremsstrahlung, may once more produce electron positron pairs. This sequence continues, i. e. the total number of electrons, positrons and photons increases exponentally in a material, while the mean energy of the particles decreases. However, the development of the shower is limited due to the ionization losses. Therefore the electromagnetic cascade begins to decay if the mean energy of the particles drops below a critical energy Ec. Ec is the energy where:

$$-\frac{dE}{dx}_{brems} = -\frac{dE}{dx}_{ion}$$

is fullfilled. We find:

$$Ec \sim 10\,MeV \quad \text{for lead, see fig. 1.3}$$

Pair production and bremsstrahlung are essentially inverse processes (see Feynman graphs fig. 2.2), hence they can be characterized by a common parameter called the radiation length X_0. The connection of this parameter with the cross section of the processes will be discussed below. Here we emphasize the meaning of the radiation length from a more phenomenological point of view:
Within a distance of one radiation length, a photon creates on the average a pair, while an electron or positron loses all but a fraction of 1/e of its energy due to bremsstrahlung.
The radiation length values of various materials can be found in tables (e.g. ref. 15) and are approximatively given by:

$$X_0^{-1}[\,cm\,]^{-1} = \frac{4\alpha N_A}{A} * Z(Z+1)\,r_e^2 \ln(183\,Z^{-1/3}) * \rho$$

$N_A \equiv$ Avogadro' s number
$A \equiv$ atomic weight
$Z \equiv$ atomic charge
$r_e \equiv$ classical electron radius
$\alpha = 1/137$
$\rho \equiv$ density of the material

Since, for important electromagnetic processes (bremsstrahlung, pairproduction Coulomb scattering), some or all of the dependence upon the medium is contained in the radiation length, it is convenient to measure the target thickness in terms of radiation length. Then the shower development is to first order of approximation independent of the material.

1.1.1 Photon interactions

Photons interact with material mainly through three processes: photoelectric effect (τ), Compton scattering (σ_{INCOH}) and pair production (K_n). The photon cross section as a function of the photon energy in a low Z material (carbon) and a high Z material (lead) are plotted in Fig. 1.1. We are interested in energies above 2 MeV where pair production takes place.
The Compton scattering cross section is still high between 2 and 10 MeV (for the low Z material), however, its influence on the shower properties is small. It will be disscused in more detail in ch. 2.3.2 in connection with polarization effects.
Pair production is a mechanism whereby a photon is completely absorbed and an $e^+ e^-$ - pair is produced.

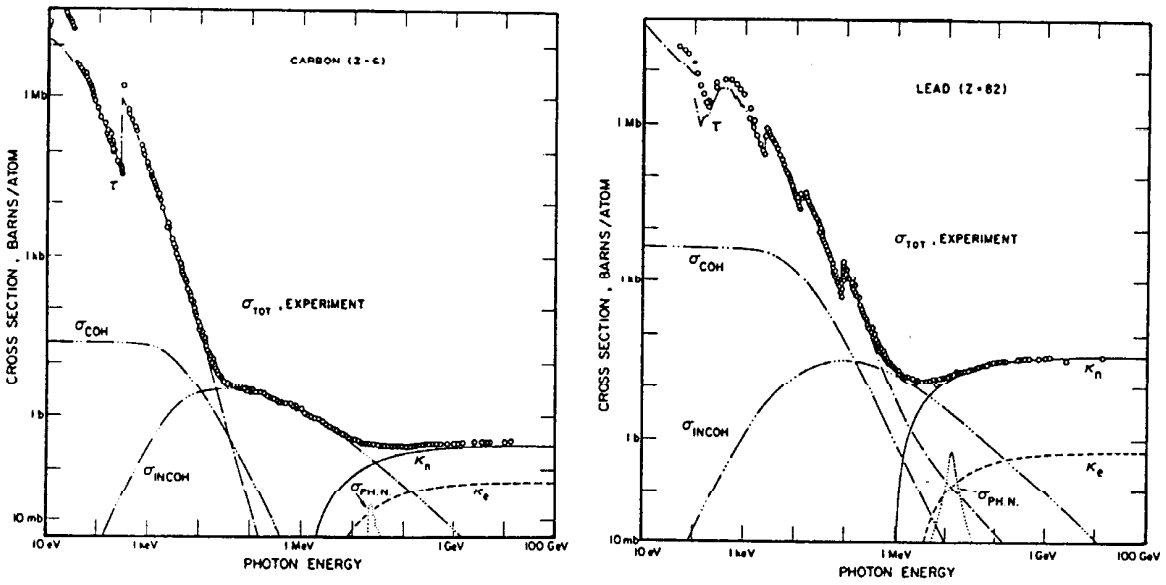

Fig. 1.1 Photon total cross section as a function of energy in Carbon and Lead [ref. 58]

τ	=	atomic photo-effect
σ_{COH}	=	coherent scattering (Rayleigh scattering)
σ_{INCOH}	=	incoherent scattering (Compton scattering)
K_n	=	pair production, nuclear field
K_e	=	pair production, electron field
$\sigma_{PH.N.}$	=	photonuclear absorption

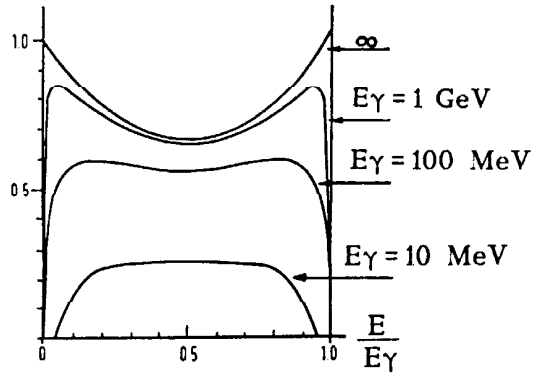

Fig. 1.2 Energy distribution for $e^+ e^-$ pairs as a function of the fractional energy $E/E\gamma$

The cross section for pair production is constant for high energies. Multiplying the number of atoms per unit volume $n = \rho * N_A/A$ with the high energy limit of the pair production cross section σ_P one obtains the probability of a pair creation by a high energy photon within a material layer of thickness x:

$$P = 1 - e^{-x n \sigma_P}$$

which can also be written as:

$$P = 1 - e^{-\frac{7x}{9 X_0}}$$

Hence we get:

$$n \sigma_P = \frac{7}{9} * X_0^{-1} \qquad (1.1)$$

Fig. 1.2 shows the probability of finding the electron or positron with the fractional energy $E/E\gamma$ for various photon energies $E\gamma$. The particles are roughly equally distributed between 0 and $E\gamma$ except for very low and extremely high photon energies.
Another important process, called the giant resonance in nuclear physics, is described by the photon-neutron cross section $\sigma_{PH.N.}$ in Fig. 1.1. This cross section is small compared to the pair production, however, it leads to an induced radioactivity in the target which is a problem particularly for high intensity sources. We will discuss this topic in more detail in ch. 1.6.4.

1.1.2 *Electron interactions*

During the bremsstrahlung process the electron loses in most cases only a small fraction of its energy, in contrast to the pair production where the photon is completely absorbed. Hence the energy loss as function of the energy is a more convenient function for the characterization of electron interactions than the cross section.
The probability $\frac{\Phi(E,k)}{dx\,dk}$ that a high energy electron ($E \gg m_0c^2 \cdot Z^{-1/3}$) will emit a photon of energy k, while passing through a material layer of thickness dx, is given by:

$$\frac{\Phi(E,k)}{dx\,dk} = \frac{1}{X_0} \cdot \frac{1}{k} \cdot F(E,k)$$

$$F(E,k) \simeq 1 + \left(\frac{E-k}{E}\right)^2 + \frac{2}{3}\left(\frac{E-k}{E}\right)$$

Hence the spectrum of bremsstrahlung photons has roughly a 1/k shape.
The average total energy loss per path length dx for a high energy electron follows from:

$$-\frac{dE}{dx} = \int_{k=0}^{E} \frac{\Phi(E,k)}{dx\,dk} \cdot k\, dk$$

to be

$$-\frac{dE}{dx} \simeq \frac{E}{X_0}$$

This is also shown in fig. 1.3, where the fractional energy loss per radiation length for collision and radiation processes in lead is plotted.

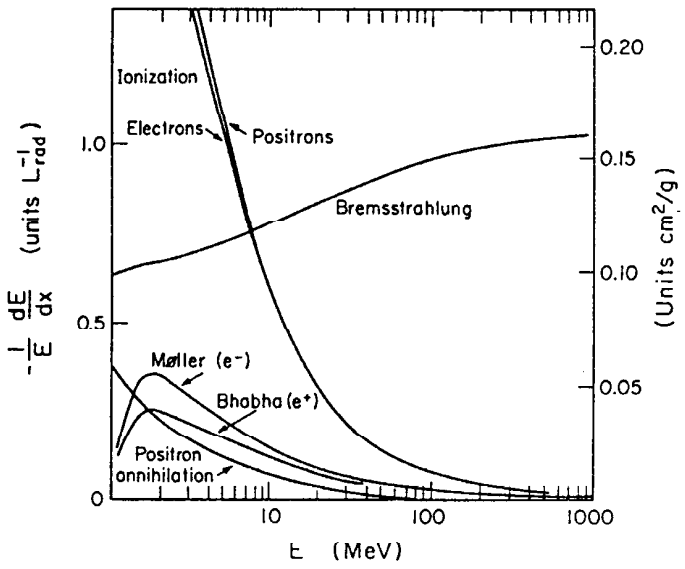

Fig. 1.3 Fractional energy loss per path length dx in units of radiation length in lead versus electron and positron energy, respectively [ref. 59].

The energy loss for bremsstrahlung per radiation length is, in the high energy limit, independent of the material. Thus, as already mentioned, the electron or positron loses on the average all but a fraction of 1/e of its energy within one radiation length.
Møller scattering, Bhaba scattering and positron annihilation can be neglected for our purpose.
The ionisation loss scales like $1/\beta^2$ ($\beta = v/c$) for energies below ~1 MeV, so that charged particles with energies below 1 MeV lose their energy nearly instantaneously.
Above ~2 MeV the ionization loss is independent of the energy and given by $\Delta\varepsilon \leq 2$ MeV cm^2/g. (The loss is roughly independent of the material. Detailed values for various materials are given in ref. 13.) The loss per radiation length is then obtained by:

$$\Delta E\,[\,\mathrm{MeV}\,] = \Delta\varepsilon\,[\,\mathrm{MeV\,cm^2/g}\,] * \rho\,[\,\mathrm{g/cm^3}\,] * X_0\,[\,\mathrm{cm}\,] \qquad (1.2)$$

Since X_0 scales like $(Z^2 * \rho)^{-1}$ the ionization loss per radiation length becomes larger for a low Z material.
In addition to the energy loss caused by ionization (i.e. soft collisions), hard collisions with atomic nuclei lead to multiple scattering and a lateral spread of the shower. (The contibutions of other processes like Compton scattering, pair production, bremsstrahlung etc. to the lateral spread out are negligiblly small.) The theory of multiple scattering has been worked out by Molière [ref. 14] and extensions and improvements have been treated by various authors.
According to ref. 15 the rms-scattering angle for a charged particle traversing a medium is:

$$\Theta_{rms} = \frac{19.2\,[\,\mathrm{MeV}\,]}{\beta\,E} * \sqrt{\frac{s}{X_0}}\;\left[\,1 + 0.2\ln\left(s/X_0\right)\,\right] \qquad (1.3)$$

s ≡ path-length of the particle in the material

If we compare targets with the same thickness in units of the radiation length, we find Θ_{rms} to be independent of the material. But the rms-displacement of a particle at the end of the target due to multiple scattering is given by:

$$y_{rms} = \frac{1}{\sqrt{3}} * \Theta_{rms} * s \qquad (1.4)$$

Thus the rms-displacement of the particles scales with the geometrical target thickness rather than with the radiation length.

1.2.0 Characteristics of undulator and wiggler radiation

In the proposal of V.E. Balakin and A.A. Mikahilichenko [ref. 9] helical undulator radiation was used to generate polarized positrons. Our emphasis in this section is more on high positron intensities rather than polarization. Hence we can use a planar wiggler for the photon generation which is much easier and less expensive to build but produces no longitudinally polarized photons. Alternatively we can use a helical undulator with parameters (i.e. field and period length) chosen unrestricted by polarization considerations. The advantage of helical undulator radiation is that compared to wiggler radiation more high energy photons are produced which can then be converted into pairs.
Hence we first try to estimate the positron spectrum for various undulator parameters and also for a planar wiggler.

1.2.1 Radiation of a planar wiggler

A planar wiggler consists of a row of short dipole magnets with constant field strength but alternating field direction. For a large period length λw (λw[cm] * B[T] >> 1) the photon number spectrum, $dN_{ph}/d\xi$, of the radiation can be approximated by means of the well known spectrum radiated by an electron in a dipole magnet:

$$\frac{d\,N_{ph}}{d\,\xi}\,[\,m^{-1}\,] = B\,\frac{e\,\alpha\,\sqrt{3}}{2\,\pi\,m\,c}\int_{\xi}^{\infty} K_{5/3}(\xi)\,d\xi$$

$$\xi = \frac{2\,\rho\,\omega}{3\,c\,\gamma^3}$$

$\omega \equiv$ frequency of radiation
$\rho \equiv$ radius of electron path in the dipole magnet
$\gamma \equiv$ relativistic γ factor of the electron
$K_{5/3} \equiv$ modified Bessel function

1.2.2 Radiation of a helical undulator

A helical undulator is a device in which the electrons pass through a transverse magnetic field whose direction revolves around the beam axis. Owing to the field pattern given by:

$$\mathbf{B}(z) = B\left[\,\cos\left(\frac{2\pi z}{\lambda u}\right),\ \sin\left(\frac{2\pi z}{\lambda u}\right),\ 0\,\right]$$

$\lambda u \equiv$ undulator period

the electron moves on a spiral trajectory.
The helical field may be produced by a pair of conducters wound to a double helix, as sketched in fig. 1.4. When currents in opposite directions are passed

through the two conductors, the central axial magnetic field is cancelled and the spiralling transverse field pattern appears.

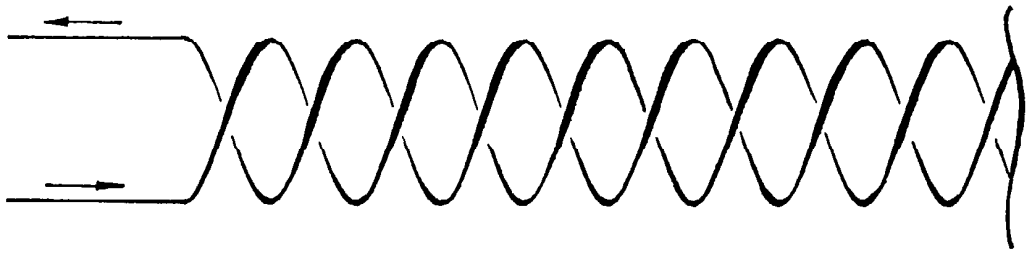

Fig. 1.4 Principle layout of a helical undulator

The radiation spectrum of a moving charge is calculated by means of the Lienard-Wiechert integral [ref. 16]:

$$I(\omega, \Omega) = \frac{d^2 I}{d\omega\, d\Omega} = \frac{e^2 \omega^2}{16 \pi^3 \varepsilon_0 c} \left| \int_{-\infty}^{+\infty} \mathbf{n} \times (\mathbf{n} \times \boldsymbol{\beta}(t))\, e^{i\omega\left(t - \frac{\mathbf{n}\, \mathbf{r}(t)}{c}\right)}\, dt \right|^2 \qquad (1.5)$$

$\mathbf{n}$ = unit vector in direction of observation

Ω ≡ solid angle

$\mathbf{r}(t)$ ≡ electron trajectory

$$\boldsymbol{\beta}(t) = \frac{d\mathbf{r}(t)}{dt} * \frac{1}{c}$$

Introducing the dimensionless parameter K

$$K = \frac{e}{2 \pi m_0 c} * B * \lambda u = 0.934 * B[T] * \lambda u[cm] \qquad (1.6)$$

the electron trajectory is given by:

$$\mathbf{r}(t) = \left[r \sin\left(\frac{2\pi \bar{\beta} c}{\lambda u} t\right),\ r \cos\left(\frac{2\pi \bar{\beta} c}{\lambda u} t\right),\ \bar{\beta} c t \right]$$

with

$$\bar{\beta} = \beta \left(1 - \frac{K^2}{\gamma^2}\right)^{1/2}$$

$$r = \frac{K \lambda u}{2 \pi \gamma}$$

i. e. the electron moves with a constant velocity $\bar{\beta} * c$ in z direction while it describes a circle with radius r.

K is the pitch angle of the electron trajectory.

The radiation spectrum of an undulator is determined by the two independent parameters λu and B or by the more convenient parameter set K and E_1:

$$E_1 = \hbar \omega_1 = \hbar \frac{4 \pi \gamma^2 c}{(1 + K^2)\, \lambda u} \qquad (1.7)$$

The K-value of the undulator determines the shape of the radiation spectrum, while the energy of the first harmonic E_1 defines the scaling of the energy axis.

The photon number spectrum for a helical undulator integrated over the solid angle is [ref. 17]:

$$\frac{dN_{ph}}{dE}\left[\frac{1}{m\ MeV}\right] = \frac{10^6 e^3}{4\pi\varepsilon_0 c^2 \hbar^2} * \frac{K^2}{\gamma^2} \sum_{n=1}^{\infty} \left(J'_n(x)^2 + \left[\frac{\alpha_n}{K} - \frac{n}{x}\right]^2 J_n(x)^2 \right) \qquad (1.8)$$

the sum has to be evaluated only for

$$\alpha_n^2 = \left[n * \frac{\omega_1 (1+K^2)}{\omega} - 1 - K^2 \right] \geq 0$$

$$x = 2 * K * \frac{\omega}{\omega_1 (1+K^2)} * \alpha_n$$

J_n = Bessel functions

In fig. 1.5 the photon spectrum of a helical undulator is plotted for various K - values, as well as the photon spectrum of a strong planar wiggler.

Substituting $\frac{\omega}{\omega_1 (1+K^2)} = \frac{E}{E_1 (1+K^2)} = r$ one finds:

$$\frac{dN_{ph}}{dr} = \frac{10^6 e^3}{4\pi\varepsilon_0 c^2 \hbar^2} * \frac{K^2}{\gamma^2} * E_1 (1+K^2) \sum_{n=1}^{\infty} \left(J'_n(x)^2 + \left[\frac{\alpha_n}{K} - \frac{n}{x}\right]^2 J_n(x)^2 \right)$$

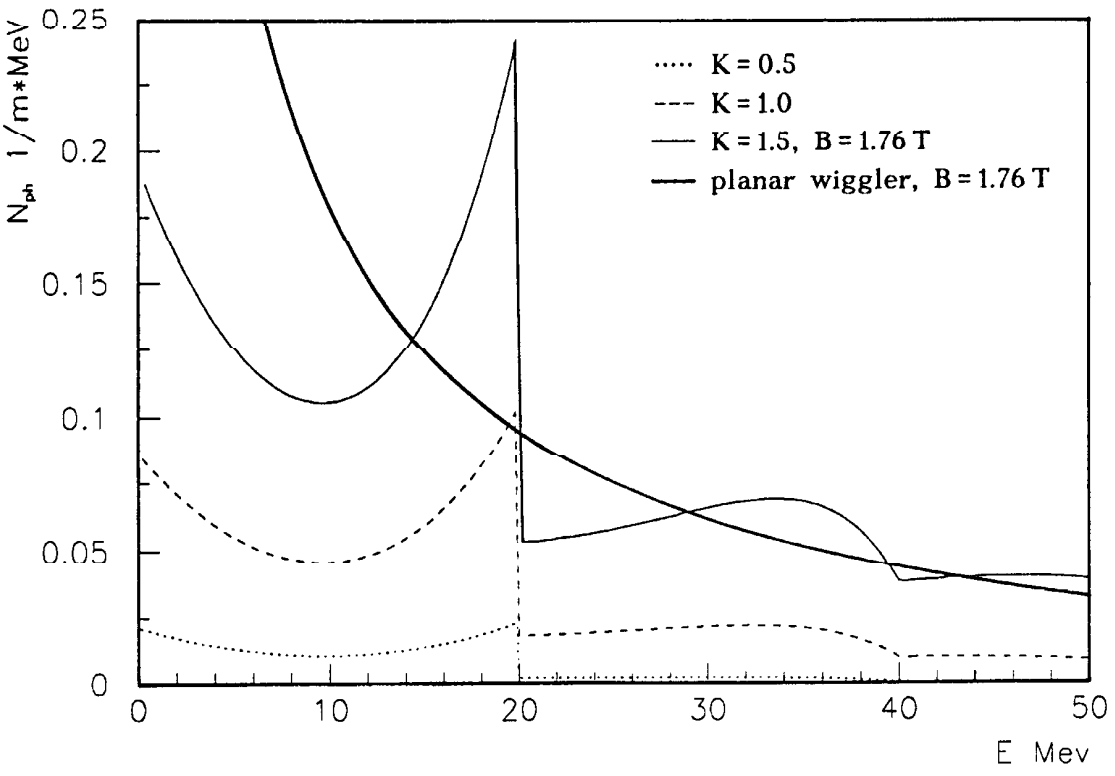

Fig. 1.5 Photon number spectrum for helical undulators and a planar wiggler, E = 250 GeV. We will discuss the spectrum of a helical undulator in more detail in ch. 2.6.0.

It follows that the total number of photons $N_{ph} = \int_0^\infty \frac{dN_{ph}}{dE} dE$ is:

- linear in E_1
- and, since E_1 is proportional to γ^2, independent of γ (λ_u fixed).

The sum depends only weakly on K, therefore we derived from our numerical results the approximated formula for the total photon production:

$$N_{tot}\left[\frac{1}{m e^-}\right] = \int_0^\infty \frac{dN_{ph}}{dE} dE \simeq 10^3 * (14.36 - 2.78 * K) * K^2 (1 + K^2) * \frac{E_1 [eV]}{\gamma^2}$$

$$\simeq (3.56 - 0.69 * K) * K^2 / \lambda_u [cm] \qquad (1.9)$$

for $0 < K \leq 3$

A comparison of this approximation with numerical results is shown in fig. 1.7.

1.3.0 Influence of the photon spectrum on the positron spectrum

In order to investigate the influence of the photon spectrum on the positron spectrum we can use a simple model for the pair production. The advantages of this crude approximation which will later be confirmed by Monte-Carlo calculations are: (1) it is much faster than any Monte-Carlo approach and (2) it allows to separate effects of the photon spectrum from effects of the shower, like particle loss due to ionisation and bremsstrahlung etc. .

The positron production by one photon of energy E in a thin target ($t < 1$) can be approximated by the linear expression:

$$N_{e^+}(E) = S(E) * t$$

t = target thickness in units of radiation length

$$S(E) = K_n * \rho * N_A/A * X_0$$

S(E) represents the probability for the positron production per radiation length (K_n = cross section for pair production see fig. 1.1). K_n is approximated by the function [ref. 11]:

$S(E) = 0$	for $E \leq 1.6$ MeV
$S(E) = 0.14 \ln(1.5\ E[MeV]) - 0.117$	for 1.6 MeV $< E < 400$ MeV
$S(E) = 7/9$	for $E \geq 400$ MeV

Assuming that the positrons produced by photons with energy E_γ are equally distributed over the energy range from 0 to E_γ, which is a good approximation only for $E_\gamma \geq 10$ MeV, one finds the positron spectrum by :

$$\frac{dN_{e^+}(E_0)}{dE} = \int_{E_0}^\infty \frac{dN_{ph}}{dE} * \frac{1}{E} * S(E)\, dE * t$$

Fig. 1.6 shows the resulting positron spectrum for two different photon spectra,

namely for the undulator spectrum with B = 1.76, $\lambda u = 0.9$ cm, K = 1.5 (solid line, energy of the first harmonic $E_1 = 20$ MeV) and for a wiggler with B = 1.76 T. The wiggler produces more low energy positrons which are difficult to collect in the subsequent optics but contribute to the thermal stress of the target. The difference between the spectra is however amazingly small.

The dependence of the positron production on the parameter K for a helical undulator is plotted in fig. 1.7. The energy of the first harmonic is fixed at $E_1 = 20$ MeV.

The three lines show the total photon production $N_{ph\,tot} = \int_0^\infty \frac{dNph}{dE}\,dE$, the total positron production $N_{e+\,tot} = \int_0^\infty \frac{dNe+}{dE}\,dE$ and the positron production in the energy range from 2 to 20 MeV $Ne+ = \int_2^{20} \frac{dNe+}{dE}\,dE$ which is the energy acceptance of the SLC source.

While the three lines increase with increasing K-values the conversion efficiency $N_{e+\,tot}/N_{ph\,tot}$ and even the ratio of the positron production in the range 2 - 20 MeV to the total production decreases.

In order to minimize the thermal stress in the target, the capture efficiency of the subsequent optics which is related to the ratio $N_{e+\,tot}/N_{e+}$ is an important factor.

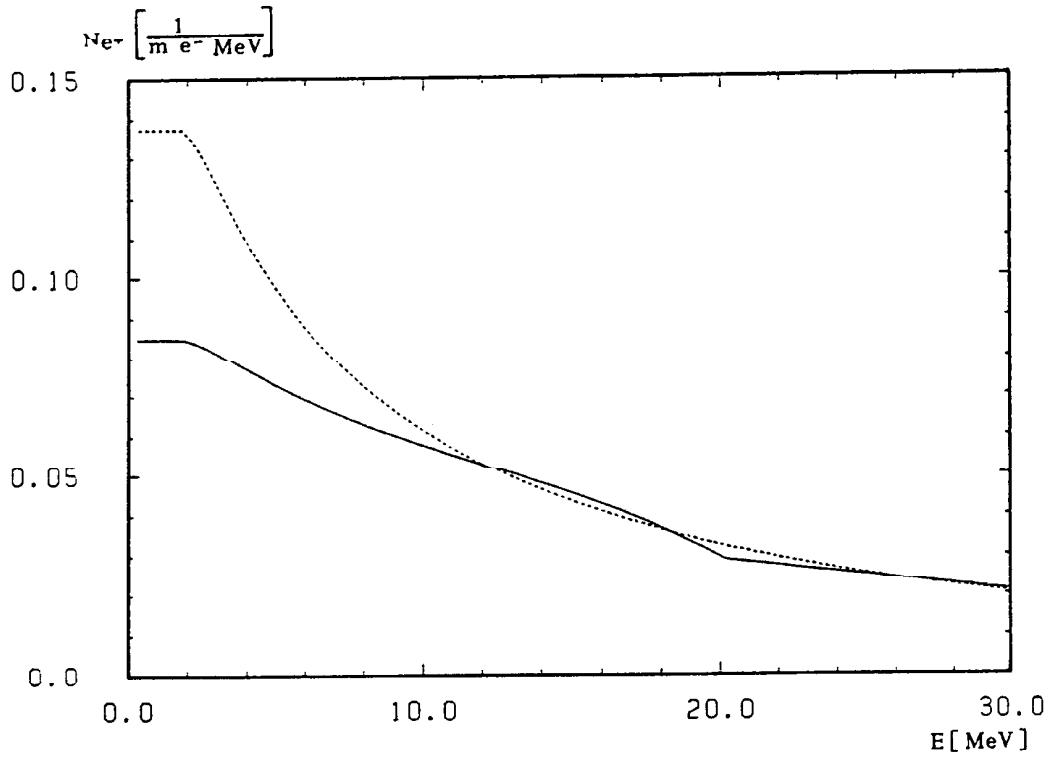

Fig. 1.6 Estimated positron spectra for a wiggler with B = 1.76 (dotted line) and a helical undulator with B = 1.76 T, $\lambda u = 0.9$ cm (solid line) at 250 GeV

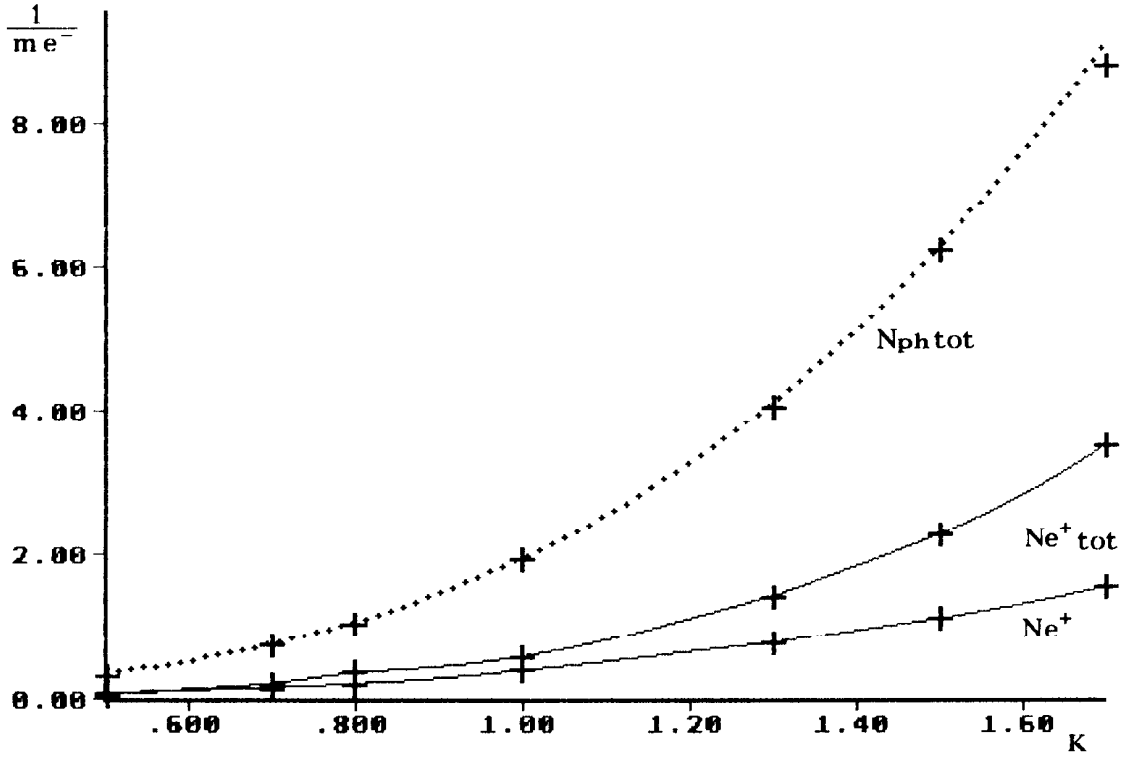

Fig 1.7 Dependence of the photon production and the positron production per radiation length on the parameter K, E_1 = 20 MeV, E = 250 GeV; dotted line: approximation according to eq. 1.9

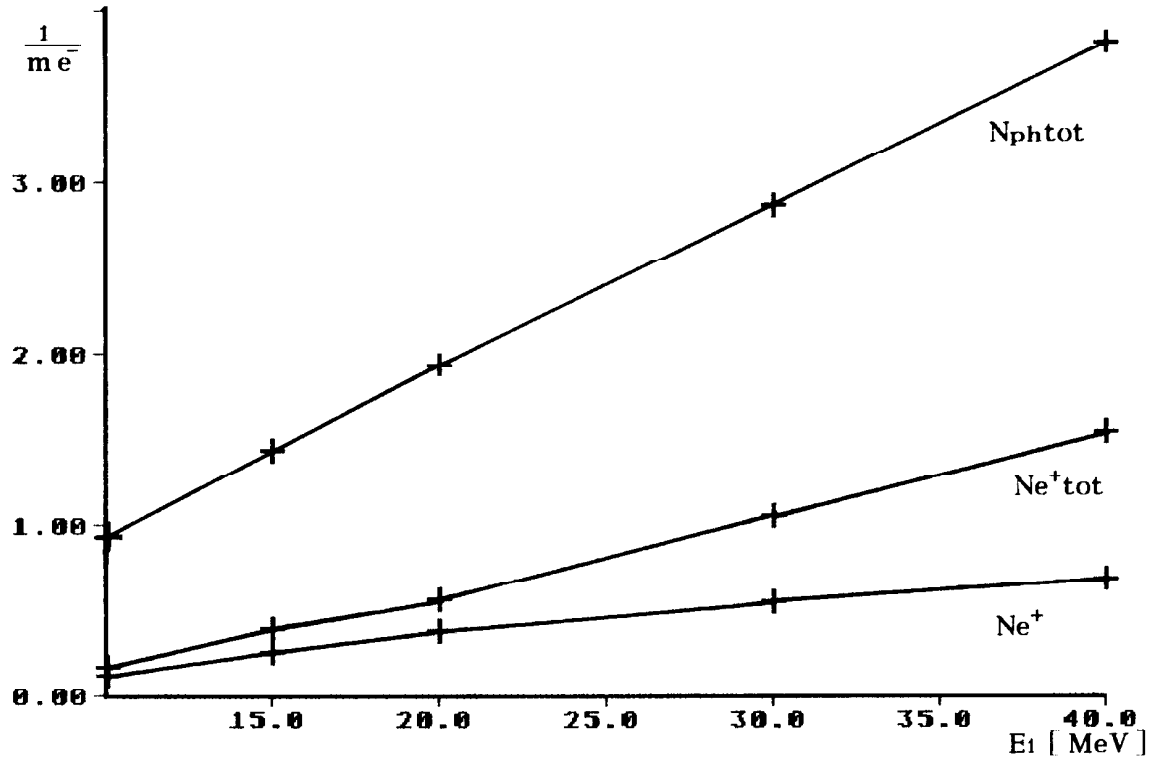

Fig. 1.8 Dependence of the positron production per radiation length on E_1; K = 1, E = 250 GeV

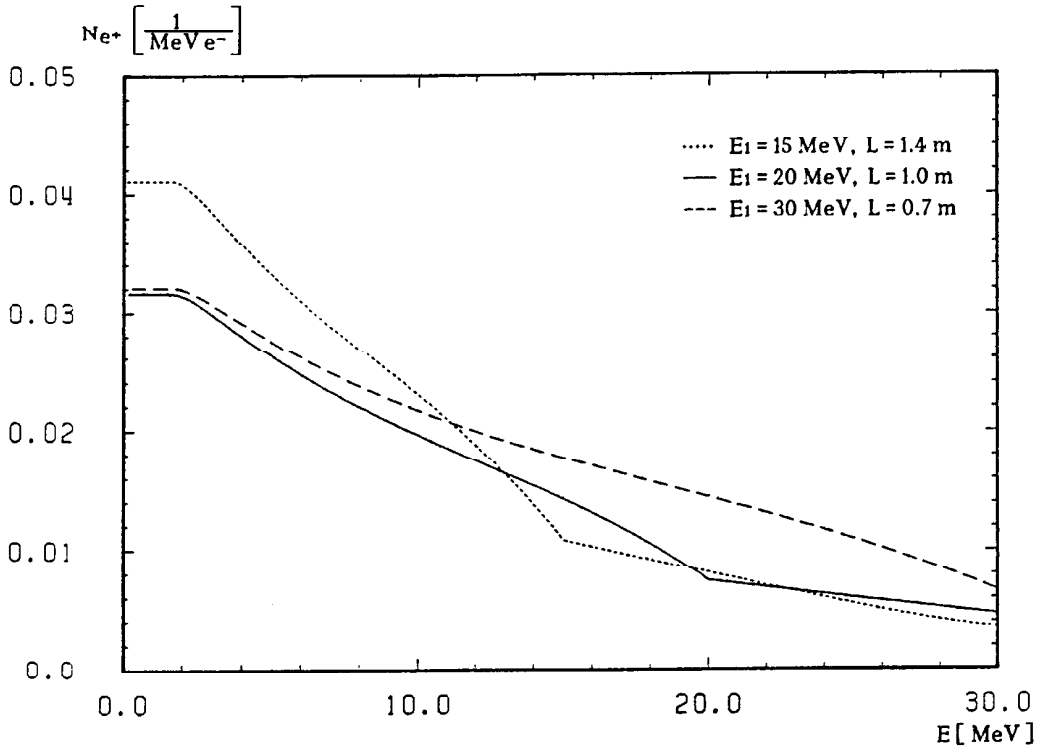

Fig. 1.9 Positron spectra for various E_1; K = 1, E = 250 GeV

Fig. 1.8 and fig. 1.9 show plots for the variation of the energy of the first harmonic E_1 with fixed K-value: K = 1.
To get a good impression of the influence of E_1 on the spectrum of the positrons, the length L of the undulators has been varied, so that the amount of positrons in the range between 2 and 20 MeV is the same for the three cases plotted in fig. 1.9.
The positron spectra indicate that there are too many low energy positrons at low K-values and at low energies E_1. Low energy positrons, as well as high energy positrons well above 20 MeV (very high K or E1), will not be collected in the subsequent optics.
However, for technical reasons one will anyway be limited to parameters of $B \leq 1.8$ T, $\lambda_u \geq 0.5$ cm, i.e $K \approx 1.5$, $E_1 \approx 20$ MeV.
For the detailed calculation of the electromagnetic shower the Monte-Carlo code EGS 4 was used [ref. 18]. See ch. 2.2.1 for a description of the program.

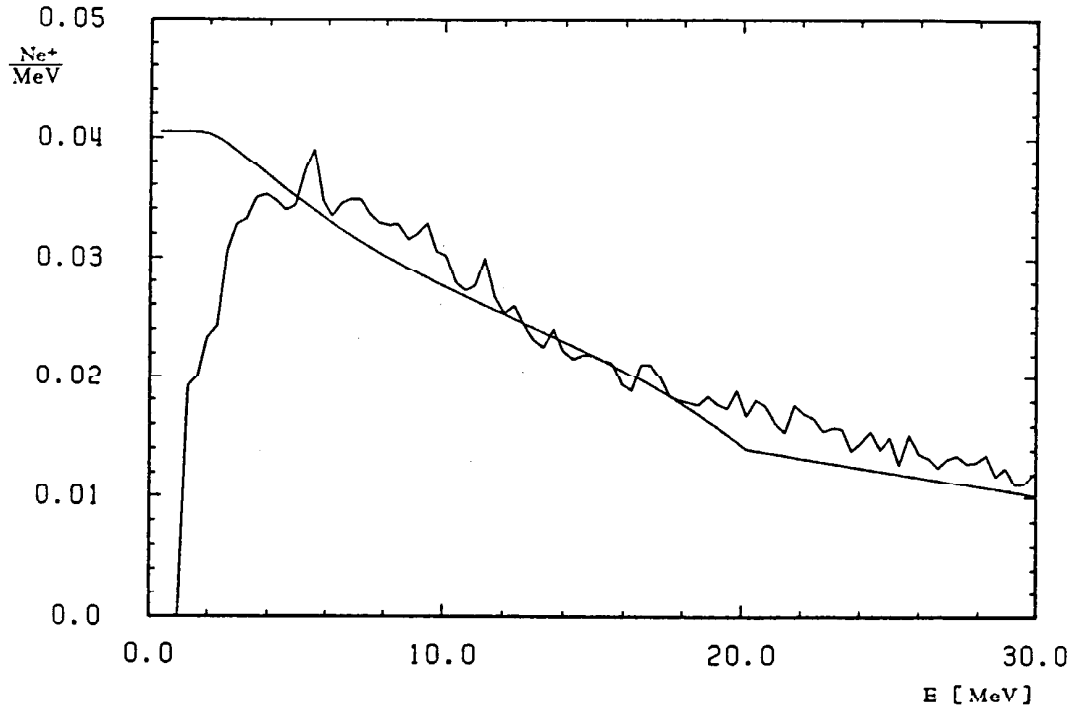

Fig. 1.10 Comparison of positron spectra calculated by means of the approximative method and by means of the shower code EGS 4

In fig. 1.10 a spectrum obtained with the approximative method is compared with results as given by EGS 4. Both curves are normalized to $\int_0^\infty \frac{d\,Ne^+}{dE}\,dE = 1$, otherwise the Monte-Carlo results would be below the approximative curve. The approximative approach tends to overestimate the total positron yield due to the lack of particle losses. The shape of the spectrum, however, is in good agreement with the Monte-Carlo results, except for energies below ~3 MeV where the increasing ionisation losses cause strong particle loss.
Hence we can conclude that a high intensity positron source can be built either with a strong planar wiggler ($B \approx 1.7$ T) or with a strong helical undulator. The energy of the first harmonic of the undulator should be between 15 MeV $\leq E_1 \leq$ 25 MeV and the K-value can be as high as 1.5.

1.4.0 The target and related thermal load problems

The most severe problem for the target of a high intensity source is the mechanical stress which is introduced in the target due to the deposited energy of the shower.
The problem can be relaxed by means of a rotating target.
Since the repetition rate of linear colliders is between 10 Hz and 1700 Hz (see table 1), subsequent shots can easily be separated on the target, so that the maximum temperature rise occurs within one shot. In case of TESLA it is even possible to spread out the bunch train of 800 bunches over a distance of the target, as will be discussed later. For all other projects the energy deposition of the bunches within a bunch train will add up in the target. Since this happens much faster than thermal relaxation processes, it can be regarded as an instantaneous energy deposition.
The heating of the target is mainly determined by the ionisation loss of the charged particles which is approximately $\Delta\mathcal{E} \simeq 2\,\mathrm{MeV\,cm^2/g}$ per particle. (Contributions of other processes like Compton scattering to the enrgy deposition in the target are negligible small.)
Hence, the energy deposited by one charged particle in a target of thickness s is (eq. 1.2):

$$E[\mathrm{J}] = 2 * 10^{6}\left[\frac{\mathrm{eV\,cm^2}}{\mathrm{g}}\right] * 1.6 * 10^{-19} * \rho\left[\frac{\mathrm{g}}{\mathrm{cm^3}}\right] * s\,[\mathrm{cm}]$$

In order to get N positrons, $2 * N * \eta$ particles (electrons and positrons) have to emerge from the target. The factor η describes the overproduction which is necessary to compensate the limited efficiency of the capture optics behind the target. Thus the temperature rise in the target per pulse can be estimated at:

$$\Delta T[\mathrm{K}] = \frac{2 * N * \eta * 2 * 10^{6} * 1.6 * 10^{-19} * \rho * s}{c * \rho * A * s} \sim \frac{N}{A} * \frac{1}{c} * \eta \qquad (1.10)$$

c ≡ heat capacity $\left[\frac{\mathrm{J}}{\mathrm{g\,K}}\right]$

A ≡ source area $[\mathrm{cm^2}]$

We will compare this estimation with numerical results in ch. 1.4.2.
There are three more or less free parameters which determine the temperature:

- the heat capacity of the target material c
- the efficiency of the capture optics $1/\eta$
- the source area A

An increased source area counteracts a high capture efficiency, because it lowers the phase-space density of the particles emerging from the target. This will be discussed in ch. 1.5, while in the following chapter suitable target parameters will be determined.

1.4.1 Choice of target material

A conventional positron source requires a target of many radiation lengths thickness for the full development of the electromagnetic shower. Low energy positrons which are produced in the first steps of the cascade will not emerge from the target due to the ionization losses inside the material. The ionization loss per radiation length depends on the material and is lower for high Z materials. If we consider a reference particle of 10 MeV we can calculate the maximum depth from which the particle reaches the end of the target (bremsstrahlung is neglegted; eq. 1.2):

$$S_{escape} / X_0 = \frac{10\ [\mathrm{MeV}]}{2\ \left[\frac{\mathrm{MeV\,cm^2}}{\mathrm{g}}\right] \cdot \rho\left[\frac{\mathrm{g}}{\mathrm{cm^3}}\right] \cdot X_0\,[\mathrm{cm}]}$$

Material	Z	S_{escape}/X_0
W	74	0.74
Cu	29	0.39
Ti	22	0.31
Al	13	0.21

Tab. 2 Escape depth for a reference particle of 10 MeV for various materials

As seen from table 2 low energy particles can emerge from a thicker layer (in units of X_0) in high Z materials. Thus one *must* use a high Z material in conventional sources in order to get a sufficiently high positron yield.
In thin targets, however, the conversion efficiency is to first order independent of the material, hence it is possibile to use a low Z material. Thermal load problems are in general somewhat relaxed in low Z materials, due to the higher heat capacity (Dulong-Petit-rule).
In fig. 1.11 the positron yield Y_{e^+}, i.e. the total number of positrons emerging out of the target, for a 1 m long wiggler is plotted for various materials. For thicknesses above 0.5 X_0 the yield function has a broad maximum before it decreases.
A strong planar wiggler was used as the photon source in fig. 1.11. For a helical undulator with equal magnetic field the yield would be ~ 6% higher for a 0.4 X_0 target.
The yield for low Z materials is only 10% — 20% worse compared to tungsten, hence we have at our disposal a large choice of target materials. In order to find a suitable target material we will discuss mechanical stress, cooling properties and thermal load of the target in the next subsections.

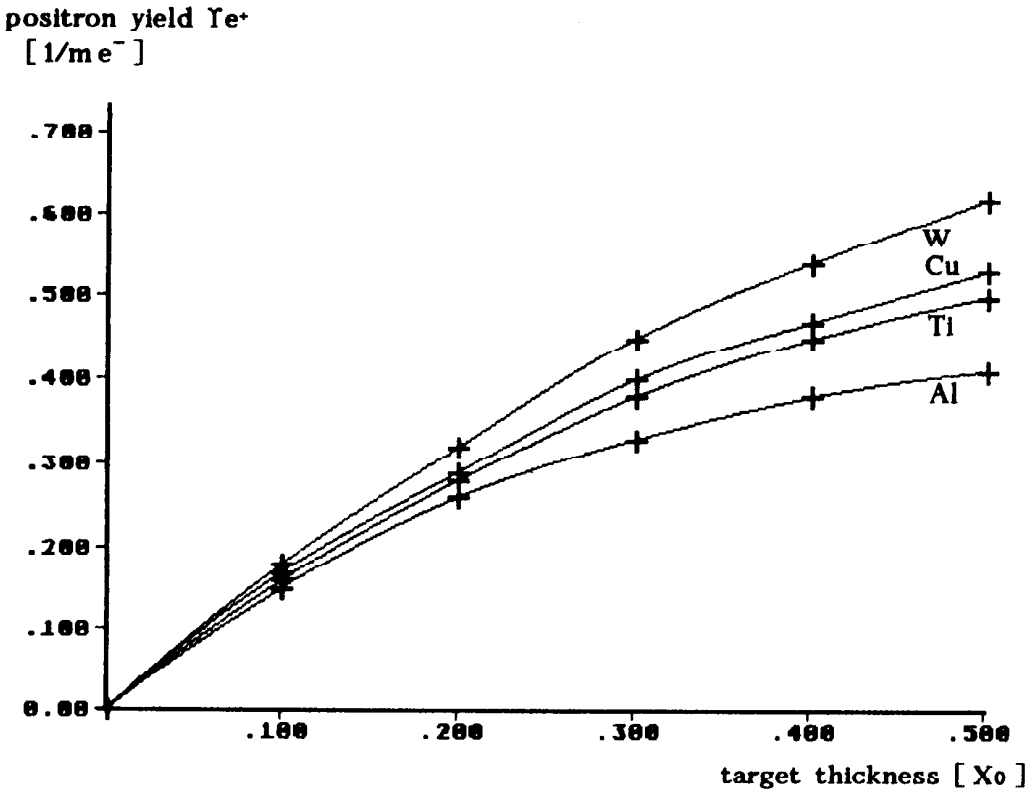

Fig. 1.11 Positron yield for various materials obtained with wiggler photons (B = 1.7 T, S = 1 m) versus target thickness in units of radiation length; E = 250 GeV

1. 4. 2 Mechanical stress

The stress introduced in the target due to the thermal load depends on the final mechanical design of the target (boundary conditions) and can in detail only be calculated by means of numerical methods (e.g. the finite-element-method). This has been done at SLAC for a tungsten-rhenium-alloy target [ref. 8].

In order to compare different materials, however, it is convenient to combine material constants with respect to their proportionality to the mechanical stress Pt, induced by heating:

$$P_t \sim \Delta T \, \alpha \, E$$

α = coefficient of linear expansion $[K^{-1}]$

$E \equiv$ elastic modulus $[N\ m^{-2}]$

For example the radial stress P_r of a circular plate with fixed boundaries which is uniformly heated up by a temperature difference of ΔT is given by:

$$P_r = -\Delta T \frac{\alpha E}{1-\mu}$$

$\mu \equiv$ poisson ratio $\mu \leq 0.5$

The poisson ratio μ is defined as the ratio of the lateral contraction $\Delta d/d$ to the linear strain $\Delta l/l$:

$$\mu = \frac{\Delta d/d}{\Delta l/l}$$

μ connects the elastic modulus with the bulk modulus K and the modulus of rigidity G:

$$K = \frac{E}{3(1-2\mu)}$$

$$G = \frac{E}{2(1+\mu)}$$

Since μ depends only weakly on the material (a typical value is $\mu=0.3$), it is sufficient for our purpose to concentrate on the tension stress.

We set:

$$\Delta T_{max} \sim \frac{1}{c} \cdot \hat{\rho} \qquad \text{(see eq. 1.10)}$$

c ≡ heat capacity

$\hat{\rho}$ is the maximum particle density at the target exit. In the radial direction it refers to the center of the distribution.
Hence we get:

$$P_{t\,max} \sim \frac{\alpha E}{c} \cdot \hat{\rho}$$

$P_{t\,max}$ denotes the maximum stress which occurs in the target. We define a specific stress $P_{t\,sp}$ which contains the material dependence:

$$P_{t\,sp} = \frac{\alpha E}{c}$$

and get:

$$P_{t\,max} \sim P_{t\,sp} \cdot \hat{\rho}$$

Now we substitute $P_{t\,max}$ with the maximum allowable stress $P_{0.2}$, called the 0.2% yield strength, which is the stress where the material deformation ceases to be elastic. (For many materials only data for the ultimate tensile strength are obtainable which, in general, is only slightly higher than $P_{0.2}$.)
We get:

$$\hat{\rho} \sim \frac{P_{0.2}}{P_{t\,sp}}$$

In table 3 material constants and the ratio $P_{0.2} / P_{t\,sp}$ are summarized for an assortment of different materials.

The ratio $P_{0.2} / Pt_{sp}$ is up to an order of magnitude larger for a titanium alloy than for the tungsten alloy used at SLC, i.e. the particle density of the positrons emerging from the target can be up to an order of magnitude higher in a thin titanium target than in a thick tungsten target, while the yield is only about 16% less. Good experience with these materials has been made at SLAC where titanium alloys are used in high power scrapers and collimators [ref. 13, 19].
We have extended our material comparison only on commercially available alloys up to now, however, new high temperature materials on the basis of titanium-aluminide and titanium-silicide are currently under investigation in several laboratories. They might increase the ratio $P_{0.2}/Pt_{sp}$ above the values obtainable with conventional alloys in the near future.

Material	c	α $*10^{-6}$	E $*10^{11}$	$P_{0.2}$ $*10^{7}$	$\frac{P_{0.2}}{Pt_{sp}}$	ρ	λ	$\frac{\lambda}{c\,\rho}$	Tmelt
W	0.14	4.4	3.45	41.0	38	19.3	163.0	60.3	3360
W-26RE	0.13	5.0	4.00	91.0	60	-	-	-	-
Cu	0.39	16.0	1.20	40.0	80	9.00	384.0	111.0	1083
Ti	0.52	8.4	1.16	55.0	294	4.54	15.5	7.0	1665
Ti-5Al-2.5Sn	0.52	9.3	1.17	86.3	412	4.46	7.3	3.0	1550
Ti-13V-11Cr-3Al	0.62	8.8	0.98	96.1	691	4.82	7.5	2.5	-
Al	0.99	23.1	0.73	25.0	148	2.7	233.0	86.0	659

Tab. 3 Comparison of material constants. Most properties are functions of the temperature, but only a few of them were measured at high temperatures (W, W-26RE: colum 1-4; T = 1000 K, all others at room temperature). The temperature dependence of the ratio $P_{0.2} / Pt_{sp}$, however, is somewhat depressed due to the similar behaviour of the elastic modulus and the 0.2% yield strength.
(c = heat capacity J/gK; α = coefficient of linear expansion K^{-1}; E = elastic modulus N/m^2; $P_{0.2}$ ≡ 0.2% yield strength N/m^2; ρ ≡ density g/cm^3; λ ≡ coefficient of heat conductivity W/m K; Tmelt ≡ melting-point °C.)

1.4.3 Thermal load problems

In a thin target the number of charged particles increases roughly linearly from the beam entrance to the beam exit. Therefore we can estimate the energy deposition $E_{dep(z)}$ per positron emerging from the target as a function of the longitudinal coordinate z in the target to be:

$$E_{dep(z)}\left[\frac{MeV}{e^+ cm}\right] = 2 * 2\left[\frac{MeV cm^2}{g}\right] * \rho\left[\frac{g}{cm^3}\right] * \frac{z}{s}$$

where s denotes the target thickness (factor 2 for the electrons accompanying the positrons).
The density ρ is smaller for low Z materials but the geometrical target thickness is much larger, hence the total energy deposition is larger in light materials, even though the temperature rise is less.
Fig. 1.12 shows a comparison between this simple model and results obtained with the EGS4 code for a tungsten and a titanium target. (For comparison the longitudinal coordinate was scaled to the respective radiation length.)

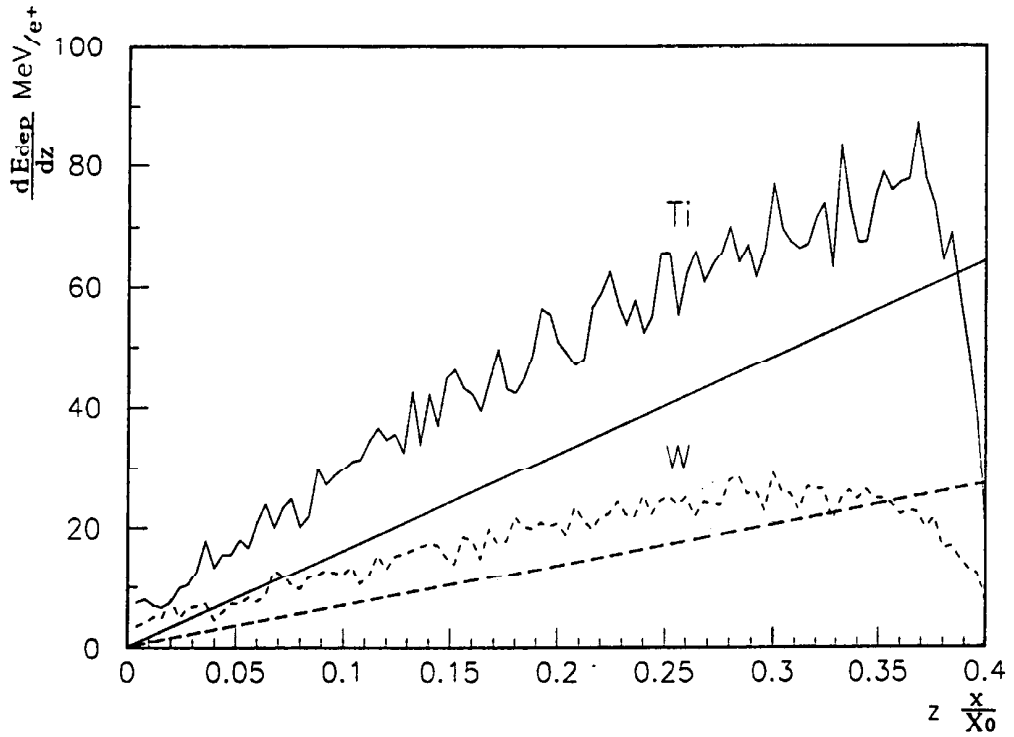

Fig. 1.12 Energy deposition per positron as a function of the longitudinal coordinate (in units of X_0) in the target for tungsten and titanium

The longitudinal distribution of the deposited energy is well approximated by the simple model. An interesting result of the EGS calculations is the decreasing energy deposition at the end of the target, where the particle density reaches its maximum. During an ionisation process energy is transferred to knock-on electrons which perform a random walk while they deposit their energy. At the border of the target the knock-on electrons can leave the target, thus the energy deposition is reduced.
In addition to the calculation of the longitudinal energy deposition the total deposited energy was calculated by means of EGS. Results, scaled to 10^{14} positrons emerging from the target, are shown in table 4. The simple analytic model underestimates the total energy deposition by some ten percent.

Material	total deposited energy per 10^{14} positrons [J] target thickness: 0.2 Xo	0.4 Xo
W	52	110
Ti	127	295

Tab. 4 Total deposited energy in a tungsten and a titanium target for different target thicknesses

For a given material the maximum temperature rise is proportional to the maximum positron density of the shower which depends on the distribution of the oncoming γ-beam and of the scattering in the target.
While the rms-scattering angle scales with the target thickness in units of the radiation length (eq. 1.3), the lateral spread of the primary beam in the target scales with the geometric thickness of the target (eq. 1.4) and hence

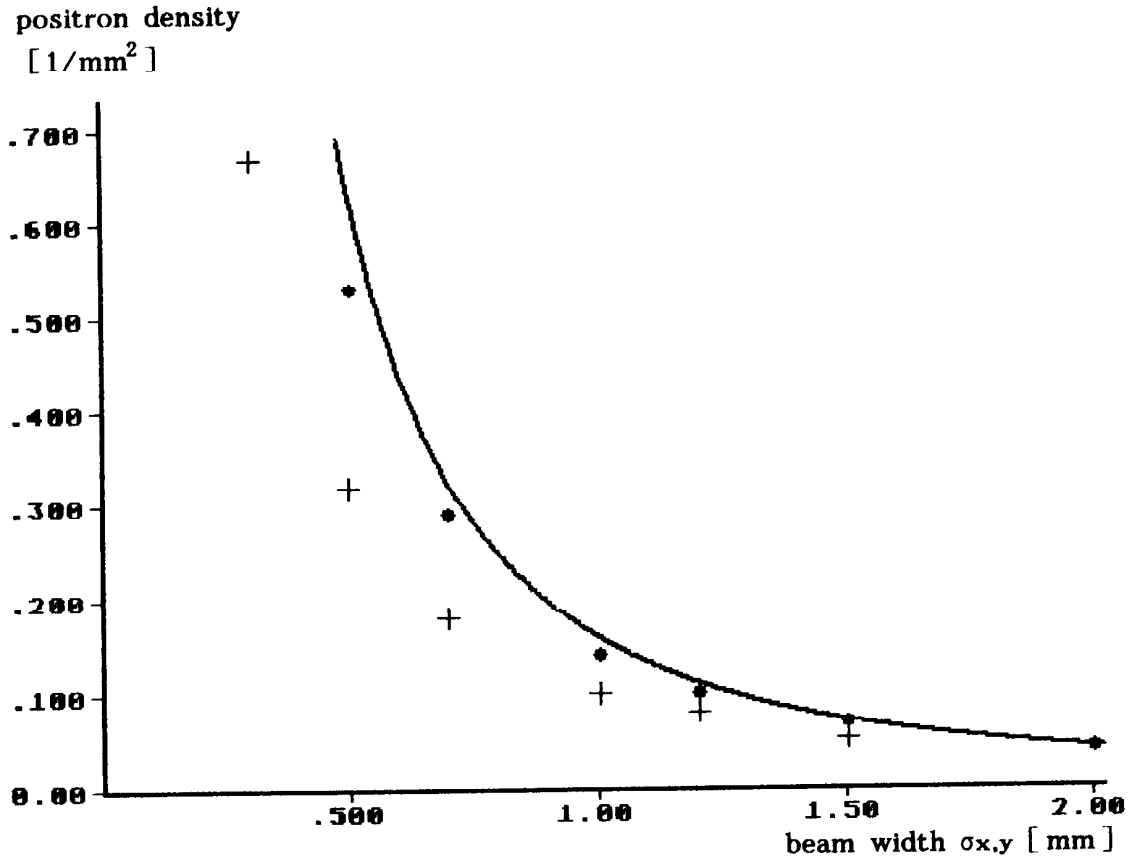

Fig. 1.13 Maximum positron density per positron at the target exit versus beam width for titanium (+) and tungsten (*) (target thickness 0.4 Xo)

is larger for a low Z material. This effect reduces the phase-space density of the positrons emerging from the target. However, if a high positron yield is required, the source area is not limited due to multiple-scattering but is due to the maximum allowable particle density in the target which determines the maximum temperature rise.

The particle density of the positrons as a function of the spot size ($\sigma x = \sigma y$) of the oncoming γ beam is plotted in fig. 1.13. Results of an EGS calculation with a point like γ-beam have been used. Gaussian-distributed random numbers with various sigmas have been added to the radial coordinate of the outgoing positrons, so that the particle density in the center of the distribution could be extracted from a histogram plot.

Fig. 1.13 shows the particle density scaled to one positron emerging from the target for various sigmas and different materials (target thickness 0.4 X_0). The solid line shows the density that would be expected if there were no scattering in the target. For small sigmas the scattering is more dominant, hence there is a large difference between titanium and tungsten which vanishes for larger sigmas, i.e. to obtain a given particle density of positrons emerging from the target the spot size of the γ-beam has to be somewhat smaller for titanium than for tungsten.

To estimate the maximum allowable particle density inside the titanium target, we scale numerical calculations which where performed by E. M. Reuter et al. for the SLC positron source [ref. 8].

The geometric proportions of the SLC target (6 X_0 tungsten-rhenium-alloy $\hat{=}$ 2.1 cm) are comparable to a thin titanium target (0.4 X_0 titanium $\hat{=}$ 1.42 cm), while the longtudinal temperature gradient would be much higher in the case of a thin tungsten target (0.4 X_0 tungsten $\hat{=}$ 0.14 cm), i.e. the longitudinal gradient would be of the same order of magnitude as the radial gradient in this case.

The maximum allowable temperature ΔT calculated in ref. 8 for the SLC target was about $\sim$ 700 K. Hence the maximum positron density $\hat{\rho}+$ can be estimated to be:

$$\hat{\rho}+ = \frac{\Delta T * c}{2 * 2 * 10^6 * 1.6 * 10^{-19}} = 1.4 * 10^{14} \left[\frac{e^+}{cm^2} \right]$$

c $\equiv$ heat capacity

In titanium alloys the heat capacity is a factor of $\sim$5 larger. In addition, the material can withstand the stress of a larger temperature rise, so that in total the particle density can be up to an order of magnitude higher (see tab. 3). However, for safety reasons we choose only a factor of 5. Therefore the maximum positron density will be:

$$\hat{\rho}+ = 7 * 10^{14} \left[\frac{e^+}{cm^2} \right] \qquad (1.11)$$

which leads to a maximum temperature rise of:

$$\Delta T_{max} = 720 \text{ K.}$$

1. 4. 4 Heat flux properties of the target material

In order to find characteristic parameters for the cooling of the target, we consider the stationary heat flux through a cylindrical wall which is given by:

$$\dot{Q} = 2\pi * L * \lambda * \Delta T * \ln \frac{r_o}{r_i}$$

L ≡ length of the cylinder
λ ≡ coefficient of heat conductivity $\left[\frac{W}{m\,K}\right]$
r_o/r_i ≡ outer/ inner radius of the cylinder
ΔT = temperature difference

During a shot (t = 0) the cylinder is uniformly heated, by a temperature ΔT_o:

$$\Delta T_o = \frac{Q_0}{c * \rho * \pi * r_i^2 * L}$$

Q_0 = total deposited energy

Thus we get:

$$\dot{Q}_{t=0} = \frac{2 * \lambda * Q_0}{c * \rho * r_i^2} * \ln \frac{r_o}{r_i}$$

The total heat flux to the enviroment is given by $Q(t) = \int_0^t \dot{Q}(t)\, dt$. We find:

$$Q(t) = Q_0 \left(1 - e^{-\frac{t}{t_o}}\right)$$

with $$\frac{1}{t_0} = \frac{2 * \lambda}{c * \rho * r_i^2} * \ln \frac{r_o}{r_i}$$

The temperature of the target is given by:

$$T(t) = T_0\, e^{-\frac{t}{t_o}}$$

Therefore the cooling of the target is characterised by the parameter $\frac{\lambda}{c * \rho}$ which should be as high as possible. Material constants are summarized in table 3. The cooling capability of titanium is more than an order of magnitude less than that of tungsten. This, however, is not a principle problem, since even in the case of a tungsten target a rotation of the target is necessary to avoid a superposition of subsequent shots on the target. The time for cooling is then given by the circumference and the rotational speed of the target wheel, i.e the titanium target has to be larger than a comparable tungsten target.

More details of the cooling of the target will be discussed in ch. 1.6.

In this chapter we have shown that titanium alloys are suitable materials for the thin target of a wiggler based positron source. We have estimated that the maximum positron density in the target is $\hat{\rho}+ = 7 * 10^{14} \left[\frac{e^+}{cm^2} \right]$ which contains a safety factor of 2.
Moreover the total heat load and the effect of multiple-scattering on the spot size have been discussed.
Before we can use this data to design the positron source, we need more information about the subsequent optics. Two points are of special interest:

- Wich capture efficiency can be achieved, i.e. how much overproduction of positrons in the target do we need ?
- How does the capture efficiency depend on the spot size of the γ-beam? As we have seen, it is possible to reduce the particle density and hence also the stress in the target by increasing the spot size of the γ radiation (see fig. 1.13). However, this would also reduce the capture efficiency.

1.5.0 Capture optics behind the target

The particles which emerge from the target have to be accelerated in a cavity embedded in a solenoid field for focusing. Here the final emittance and the efficiency of the positron source are defined. Since, compared to the thick target of a conventional source, the multiple-scattering is reduced in a thin target, the transverse momenta of the positrons emerging from the target are smaller. Fig. 1.14 compares transverse momenta of a SLC-like source with those of a thin target source driven by wiggler photons. The smaller transverse momenta lead to a higher capture efficiency of the positrons behind the target.

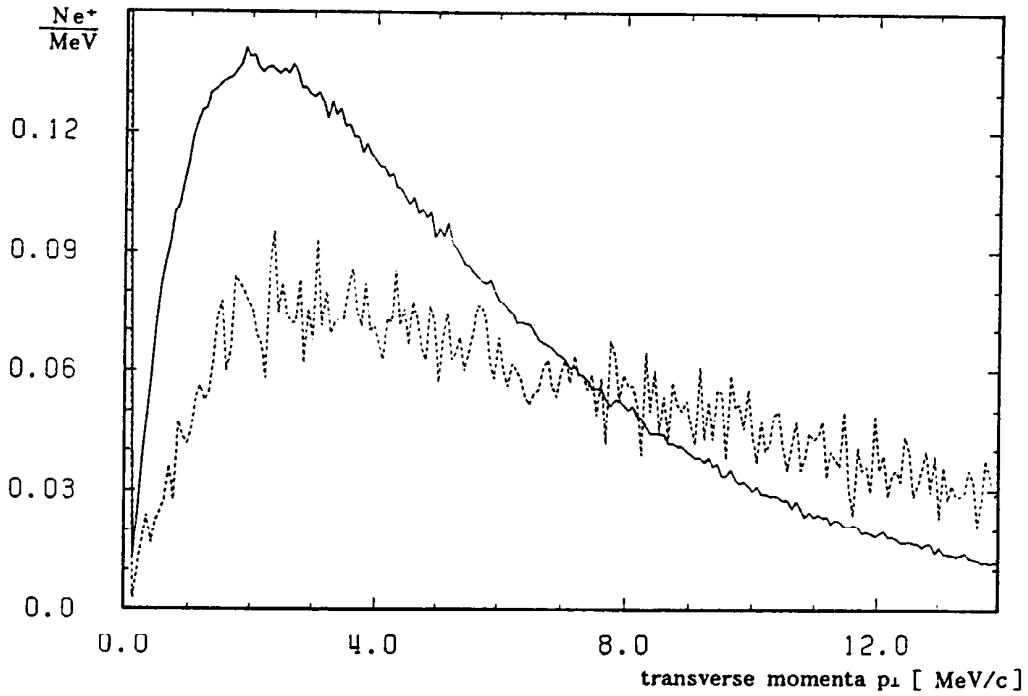

Fig. 1.14 Comparison of the transverse momenta of a SLC-like source (6 X_0, W; dotted line) and a thin target driven by wiggler photons (0.4 X_0, Ti; solid line)

In order to match the emittance of the positron beam, characterised by a small spot size and a large divergence, to the acceptance of the solenoid which is rather determined by a large spot size and a small divergence, a matching section is introduced between the converter target and the first accelerating cavity.

Two somewhat different matching devices are commonly in use, depending on the accelerator design upstream of the source.

The quarter-wave transformer is a short pulsed solenoid with a high field, followed by a long, low field solenoid. This field configuration leads to a large acceptance of transverse momenta from a small spot size. However, the acceptance is limited to a narrow energy band (narrow band system).

The adiabatic matching device is made of a tapered solenoid field, starting

with a high initial field and tapered adiabatically down to the constant end field (see fig. 1.23). The acceptance of transverse momenta is somewhat smaller than that of a quarter-wave transformer, and the accepted spot size larger, however, these properties hold for a broad energy band (broad band system).
The damping ring of a linear collider will have a large absolute energy acceptance, compared to a low energy positron accumulator like PIA for example, hence the broad band system is the favoured solution for these projects.

1.5.1 The adiabatic matching device

R. Helm [ref. 20] describes an adiabatic solution for the particle motion in a solenoid field with tapered field strength. Using the canonical coordinates:

$$p_x = x' - \frac{e\,B}{2\,P} * y$$
$$p_y = y' + \frac{e\,B}{2\,P} * x \qquad (1.12)$$

(x,y transverse coordinates; derivative with respect to the longitudinal coordinate z) the transfer matrix M, which transforms the phase space vector of a particle through the matching device, is given by [ref. 20]:

$$M = \begin{bmatrix} A\cos^2\mu & \frac{B}{2}\sin 2\mu & \frac{A}{2}\sin 2\mu & B\sin^2\mu \\ \frac{C}{2}\sin 2\mu & D\cos^2\mu & C\sin^2\mu & \frac{D}{2}\sin 2\mu \\ -\frac{A}{2}\sin 2\mu & -B\sin^2\mu & A\cos^2\mu & \frac{B}{2}\sin 2\mu \\ -C\sin^2\mu & -\frac{D}{2}\sin 2\mu & \frac{C}{2}\sin 2\mu & D\cos^2\mu \end{bmatrix}$$

$$A = \left(\frac{Bi}{Be}\right)^{1/2} \qquad B = \frac{2\,P}{e\,(Bi\,Be)^{1/2}}$$

$$C = -B^{-1} \qquad D = A^{-1}$$

Bi ≡ initial field (i.e. at the exit of the target)
Be ≡ end field (i.e. at the entrance of the cavity)

$$\text{Lamor angle } \mu = \int \frac{e\,B(z)}{2\,P}\,dz$$

For Be = Bi one obtains the well known transfer matrix of a solenoid with constant field.
The particles move in the field on spiral trajectories with increasing radius r, which is given by:

$$r^2 = \frac{1}{Be}\left[Bi\,(x_o^2 + y_o^2) + \frac{2P}{e} \sin 2\mu\,(x_o x_o' + y_o y_o') \right.$$
$$\left. + \frac{4P}{e} \sin^2\mu\,(x_o y_o' - x_o' y_o) + \frac{4P^2}{e^2 Bi} \sin^2\mu\,(x_o'^2 + y_o'^2) \right] \qquad (1.13)$$

With $x_o' = y_o' = 0$ we get:

$$r_{o\,max} = \left(\frac{Be}{Bi}\right)^{1/2} * R$$

where R denotes the aperture radius of the cavity following the matching device. With $x_o = y_o = 0$ we find:

$$(x_o'^2 + y_o'^2)^{1/2}_{max} = r_o'_1 = \frac{e\,(Bi\,Be)^{1/2}}{2\,P} * R$$

$r_o'_1$ is the maximum accepted angle for a particle which starts on the axis. In a solenoid, however, the largest accepted angles can be reached by particles at the aperture limit. With $y_o = (Be/Bi)^{1/2} \cdot R$ and $x_o = 0$ we get:

$$x_o'_{max} = \frac{e\,(Bi\,Be)^{1/2}}{P} * R = 2 \cdot r_o'_1 \qquad y_o' = 0$$

(These particles perform a circle with radius $(Be/Bi)^{1/2} \cdot R$ in the solenoid.) The above mentioned relations show the effect of the matching device, i.e. increasing radii and decreasing angles.
The maximum transmitted four-dimensional phase space volume (admittance) was calculated by Helm to be:

$$V = \int dx\,dp_x\,dy\,dp_y = \pi^2 \frac{2}{3} \left(\frac{e\,Be}{2\,m_o c\,\gamma} R^2 \right)^2$$

V scales like the beam emittance with $1/\gamma^2$, i.e. the normalized admittance is constant. Therefore the adiabatic matching device is inherently broad band; however, the solution is only valid in case of an adiabatically tapered field. The condition of validity is given by:

$$\left| \frac{dB(z)}{dz} * \frac{1}{B(z)^2} \right| = \varepsilon \frac{e}{P}$$

$$\varepsilon \ll 1$$

If we set:

$$B(z) = \frac{Bi}{1 + g*z} \qquad (1.14)$$

with the taper parameter g, we get:

$$\frac{g*P}{e*Bi} = \varepsilon \ll 1 \qquad (1.15)$$

which is independent of the longitudinal coordinate z. In this sense the field distribution of eq. 1.14 is optimized.
This field distribution is plotted in fig. 1.23.
However, the condition of validity still depends on the momentum of the particle P. Thus it can only be fullfilled up to a certain particle energy, which leads to an upper limit in the accepted energy band.
In order to investigate the breakdown of the adiabatic condition we consider the radius $\hat{r}$ of the envelope of a single particle trajectory, which is given by:

$$\hat{r} = \frac{I\ P}{e\,B(z)} + \sqrt{\left(\frac{I\ P}{e\,B(z)}\right)^2 - \left(\frac{2\ P\varphi P}{e\,B(z)}\right)^2}$$

$$P\varphi = (x\,p_y - y\,p_x)$$

$$I = \frac{e\,B}{2\,P}(x^2+y^2) + \frac{2\,P}{e\,B}(p_x^2 + p_y^2)$$

$P\varphi$ is the canonical angular momentum, which is a constant of the motion, while I is an adiabatic invariant, i.e. it is a constant only in the adiabatic approximation.
The envelope radius at the end of the matching device was calculated both by means of the adiabatic approximation and numerically by a Runge-Kutta-integration of the equations of motion, given by:

$$x'' = -\frac{e\,B(z)}{P}\,y' - \frac{e}{2P}\frac{\partial B}{\partial z}\,y$$

$$y'' = +\frac{e\,B(z)}{P}\,x' - \frac{e}{2P}\frac{\partial B}{\partial z}\,x$$

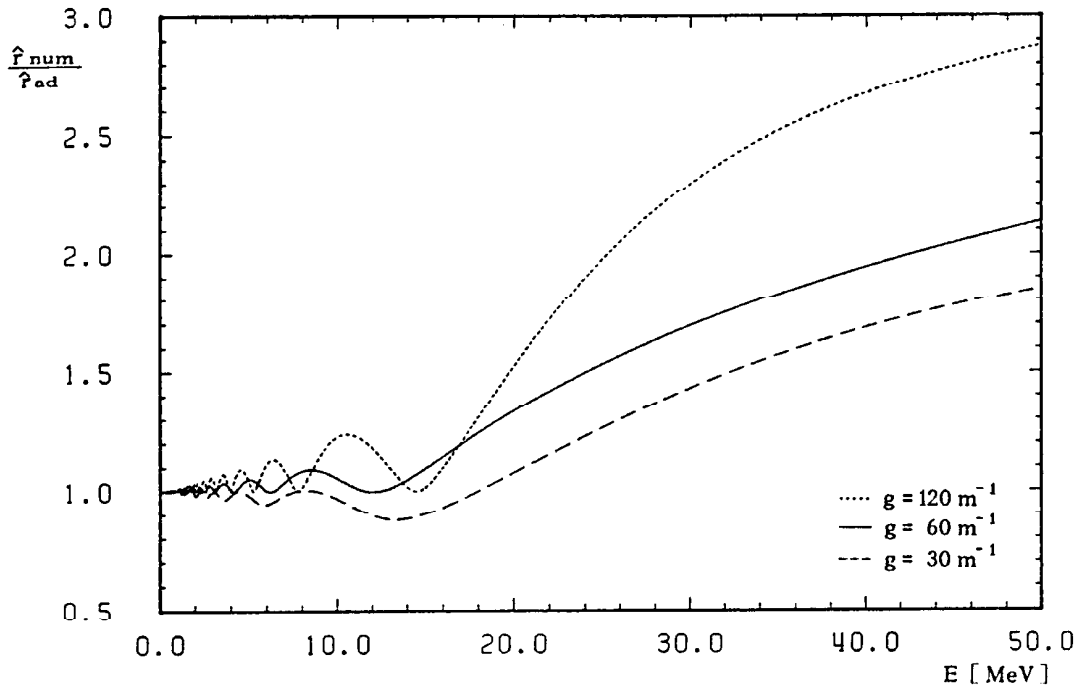

Fig. 1.15 Comparison of the adiabatic approximation with results of a Runge-Kutta integration (g/Bi = 8.8 $T^{-1}m^{-1}$)

The ratio of the envelope radius $\hat{r}_{num}$ to the envelope radius in the adiabatic approximation $\hat{r}_{ad}$ is independent of the initial conditions of the particle trajectory and hence a measure of the emittance dilution which the high energy particles suffer in the non-adiabatic field.
In fig. 1.15 the ratio $\hat{r}_{num}/\hat{r}_{ad}$ is plotted for different taper parameters g. In order to keep the condition for the adiabatic field constant, Bi was adjusted so that g/Bi is the same for the three cases plotted in fig. 1.15. Nevertheless the increase of the envelope radius is different for the three taper parameters. From eq. 1.15 one expects $\hat{r}_{num}/\hat{r}_{ad} \simeq 1$ as long as $E \ll 34$ MeV.
The emittance increase which high energy particles suffer in the tapered solenoid field does not necessarily lead to a particle loss, because the emittance of the high energy particles tends to be smaller than that of the low energy particles. Hence the optimization of the adiabatic matching device cannot be predicted from general considerations of the tapered field alone.
We have tracked a large number of positrons (~100 000) as produced by EGS through the matching device. Fig. 1.16 compares the spectrum of the emitted positrons behind the target (solid line) with the spectrum of the accepted positrons (dotted line) and with the spectrum of the positrons which are accepted in the adiabatic approximation (broken line). We observe a slowly increasing particle loss of the upper part of the spectrum rather than a sharp energy cut.

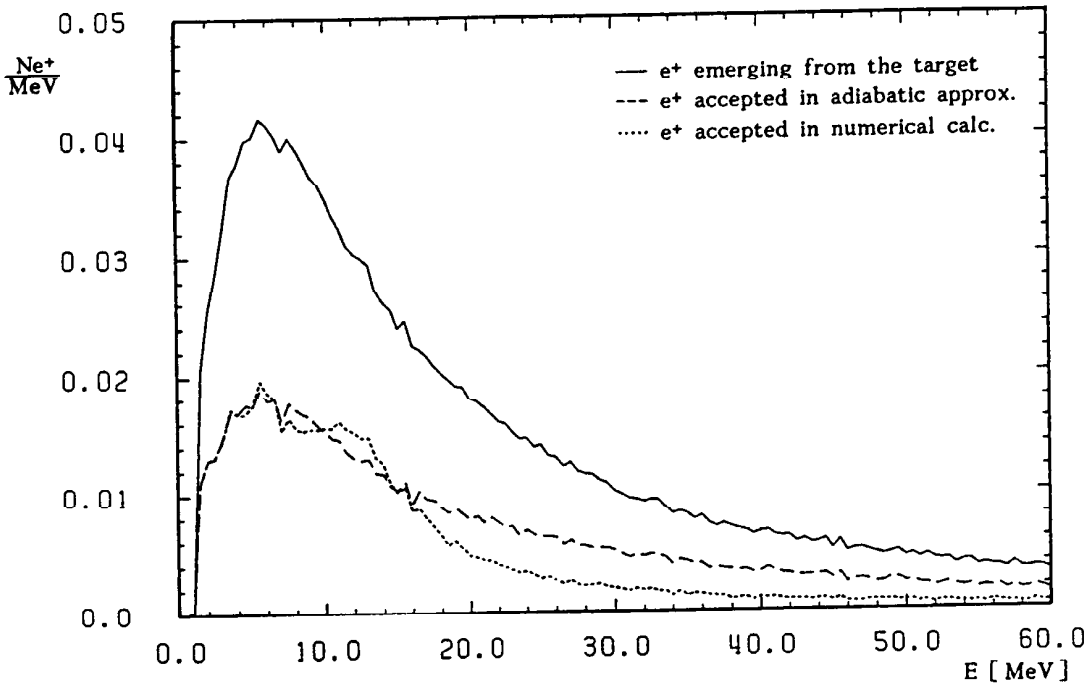

Fig. 1.16 Particle loss due to emittance growth caused by the non-adiabatic field. The plotted spectra are normalized to one positron emerging from the target. g/Bi = 8.8 T^{-1} m^{-1}

For small taper parameters the additional loss due to the non adiabatic field is of the order of 10% - 20%.
Due to different path-lengths of the particles on their spiral trajectories and due to their somewhat different velocities the bunch length is increased in the matching device and - to a smaller extent - also in the first cavity section. Since not all particles of a long bunch are on the crest of the accelerating rf-wave, a coherent energy spread is maintained during acceleration to the damping ring. Due to the limited energy acceptance of the damping ring, particles with a large dephasing with respect to the crest of the rf-wave will not be accepted.
If the particles in the first cavity section are deccelerated, the bunch lengthening might be reduced [ref. 56, 57]. However, at lower energies the particles are more sensitive to space-charge effects, which need a careful treatment in the simulations. In the 'normal' operation mode, where the particles are accelerated as soon as possible, space-charge effects can be neglegted, since the particles have a comparatively high energy (> 2 MeV) and due to the fact that every positron is accompanied by an electron, the space-charge is nearly compensated (in fact there are more electrons than positrons). The differently charged particles are seperated in the accelerating cavities.
The difference in the path length ΔL of a particle which is emitted under an angle relativ to the longitudinal z-axis, with respect to a particle emitted at zero angle is:

$$\Delta L = \left[\int_0^L \sqrt{1 + x'^2 + y'^2}\ dz \right] - L$$

For $x'^2 + y'^2 \ll 1$ we find:

$$\Delta L = \int_0^L \frac{B(z)}{2\,Bi} \left(xo'^2 + yo'^2 \right) dz$$

and finally with $B(z) = \frac{Bi}{1 + g z}$

$$\Delta L = \frac{1}{2g} \ln \left(\frac{Bi}{Be} \right) * \left(xo'^2 + yo'^2 \right)$$

In addition the dephasing due to the different velocities has to be taken into account. Since the emission angles are smaller in our thin target approach, compared to a conventional source, the relative contribution of this effect is more serious. We found that the particle loss due to different velocities is nearly as high as the loss due to the path length differences.
In order to keep the dephasing small we should select a large taper parameter, so that the length of the matching device is reduced. On the other hand the taper parameter should be small in order to make the field for high energy particles more adiabatic.
Obviously there is an optimum taper parameter where the capture efficiency has a maximum.

The calculation of the path length has been introduced into the tracking code of the matching device by a numerical integration along the trajectory, so that no approximation occurs as in the analytical formula.
Assuming an energy acceptance of ± 1 % in the damping ring, we accept only particles within ± 7.5° rf-phase (1 - cos 7.5° ~ 0.01) with respect to an optimized phase in our calculations.
(The bunch length (15° of an S-band wave ≙ 4.2 mm) is small compared to the longitudinal acceptance of the damping ring, hence the energy spread is in fact the limiting factor.)

1.5.2 Matching of the beam to the transfer line

After accelerating the beam within the focusing field of the solenoid to an energy of ~100 MeV, the divergence of the beam has been sufficiently reduced, so that it can now be focused by means of quadrupole magnets. The beam is then further accelerated to 3.15 GeV (S-band study) and injected into the damping ring. Here it has to fit into the dynamic acceptance of the damping ring otherwise we will lose particles. In order to simulate the dynamic aperture of the damping ring, we apply an acceptance limit at the beginning of the transfer line. (In practice one will of course design the transfer line with a larger acceptance.)
The properties of the beam leaving the solenoid field can be investigated by means of the radius vector of the particles in a solenoid field, given by eq.1.13 with Bi = Be = B. We find the maximum values of the particle distribution to be:

$$x_{max} = \pm R \qquad \text{for } x' = y' = y = 0$$

$$x'_1 = \pm \frac{eB}{2P} R \qquad \text{for } x = y = y' = 0$$

$$x'_{max} = \pm \frac{eB}{P} R \qquad \text{for } x = y' = 0 \; ; \; y = \pm R$$

$$y_{max} = \pm R \qquad \text{for } x' = y' = x = 0$$

$$y'_1 = \pm \frac{eB}{2P} R \qquad \text{for } x = y = x' = 0$$

$$y'_{max} = \mp \frac{eB}{P} R \qquad \text{for } y = x' = 0 \; ; \; x = \pm R$$

(Note the different signs of x'max and y'max)

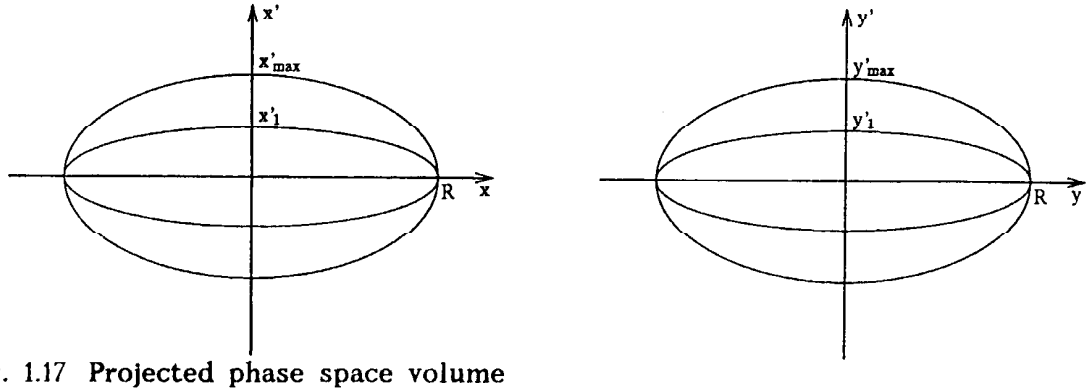

Fig. 1.17 Projected phase space volume

We consider the projections of the four-dimensional phase space volume on the x x'-plane and the y y'-plane, respectively. The emittance ellipses are not rotated ($\alpha = 0$); see fig. 1.17. (Here the emittance refers to the phase space ellipse containing 100% of the particles.) Hence the emittance is given by:

$$\varepsilon x = \varepsilon y = \frac{eB}{P} \cdot R^2$$

and we expect a four-dimensional phase space volume of:

$$V = \frac{\pi^2}{2} \varepsilon x \cdot \varepsilon y = \frac{\pi^2}{2} \left(\frac{eB}{P} R^2 \right)^2$$

which is three times larger than the four-dimensional phase space volume calculated by Helm [ref. 20]:

$$V = \frac{\pi^2}{2} \frac{1}{3} \left(\frac{eB}{P} R^2 \right)^2$$

The reason is, that the four-dimensional phase space volume is not a hyper ellipsoid as can be seen from eq. 1.13.
In canonical coordinates eq. 1.13 assumes the form:

$$r^2 = \cos^2\mu \, (x^2 + y^2) + \frac{2P}{eB} \sin\mu \cos\mu \, (x p_x + y p_y) + \left(\frac{2P}{eB}\right)^2 \sin^2\mu \, (p_x^2 + p_y^2)$$

Particles at the aperture limit fulfill the conditions:

$$(x p_x + y p_y) = x x' + y y' = 0$$

Hence the phase space volume assumes the form of a hyper ellipsoid in canonical coordinates.
However, the transformation from geometrical coordinates into canonical coordinates is not symplectic as we will see later. This means that it cannot be realized by means of a magneto-optic element.
In order to avoid any particle losses in the damping ring, we would have to make the acceptance of the solenoid not larger than the acceptance of the damping ring. This, however, would be ineffective, because the transmitted hyper ellipsoid would only be partially filled. Hence it is better to make the acceptance of the solenoid larger than the acceptance of the damping ring (at least by a factor of two) and cut a more or less completely populated phase space volume out of it.
A common way of defining the normalized acceptance A of a storage ring refers to the sum of the acceptances in the two orthogonal coordinates:

$$A = \gamma\varepsilon x + \gamma\varepsilon y$$

Hence we will apply this condition in our calculation.
The particles at the aperture limit of the distribution leaving the solenoid reach in both planes the maximum single particle emittance, i.e. $x' = x'_{max}$ only for $y = y_{max}$. Hence we get:

$$A = \gamma\varepsilon x + \gamma\varepsilon y = 2 \cdot \frac{eB}{m_o c} R^2 \qquad (1.16)$$

for the solenoid.

The correlation between the phase space vectors of the particle distribution coming out of the solenoid ($x' = x_{max}$ only for $y = y_{max}$) can be used to transform emittance from one plane to the orthogonal one by means of a skew quadrupole magnet. (This is useful if the acceptance of the damping ring turns out to be larger in one plane.)
In the thin lens approximation the transformation performed by a skew quadrupole can be written as:

$$\begin{aligned} x_s &= x \\ x'_s &= x' + \frac{eKl}{P} \cdot y \\ y_s &= y \\ y'_s &= y' + \frac{eKl}{P} \cdot x \end{aligned}$$

(This transformation has to be compared with the transformation into canonical coordinates eq. 1.12. Since the transformation of a skew quadrupole is symplectic, it is obvious that the transformation into canonical coordinates is not symplectic.)
We set:

$$K \cdot l = B/2$$

K = gradient of the quadrupole
l = length of the quadrupole
B = field strength of the solenoid

and find the following relations:

$$\begin{aligned} x'_{s\,max} &= \pm 3 \frac{eB}{2P} R \\ x'_{s\,1} &= x'_1 \\ y'_{s\,max} &= \pm \frac{eB}{2P} R^2 \\ y'_{s\,1} &= y'_1 \end{aligned}$$

The effect of a skew quadrupole of strength $K \cdot l = B/2$ is shown in fig. 1.18. The emittance is decreased in one plane by a factor of 2 while it is increased in the orthogonal plane. The sum of the emittances stays constant.
In practical cases, the correlated parts of the phase space volume are only rarely populated. Therefore the effect of a skew quadrupole has only a minor practical meaning.

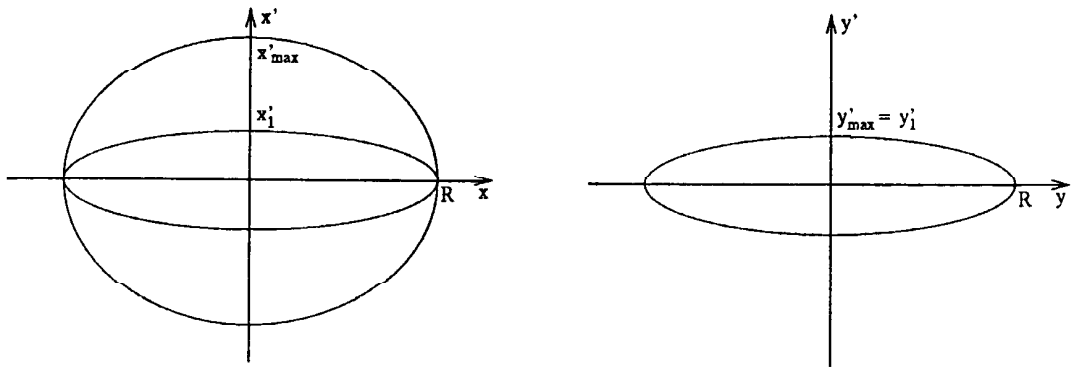

Fig. 1.18 The effect of a skew puadrupole on a correlated particle distribution

1.5.3 Parameters of an optimized matching device

The normalized acceptance of the damping ring is $\gamma\varepsilon x + \gamma\varepsilon y \simeq 0.024$ [ref. 21] for the S-band study. (For TESLA it might even be larger. The capture efficiency, i.e the ratio of the number of positrons accepted by the transfer line to the number of positrons emerging from the target, scales roughly linearly with the acceptance.)

For the pre-acceleration section we choose parameters, comparable to that at the existing SLC source, namely: aperture radius of the cavity iris R = 9 mm and field strength of the solenoid B = 0.62 T. Hence the normalized acceptance as defined by eq. 1.16 is A = 0.059, i.e. a factor of 2.45 higher than the acceptance of the damping ring. The particle loss at the matching point from the solenoid to the transfer line is nevertheless only of the order of 5%.

In order to get a high initial field, a pulsed field from a flux concentrator is added to a strong DC-field in the matching device [ref. 22, 23]. The initial field at the SLC source is Bi $\simeq$ 7 T. It could be increased to 10 T which seems to be the upper limit of this technique [ref. 24].

With Bi = 7 - 10 T and Be = 0.62 T we found, for the taper parameter g (eq. 1.14), an optimum at $g = 30\ m^{-1}$.

Small variations of the target thickness show a broad maximum at a thickness of 0.4 X_0. For a thicker target the yield is somewhat higher (see fig. 1.11), but the capture efficiency is lower due to larger emission angles of the particles.

Fig. 1.19 shows the effect of the longitudinal cut on the spectrum of the positrons. The particle losses due to the dephasing are of the order of 30%.

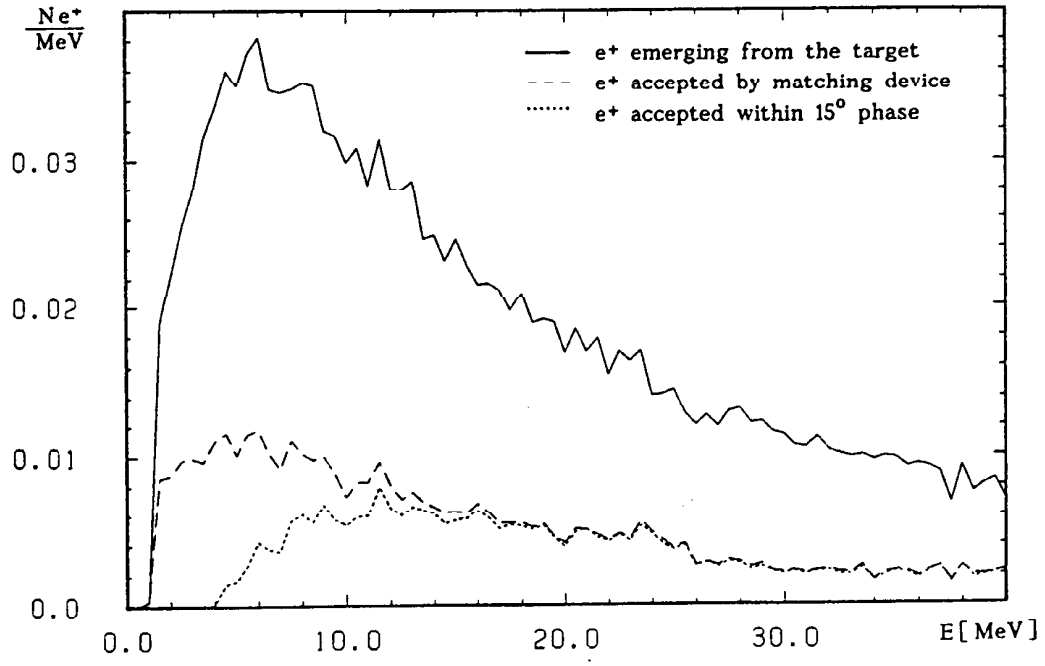

Fig. 1.19 Energy spectra of the positrons from wiggler photons impinging on a 0.4 X_0 titanium target. (Normalized to one positron emerging out of the target.)

The corresponding longitudinal beam profile is shown in fig. 1.20. It shows that the core of the beam is maintained, while the low energy particles form a long tail.

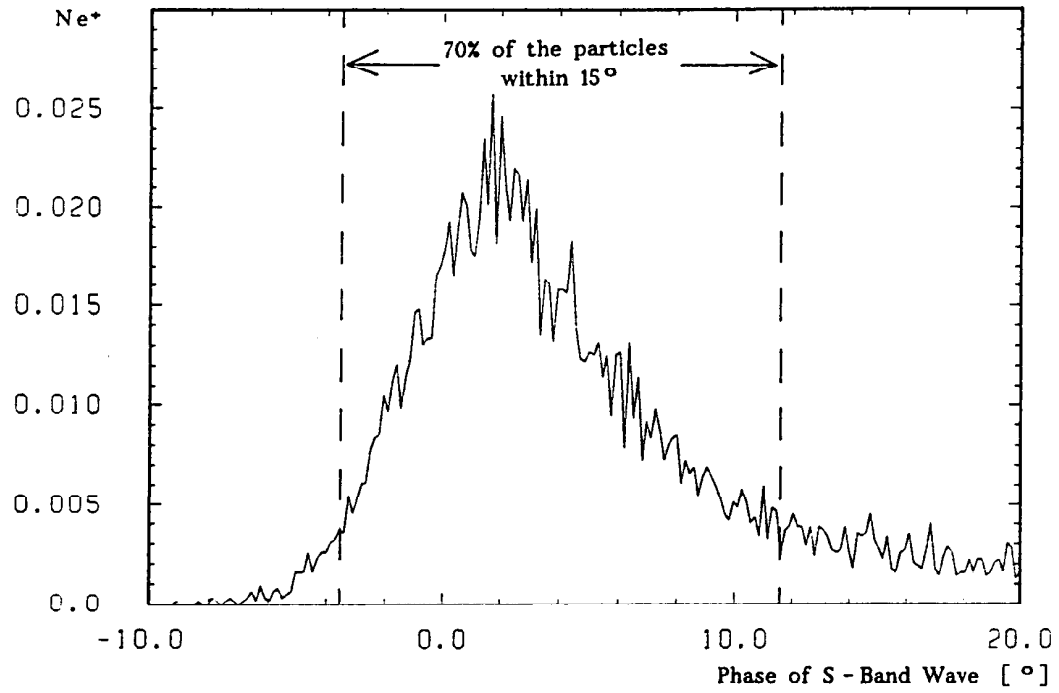

Fig. 1.20 Longitudinal beam profile behind the matching device. The bunch length of the primary beam $\sigma_z = 0.7$ mm corresponds to 2.5°. (Normalized to one positron emerging from the target.)

Obviously the capture efficiency is not very sensitive to small variations of the condition for the longitudinal acceptance. Hence we conclude that our simple phase-cut is a sufficient condition in our simulation.

The capture efficiency as a function of the spot size of the oncoming γ-beam is plotted in fig. 1.21. It was calculated with an initial field of the matching device of Bi = 10 T. A reduction of the field to 7 T decreases the capture efficiency from 18.5% to 15% for $\sigma_{x,y} = 0.7$mm, while an enhancement of the initial field to 15 T increases the efficiency to only 19.7%. For higher initial fields the efficiency drops again.

This shows that the optimum efficiency, i.e. the optimum matching is achieved with fields close to what is technically feasible. A further improvement of the efficiency by means of new techniques e.g. lithium lenses [ref. 25] or plasma lenses [ref. 26] may, hence, in the case of a thin target source, not be expected from the stronger focusing fields, but only from differences in the particle dynamics. In plasma and lithium lenses the particle moves, for example, not on a spiral trajectory but on a sinusodial path, thus the dephasing is reduced. However, it will be difficult to vary the focusing field with the longitudinal coordinate in these devices. Hence they act more like a quarter-wave transformer with a small bandwidth than like an adiabatic matching device.

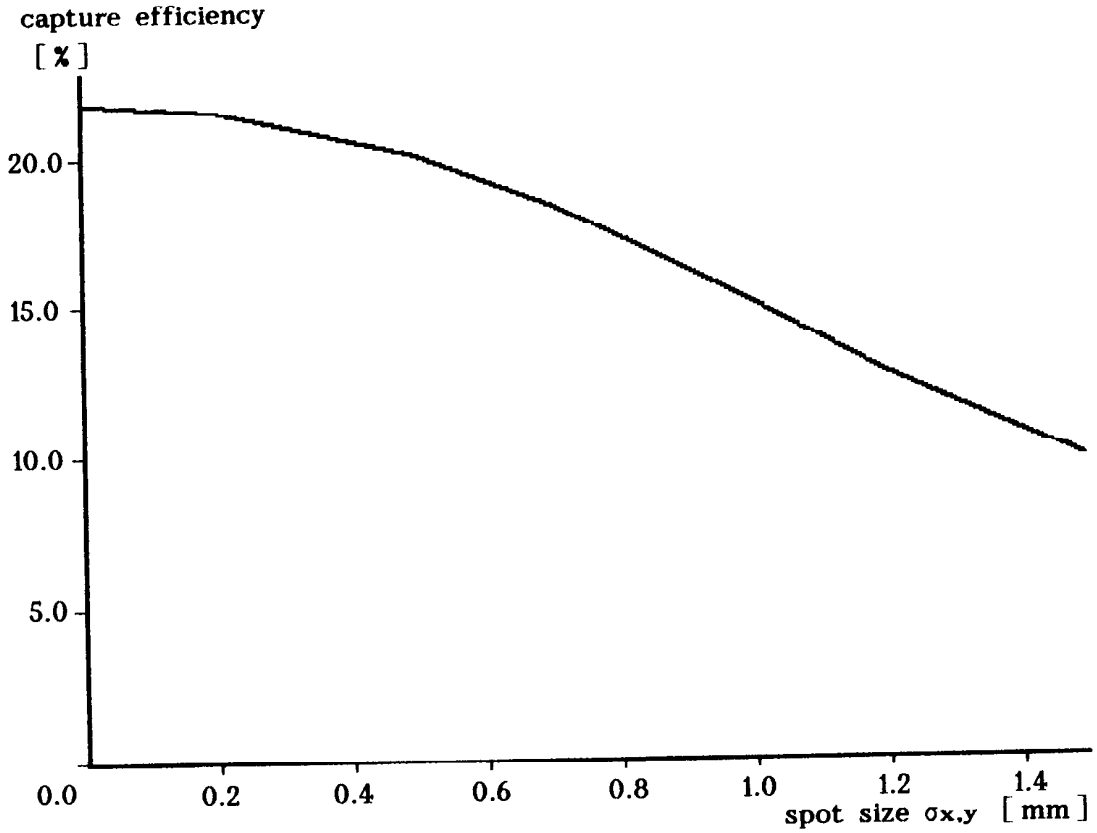

Fig. 1.21 Capture efficiency versus spot size of the γ-beam

Now we have all information that we need to calculate the maximum positron intensity that we can obtain from a source based on wiggler radiation:
The maximum tolerable positron density in a titanium target was shown to be: $\hat{\rho}^+ = 7 \cdot 10^{12}$ e^+/mm^2 (eq. 1.11). Fig. 1.13 shows the particle density $\rho(\sigma x,y)$, normalized to one positron emerging from the target, as a function of the spot size of the oncoming γ-beam.

σx,y mm	ρ(σx,y) mm^{-2}	Ne+tot 10^{12}	capture efficiency	Ne+ 10^{12}
0.3	0.67	10.5	0.210	2.21
0.5	0.32	21.9	0.201	4.40
0.7	0.18	38.9	0.185	7.19
1.0	0.10	70.0	0.151	10.57
1.2	0.08	87.5	0.127	11.11
1.5	0.05	134.6	0.098	13.12

Tab. 5 Maximum tolerable positron production as a function of the spot size of the oncoming γ-beam. σx,y ≡ sigma of the γ-beam; ρ(σx,y) ≡ particle density normalized to one positron (see fig. 1.13); Ne+tot ≡ maximum number of positrons produced in the target; Ne+ ≡ number of positrons matched to the first cavity section.

The maximum number of positrons Ne^+tot which can be produced in the target, is given by the ratio $\hat{\rho}^+/\rho(\sigma x,y)$. Tab. 5 summarizes Ne^+tot for various sigmas of the γ-beam.
With increasing spot size more and more positrons can be produced, however, the capture efficiency drops with larger spot sizes (see fig.1.21). Hence the number of positrons which can be matched to the first cavity section, Ne^+, increases not as fast as the number of positrons which are produced in the target. Moreover the wiggler length has to be increased, in order to reach the higher intensities.
So far we have matched only the particles to the cavity section. Now we have to avoid particle losses in the beam transfer to the damping ring. An important effect is the bunch lengthening in the first accelerating structures where the ratio of the transverse momenta to the longitudinal momenta is still large.
The dephasing in the subsequent cavity section depends on the gradient and can be kept small.
In the cavities the transverse momenta stay constant and the variation of the longitudinal velocity can be analytically calculated. We found, for the path length difference of a particle with respect to a particle travelling with the velocity of light on the axis:

$$\Delta s = c\left(T - \frac{1}{a}\left[\sqrt{(a\,T + b)^2 + 1} - \sqrt{b^2 + 1} \right] \right)$$

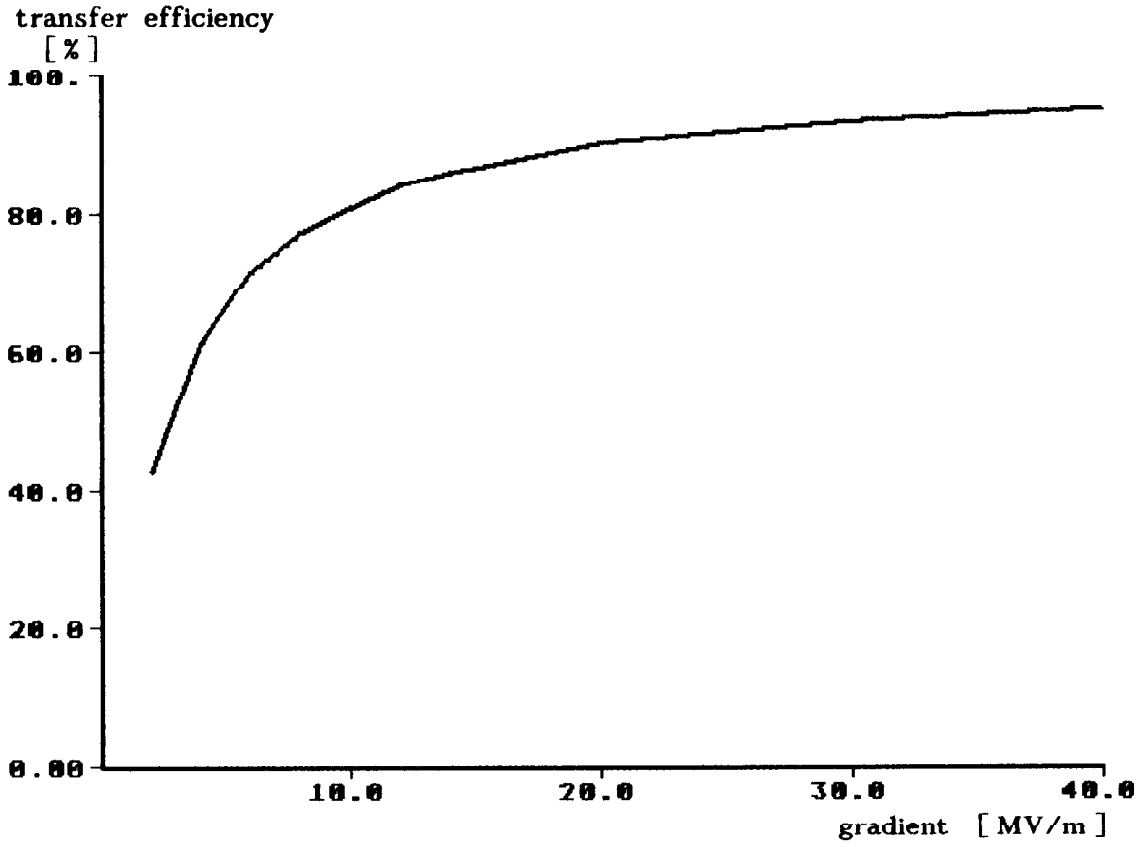

Fig. 1.22 Transfer efficiency for the accelerating section versus gradient

$T \equiv$ time of flight (reference particle) = $E/(\Delta E * c)$

$$a = \frac{e * \Delta E}{m_e c * K} \quad ; \qquad b = \frac{p_{oll}}{m_e c * K}$$

$$K = \left[\left(\frac{p_t}{m_e c} \right)^2 + 1 \right]^{1/2}$$

$p_t \equiv$ transverse momentum
poll $\equiv$ longitudinal momentum at the beginning of the section
$E \equiv$ total voltage of the section (100 MV)
$\Delta E \equiv$ gradient in the section

Fig. 1.22 shows the transfer efficiency of the pre-acceleration section as a function of the gradient in the cavities.
The standard gradient in S-band travelling wave structures is about 20 MV/m and gradients up to 40 MV/m have been achieved, so that the dephasing in the cavities can be sufficiently suppressd.
The situation is somewhat more complicated for TESLA due to the long bunch train of 800 μs.
Behind the positron target there will be a large background of positrons, electrons, photons, neutrons and muons which will deposit energy in the first cavities. Hence it seems to be impossible to preaccelerate the positrons by means of superconducting cavities.
The preacceleration has to be done with normal conducting cavities up to an energy of 100-200 MeV, where the positrons can be separated from the back ground and be injected into the standard superconducting TESLA cavities.
Two problems arise for the acceleration of the long TESLA bunch train in a normal conducting cavity:

- klystrons, able to deliver high power for such a long rf-pulse, are not available yet.
- the energy deposition of a long rf-pulse in the cavity walls would be much too high in case of a high power, i.e. high gradient, cavity.

It was proposed to use a pulse compression system (SLED system) to overcome these problems [ref. 5]. Here the klystron delivers power on a low level over the whole pulse length of 800 μs, while the accelerating structure is filled with 1 MHz rep. rate for every single bunch. Between successive bunches the power is used to fill a storage cavity.
The advantages of these systems are as follows:

- due to the pulsed operation of the accelerating cavities the energy deposition in the cavities can be kept small.
- due to the pulse compression the gradient is higher, for a given mean power. In the simulations a gain of 1.6 in the gradient was achieved, while the power deposition was reduced by a factor of 2.58.

More details can be found in ref. 5.

1. 5. 3 Improvements in the optics

– An optimized field distribution for the matching device

The field distribution of the adiabatic matching device (eq. 1.14) was developed in a way that the condition for an adiabatic field was independent of the longitudinal coordinate. This is a resonable argument, however, one may ask for a field distribution which takes all the input parameters of the source, like the positron spectrum, the bandwidth of the damping ring etc., into account.
In order to find such a distribution we have used an evolutionary strategy:
The field distribution of eq. 1.14 can be expanded in a Taylor series.

With $$B(z) = \frac{Bi}{1 + g*z}$$

we get $$\frac{d^n B(z)}{dz^n} = n!\, Bi\,(-g)^n \frac{1}{(1+g z_0)^{n+1}}$$

hence $$B(z) = \sum_n Bi\,(-g)^n \frac{(z - z_0)^n}{(1+g z_0)^{n+1}}$$

With $z_0 \simeq L/2$ (L = length of matching device) twenty coefficients are sufficient to approximate the initial field distribution.
By statistical variation of these coefficients the field distribution can be slightly distorted and by tracking particles through the new field an optimized field can be found. In principle a realistic simulation of the beam transport from the target to the damping ring can be introduced.
To avoid an increase of the initial and end field Bi and Be of the device two additional coefficients had to be added:

$$C_1 = \frac{Bi - B(z=0)}{L}$$

$$C_2 = \frac{B - B(z=L)}{L}$$

$$B(z) = \sum_n Bi\,(-g)^n \frac{(z - z_0)^n}{(1+g z_0)^{n+1}} + C_1 (L - z) + C_2 \cdot z$$

Since the length of the matching device appears in C_1 and C_2, it can also be optimized by statistical variation.
Fig. 1.23 shows a comparison of the initial field distribution and the optimized field distribution as a result of the evolutionary strategy.
The length of the matching device is reduced by ~35 % but the capture efficiency is increased only by ~3 % in case of a thin target source.
The improvement of the yield tends to be larger the in case of a conventional thick target source and in cases where boundary conditions, i.e. energy limits have been introduced.

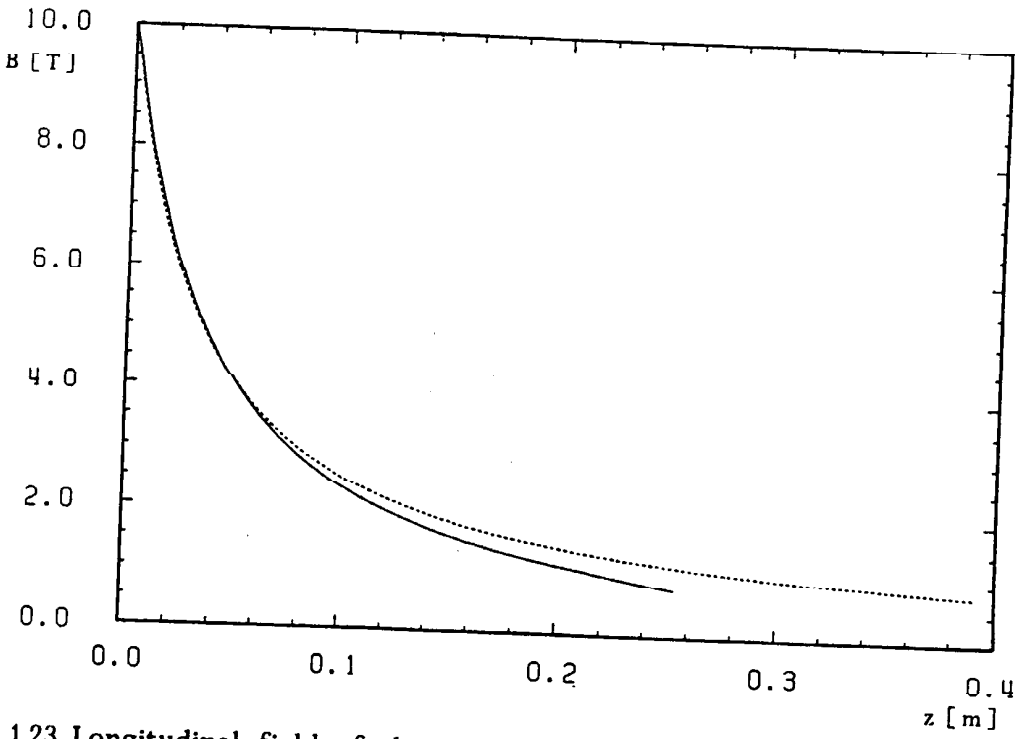

Fig. 1.23 Longitudinal field of the adiabatic matching device. The lines show the field distribution according to eq. 1.14 (dotted line, $g = 30\ m^{-1}$) and the optimized field distribution (solid line).

1.6.0 A high intensity positron source

After the discussion of the various parts of the positron source in the previous sections, we will now consider the source as a complete system and thereby summarize some important results of our investigation and draw some conclusions.

It is proposed to use the disrupted 250 GeV electron beam after collision as a primary beam to generate the wiggler radiation. Anyway, the beam has to pass the final focus quadrupole magnets of the oncoming beam in order to avoid mechanical damage as well as an intolerably high background in the detector. It requires, however, some additional optical effort to match the disrupted beam to the wiggler requirements.

The desired beam properties in the wiggler section are governed by the requirement of being able to adjust the wiggler radiation spot size on the conversion target over a range of 1 - 3 mm in diameter in order to optimize positron capture efficiency versus thermal stress in the target. In addition, it is desirable to keep the transverse beam size in the wiggler section below about 2 mm to reduce the costs of fabrication.

There are two contributions to the radiation spot size which add up more or less quadratically, namely the opening angle of the synchrotron radiation α and the beam parameters in the wiggler section. We consider a wiggler of L = 40 m length plus about 10 m distance D for the separation of the primary beam.

In the case of a wiggler with period length λ the opening angle of the radiation α can be approximated by:

$$\alpha \approx \frac{e\,B}{P} * \frac{\lambda}{2\pi} + \frac{1}{\gamma}$$

It follows:

$$\sigma_{SR} \approx \frac{e\,B}{P\,2\pi} * (L/2 + D) * \lambda \approx 9.74 \cdot 10^{-3}\,\lambda$$

To achieve σ_{SR} = 0.5 mm , λ must not be larger than 51 mm.

A wiggler with a period length less than 51 mm, based on hybrid technology, is already in use in DORIS [ref. 60]. However, even with a gap height g of 4 - 5 mm the field distribution will be more or less sinusodial. The maximum field amplitude on the axis of the wiggler is given by [ref. 61]:

$$B_{max} = 3.33 \cdot \exp[\,-g/\lambda\,(5.47 - 1.8\,g/\lambda)\,]$$

with g/λ = 0.078, we obtain:

$$B_{max} = 2.2\ T$$
$$B_{rms} \simeq 1.5\ T$$

A more rectangular field distribution at reduced field amplitude can be obtained by means of a pure permanent magnet wiggler.

The positron production is insensitive to the photon spectrum, as we have already shown. However, it scales with the total photon number and hence with the rms-field amplitude.
Assuming that the wiggler consists of sections of alternating constant magnetic field $B = \pm 1.7$ T, we overestimate the positron production by roughly 15%.
In order to minimize the cost of the wiggler, the gap height should be small and we have to have a small rms beam size σ_e in the wiggler section.
The electron beam is focused onto the target and the spot size σ_e^* of the beam on the target should be:

$$\sigma_e^* = 0.5 \text{ mm}$$

while in the wiggler section

$$\sigma_{ey} \leq 0.7 \text{ mm}$$

$$\sigma_{ex} \leq 2.0 \text{ mm}$$

is sufficient.
Then, the minimum tolerable β-function on the target is about:

$$\beta^*_y \approx (L+D) * \frac{\sigma_e^*}{\sigma_{ey}} = 36 \text{ m}$$

$$\beta^*_x = 13 \text{ m}$$

The maximum β value inside the wiggler is then:

$$\beta_y = \frac{(L+D)^2}{\beta^*} + \beta^* = 105 \text{ m}$$

$$\beta_x = 213 \text{ m}$$

And for the maximum tolerable emittance of the disrupted beam we obtain:

$$\hat{\varepsilon}_y = \frac{\sigma_{ey}^2}{\beta_y} = 4.7 * 10^{-9} \text{ m}$$

$$\hat{\varepsilon}_x = 1.9 * 10^{-8} \text{ m}$$

This would easily be satisfied by the emittance of the oncoming electrons before the collision, which is below 10^{-11} m for both, the S-band study (DESY/THD) and TESLA.
However, the emittance is diluted during collision due to the non linear forces which the electrons sustain in the field of the positron bunch. In addition the particles lose a fraction of their energy due to beamstrahlung. This leads to a broad, asymmetric energy distribution of the electrons after collision.
(We have investigated the influence of this broad energy distribution on the photon spectrum of undulator radiation in more detail in ref. 36. Here this effect can be neglected.)
The bandwidth of the matching optics between interaction point and wiggler is limited due to local chromaticities which can only be compensated in a narrow energy band [ref. 27]. However, the bandwidth can be increased if

some emittance dilution can be allowed. A bandwidth of ±10% has been shown to be feasible for a disrupted beam transport line in a positron recycling scheme [ref. 2], which, however, does not meet our emittance requirements.

A conservative estimate for a matching optic, able to meet the emittance requirements for the wiggler leads to a bandwidth of ±3%, corresponding to ~70% of the particles of the beam for the S-band study [ref. 11].
R. Brinkmann has designed an optic for a particle recycling sytem for TESLA, which also can be adopted for the positron source. Due to the somewhat smaller energy spread of the beam after interaction and due to the refined optics, approximately 90 % of the particles can be collected within an emittance of $\hat{\varepsilon}x \simeq 10^{-9}$ m and $\hat{\varepsilon}y \simeq 10^{-11}$ m [ref. 30].
For the DESY/THD S-band study a positron intensity of $3.6 * 10^{12}$ positrons per pulse is required.
In addition we demand that 2 positrons per electron are captured, as a saftey margin for compensation of particle losses which might occur, for example, during injection into the damping ring etc. . This factor of 2 will also compensate particle losses due to bunch lengthening in the accelerating structure. Hence $7.2 \cdot 10^{12}$ positrons have to be captured.
If the positron production is too high, it can easily be adjusted, for instance by means of an increased gap height of the wiggler (lower field), or by means of a decreased solenoid field in the preacceleration section.
From tab. 5 we see, that this value corresponds to a $\sigma x,y$ of the γ-beam of 0.7 mm. In this case $4 \cdot 10^{13}$ positrons are produced in the target and the capture efficiency is 18.5%.
Now we can calculate the length L of the wiggler section:
The optimum target thickness was found to be $0.4\,X_0$, where the yield of a titanium target is: $\Upsilon e+ = 0.45 \frac{e+}{e^-m}$ (see fig 1.11).
We set, for the efficiency of the matching optics, $\eta m = 0.7$, and, for the capture efficiency of the particles behind the target, $\eta c = 0.185$. Hence, we get:

$$L * \Upsilon e+ * \eta c * \eta m = 2\ e+/e^-$$

$$L = 34\ m$$

With a more realistic field distribution the wiggler length will be approximately 40 m.
The maximum temperature rise during a shot is 720 K and the mean deposited power in the target turns out to be 5.9 kW for 50 Hz rep. rate (see table 4).
Table 6 summarizes all parameters of the source. They should only be regarded as an example for one possible solution, because an adjustment of the parameters is still possible without exceeding technical limits. For example the initial field of the matching device might be reduced for technical reasons. The capture efficiency would shrink in this case and the wiggler length would have to be increased.

Wiggler	
field on axis	~1.7 T
period length	≤ 51 mm
gap height	~ 4 mm
total length	~34 m
spot size of radiation on target $\sigma_{x,y}$	0.7 mm
number of photons per electron	10.5 m^{-1}
mean photon energy	22 MeV
Target	
material	titanium alloy
target thickness	0.4 Xo ≙ 1.42 cm
pulse temperature rise	720 K
mean deposited power	6 kW S-band 14 kW TESLA
Adiabatic matching device	
initial field	10 T
taper parameter g	30 m^{-1}
end field	0.62 T
radius of cavity iris	9 mm
Damping ring	
norm. acceptance $\gamma\varepsilon_x + \gamma\varepsilon_y$	0.024 m
capture efficiency	18.5 %
estimated overall efficiency	9.25 %

Tab. 6 Parameters of a high intensity source. The estimated overall efficiency includes particle losses during injection into the damping ring etc. and refers to the fact that 2 positrons per electron are produced.

The TESLA approach requires a positron intensity of $4.5 * 10^{13}$ positrons per bunch train, which is another order of magnitude more than in the S-band design.
Since the bunch spacing is large for TESLA (1 μs) compared to other designs, the thermal load problems of the target can be solved by means of a rotating target.
If we choose the velocity of the circumference of the rotating target disk to be 50 m/s, no more than 60 bunches will overlap on the target, leading to a maximum temperature rise of ~ 700 K. The mean power deposited in the target with 10 Hz rep. rate will be 14 kW.
In order to load all parts of the target disk with thermal stress, successive shots should be placed next to each other on the target as sketched in fig. 1.24.
Within one bunch train (0.8 ms) the advance of the target on the disk Δs is 0.04 m. In order to place the next shot after n revolutions beside the foregoing shot the condition

$$\tau_{rep} = \tau_{bunch\ train} (N * n \pm 1)$$

has to be fulfilled.

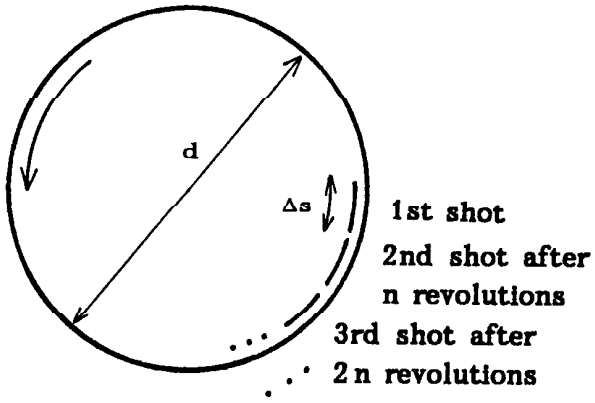

Fig. 1. 24 The rotating target disk

n	N	d [m]	τ_{cool} [s]	revolutions per minute
1	124	1.58	12.4	605
2	62	0.79	6.2	1210
3	41.3	0.53	4.1	1815
4	31	0.39	3.1	2419

Tab. 7 Comparison of target parameters.

N denotes the number of shots, which can be placed on the circumference of the target. Thus the diameter of the target has to be $d = N * 0.04\ m / \pi$ and the time for cooling, i.e. the time between two shots on the same place, is

$\tau_{cool} = N * \tau_{rep}$. Tab. 7 compares parameters for various numbers of revolutions between successive shots.

1.6.1 Cooling of the target

The most critical component of a water cooled target is the rotating vacuum feed-through for the water supply. Organic materials, as they are used for example in O-rings, cannot be used in the highly radiative environment of the positron target and commercially available feed-throughs with bellows cannot be used at the revolution frequency which is necessary for TESLA.
A possible solution has been worked out by P. Sievers and M. Höfert from CERN for a positron target, able to withstand a mean power deposition of 800 kW [ref. 28]. The feed-through is based on differential pumping of a series of stationary chambers around the axis.
For TESLA, however, the mean power deposition is only small compared to the large volume of the target.
Hence one might as well consider radiation cooling supported by cooling of the rest gas in the chamber. A radiation cooled target offers the additional advantage that problems like the radiolysis of the cooling water and the transport of radioactivity with the cooling water are reduced. The rotation can, in this case, be transferred onto the target-wheel by means of a magnetic coupling.
The radiation flux Φ from a hot body (surface area A, temperature T) to the environment (temperature T') is given by the Stefan-Boltzmann-law:

$$\Phi = \varepsilon \sigma A (T^4 - T'^4)$$

ε = emission coefficient ≤ 1
σ = Stefan-Boltzmann-constant = $5.67 * 10^{-8} \frac{W}{m^2 K^4}$

If we embed the target in a material with high heat conductivity, the energy has to be transferred to the material and then radiated at a low temperature level from a large surface area A.
Assuming a mean temperature of the target disk of 500 K, while the environment stays on 300 K, we find that for the surface area of the disk $A = 4.5\ m^2$, if the power of 14 kW has to be radiated from this area. Since the circumference of the wheel is of the order of some meters, this area can be provided by means of large cooling fins.
Alternatively we consider cooling due to the rest gas:
In order to achieve a substantial cooling of the rest gas in the vacuum chamber, it would be necessary to allow the pressure to be of the order of $10^{-2} - 10^{-1}$ mbar for a large part of the target surface. The pressure near the beam area could nevertheless reach the operational requirements by means of differential pumping.

The target has to rotate in the S-band case too, however, here only an overlap of adjacent bunch trains has to be avoided. In order to separate the bunch trains (rep. rate 50Hz) by ~3 mm on the target wheel a velocity of only 0.15 m/s is necessary, which can be achieved with a small target radius, as in case of the SLC source [ref. 29].
However, a large radiation cooled target with a magnetic coupling is an attractive solution for reliability reasons. Therefore it should also be considered for the S-band study.

1.6.2 Source operation

An operational disadvantage of a wiggler based source is the coupling of the source to the main linac. Two crucial points should be mentioned.
For the commissioning of the positron damping ring, the main positron linac etc. a source which works independently of the main electron linac would be desirable in order to work on both linacs simultaneously.
It is worth noting that a large fraction of this work can be done or even has to be done with a low intensity source. Fig. 1.25 shows a conventional low intensity souce integrated into the high intensity beam line. Per 500 MeV electron 0.1 positrons are produced in the thin titanium target. The capture efficiency is roughly 15 %, so that ~1 % of the design intensity can be obtained with a primary electron beam at design current. Higher intensities at a low repetition rate can be reached, if several shots are accumulated in the damping ring.

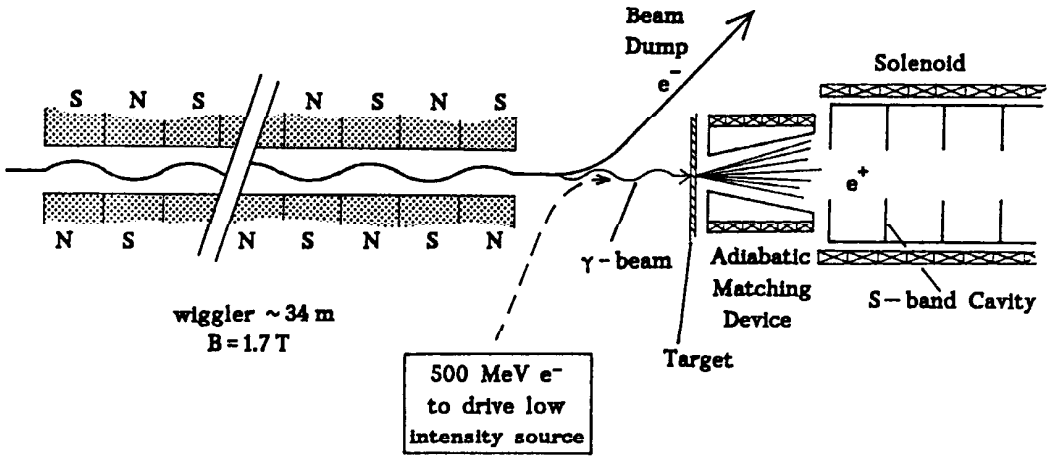

Fig. 1.25 Integration of a conventional, low intensity source into the beam line of a high intensity source based on wiggler radiation (see fig. 1.0 for comparison)

A more severe question concerns the stability of the source.
The energy width of a linear accelerator is affected by the longitudinal wake potential (single bunch energy spread) and by beam loading effects (bunch to bunch energy spread). Since the final focus optics has only a small bandwidth (1 - 2%), the energy width is not only important for the experimental program, but also for the operation of the linac. Different techniques can be used to

minimize the energy spread which, however, depend on the intensity of the beam. Hence, intensity variations of the source have to be controlled within a few percent.
One reason for intensity variations of the positron source is a drift of the beam spot on the target, which can be introduced by different effects in the steering optics (current drifts, magnet vibrations, temperature variations etc.).
In fig. 1.26 the influence of an offset Δr on the positron yield is plotted. (The offset is defined with respect to the intersection of the cavity axis (behind the target) with the target.) In order to suppress the intensity variation below -1% the offset has to be controlled within ± 0.1 mm in each direction.

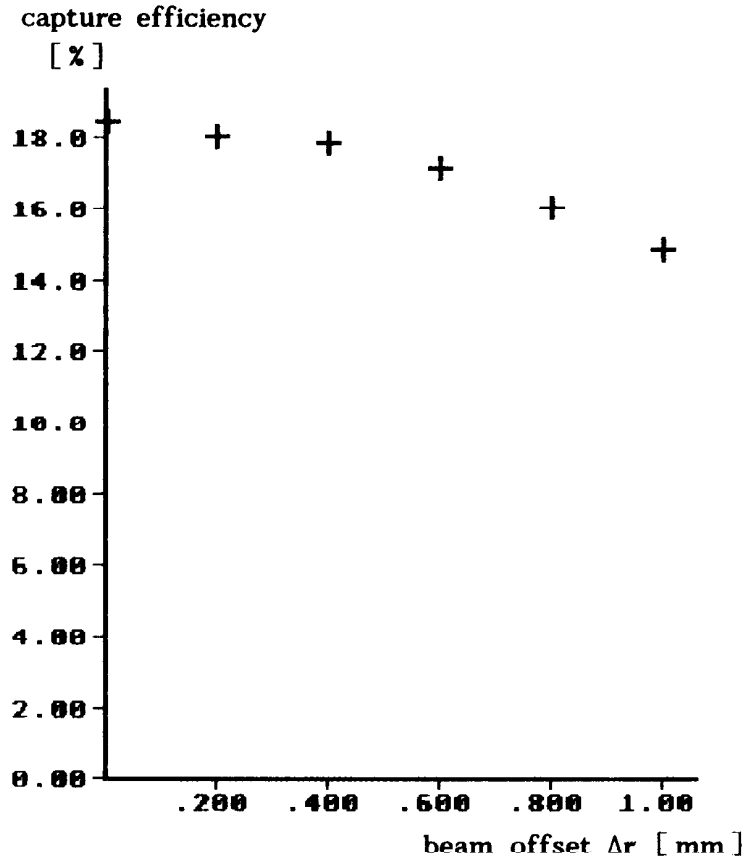

Fig. 1.26 Influence of a beam offset on the capture efficiency

If we assume that no steering coils are introduced in the wiggler section, the offset of the beam spot is determined both by the offset and by the angle of the beam in the last steering magnet before the wiggler.
The offset can be measured with a beam position monitor, with a resolution well below 0.1 mm. Then the angle can be determined by means of a monitor, which directly observes the spot size on the target. Here the visible part of the wiggler radiation might be useful. Both, the offset and the angle can be controlled by means of simple feed-back loops and appropriate orbit bumps. A similar system works at the SLC positron source [ref. 31].

Like any other positron source the wiggler based source relies upon a constant beam intensity of the primary beam. However, due to the beam-beam interaction and the limited efficiency of the matching optics, the positron production depends on the intensity of the foregoing shot.
We consider a simplified model to investigate this effect:
In the case that the beams collide with the design intensity in both bunches, we can describe the positron production by:

$$P_0 = \eta_0 \cdot E_0$$

$P_0 \equiv$ number of positrons
$E_0 \equiv$ production factor $\simeq L \cdot \Upsilon_{e^+} \cdot \eta_C \cdot N_{e^-}$
$\eta_0 \equiv$ efficiency of the matching optics at design currents

with

$$\eta_0 = 1 - \nu_0$$

$\nu_0 \equiv$ particle loss

We consider a distortion of the positron number by a factor α

$$P_{dist} = P_0 \cdot \alpha$$

$$\alpha = 1 + \varepsilon \qquad -1 < \varepsilon < +1$$

The particle loss as a function of the intensity of the foregoing shot is unknown. We use a scaling of α with the power n, which simply addresses the fact that the particle loss increases or decreases with increasing or decreasing intensity of the foregoing shot, respectively. For a sufficiently high n this treatment may be regarded as a worst case calculation.
We set:

$$\eta_{dist} = 1 - \nu_0 \cdot \alpha^n$$

The production in the next shot P_1 assumes the form:

$$P_1 = \eta_{dist} \cdot E_0$$
$$= (1 - \nu_0 \cdot \alpha^n) \cdot E_0 = \alpha_1 \cdot \eta_0 \cdot E_0$$

and we get:

$$\alpha_1 = 1 + \varepsilon_1 = 1 - \frac{\nu_0}{1 - \nu_0} (\alpha^n - 1)$$

For stability the condition

$$| \varepsilon_1 | = \frac{\nu_0}{1 - \nu_0} (\alpha^n - 1) \leq | \varepsilon | \qquad (1.16)$$

has to be fulfilled.
With

$$\alpha^n = (1 \pm \varepsilon)^n = \sum_{k=0}^{n} \binom{n}{k} \cdot \varepsilon^k$$

we find, for equality of the stability equation (1.16):

$$\frac{\nu 0}{1-\nu 0}\left(n+\sum_{k=2}^{n}\binom{n}{k}\varepsilon^{k-1}\right)=1$$

With $\varepsilon = 0$ we can derive a lower stability limit ξ_1 at:

$$\nu 0 = \xi_1 = \frac{1}{1+n}$$

The maximum distortion occurs when no positrons disrupt the oncoming electrons and all electrons are matched to the wiggler section. With $\eta = 1$ we get:

$$P_{dmax} = E_0$$

Hence $\alpha_{max} = \frac{1}{1-\nu 0}$ and $\varepsilon_{max} = \frac{\nu 0}{1-\nu 0}$

Introducing α_{max} and ε_{max} into the stability equation (1.16), we find:

$$\left(\left(\frac{1}{1-\nu 0}\right)^{n}-1\right)\leq 1$$

and we can derive a second stability limit ξ_2 at:

$$\nu 0 = \xi_2 = 1 - 2^{-1/n}$$

Table 8 compares ξ_1 and ξ_2 for different scaling parameters n.

n	ξ_1	ξ_2
1	0.50	0.50
2	$0.3\overline{3}$	0.29
3	0.25	0.21
4	0.20	0.16

Tab. 8 Stability limits for different scaling parameters n

The meaning of the stability limits are as follows:
For $\xi_1 > \nu 0 > \xi_2$ only small distortions are attenuated, while large distortions are exited and the system can become unstable, i.e. the beam intensity varies from shot to shot between a maximum and a minimum value.
For $\nu 0 < \xi_2$ all possible distortions are damped and stable operation would be possible in any case.
The calculations represent only a crude model of the positron source, which however shows, that the coupling via beam-beam interaction does not necessarily lead to an unstable state of the positron source.
The stability of the positron source can additionally be affected by beam loading effects in the main linac [ref. 32], which require a more sophisticated treatment in the framework of the whole linac.

1.6.3 Source operation at different energies

So far we have developed a positron source for a 500 GeV center-of-mass collider. However, the collider has to operate over an energy range, starting at ~300 GeV where interesting results of top physics are expected up to the highest energies which can be achieved.
The number of photons produced in a wiggler or undulator is independent of the energy of the primary beam. However, the energy of the photons scales with γ^2. Hence the positron production decreases, if the energy of the primary beam is decreased. Fig. 1.27 shows the total positron yield as a function of

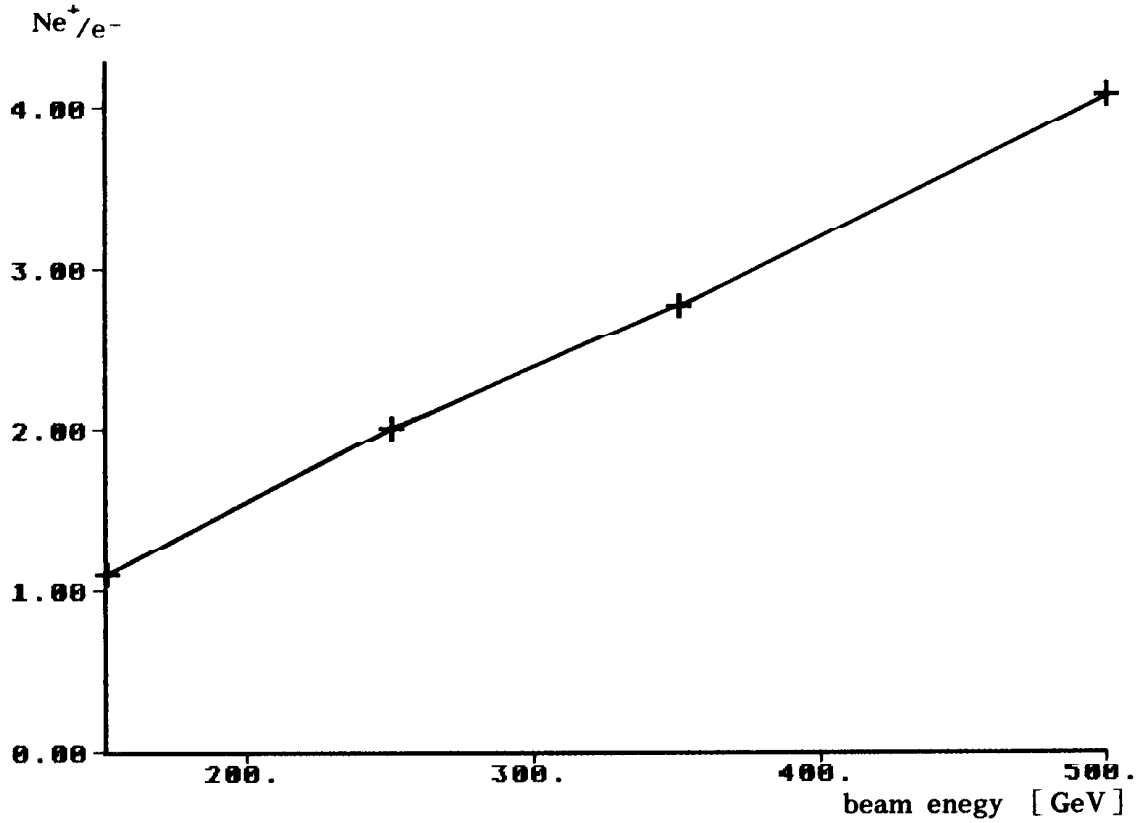

Fig. 1.23 Positron yield per electron at IP versus energy of the primary beam (wiggler length 34 m)

the energy of the primary beam. For the calculations we had to make some assumptions about the efficiency of the matching section between interaction point and wiggler.
The beamstrahlung is much softer for a 2 * 150 GeV collider, hence the energy distribution of the particles after collision is smaller [ref. 6] and we can assume that 100% of the particles can be matched to the wiggler section. For the higher energies above 150 GeV the matching efficiency was kept constant $\eta m = 0.7$. Since the parameters of a 1 TeV collider are not yet fixed, this is somewhat arbitrary, however, in any case the beamstrahlung has to be sufficiently small in order to allow high energy physics experiments.

The yield of 1.1 e+/e at 300 GeV would be sufficient, if no additional losses were to occur. In order to readjust our saftey margin we can either double the wiggler length or run the machine with different currents in both beams. If the number of electrons is increased by 34% above the present design current, the positron current will be 75% of the design, while the luminosity stays constant. This would of course have a lot of implications for the machine operation which are not considered here.

1.6.3 Radiological problems

A detailed discussion of the radiological problems of a wiggler based positron source would exceed the intention of this work. We can, however, draw out some general considerations by comparing the wiggler based source with a conventional high intensity positron source like the SLC source.
The radiological problems divide into two fields:

- the production of high energy particles (positrons, electrons, photons, neutrons and muons), which ask for an adequate shielding.
- the production of unstable isotopes in the target and the surrounding structures (induced activity), which is a particular problem in the case of a target failure.

The most important processes in the converter target are gamma-neutron reactions via the so called giant dipole resonance, whereby one or more neutrons are knocked out of the nucleus. The process can be understood as an oscillation of the neutrons against the protons in the nucleus and corresponds to the frequency of absorption of electric dipole radiation [ref. 33]. The cross section for photo nuclear reactions is plotted in fig. 1.1.
At higher energies other processes like deuteron photo-disintegration and photon production of π-mesons set in [ref. 34]. The total cross sections of these processes are by a factor of 100 up to 1000 times smaller, hence they contribute only to a small amount to the induced activity. However, pions decay into muons, which are difficult to shield [ref. 35]. Since the content of high energy photons in the wiggler radiation is only small, these processes are suppressed in a wiggler based source compared to a conventional source with a multi GeV primary beam.
Compared to a conventional source, which would produce the required positron intensity (30 times SLC for the S-band study and 67 times SLC for TESLA) the neutron production is reduced by a factor of 5 in case of the wiggler based source due to the higher capture efficiency.
The neutron production in the thin target is comparable to the neutron production at the rear end of the thick target. In the thick target the photons have to be produced in the first radiation length of the target, hence we assume a linearly increasing neutron production from the beginning to the end of the target, while in the wiggler based source the photons penetrate from the beginning through the target and the neutron production rate is assumed

to be constant. Therefore the neutron production is reduced by a factor of:

$$\frac{6}{2 \cdot 0.4} \simeq 7.5$$

(thick target: 6 X_0; thin target: 0.4 X_0)
This factor is of course modified if different materials are used.
The total integrated cross section for electric dipole absorption can be estimated by means of the Thomas-Reiche-Kuhn (TRK) sum rule to be [ref. 33]:

$$\int_0^\infty \sigma(E)\, dE = 60 \cdot \frac{N \cdot Z}{A} \text{ MeV mb}$$

The formula overestimates the cross section for light and medium nuclei by a factor of ~2. Hence we conclude that the neutron production per radiation length in titanium is about a factor of 1.5 higher than in tungsten.
Taking all effects together, we can conclude that the neutron production of the wiggler based source will roughly be the same as at the present SLC source for the S-band study and ~2.5 times higher for TESLA, even though the positron intensity is increased.
Due to the emission of neutrons, new isotopes are produced inside the target with a production rate P.
Tab. 9 summarizes isotope properties for gamma-neutron reactions in tungsten and titanium.
Other isotopes are produced via gamma-proton reactions, however, due to the Coulomb barrier, nearly all the photon absorption strength leads to a neutron emission in heavy and medium nuclei [ref. 33].

Isotope	Abundance %	Reaction	End Product	Half life $t_{1/2}$	Decay mode
W_{186}	28.6	(γ, n)	W_{185}	75 d	β^-
		$(\gamma, 2n)$	W_{184}	stable	-
W_{184}	30.7	(γ, n)	W_{183}	stable	-
		$(\gamma, 2n)$	W_{182}	stable	-
W_{183}	14.3	(γ, n)	W_{182}	stable	-
		$(\gamma, 2n)$	W_{181}	121.2 d	γ
W_{182}	26.3	(γ, n)	W_{181}	121.2 d	γ
		$(\gamma, 2n)$	W_{180}	stable	-
Ti_{48}	73.8	(γ, n)	Ti_{47}	stable	-
		$(\gamma, 2n)$	Ti_{46}	stable	-
Ti_{47}	7.4	(γ, n)	Ti_{46}	stable	-
		$(\gamma, 2n)$	Ti_{45}	3.08 h	β^+
Ti_{46}	8.2	(γ, n)	Ti_{45}	3.08 h	β^+
		$(\gamma, 2n)$	Ti_{44}	47.3 a	γ

Tab. 9 Gamma-neutron reactions in tungsten and titanium.

The dangerous isotopes are W_{181} in the tungsten target and Ti_{44} in the titanium target. Both decay under emission of a γ-quant. Since Ti_{44} is produced only in one channel out of an isotope with small abundance in the naturally occuring element, the production rate of Ti_{44} is somewhat lower than that of W_{181}.
The induced activity A in the target is given by:

$$A = P\left(1 - e^{-\frac{\ln 2}{t_{1/2}} \cdot t}\right)$$

It can be seen, that due to the half life of 121 days for W_{181} the full activity can be reached within a run period of the source (~ half of a year), while the activity in the titanium target increases slowly over many years, so that it is lower at least in the first years of operation.
The whole situation is of course modified by additional elements in the target alloys and by the surrounding structure material.
The above analysis can not substitute a detaild quantitative analysis, which has to be done before a source based on wiggler radiation can be build. It shows, however, that the radiological problems will not increase dramatically, compared to already existing sources which might be a sufficient conclusion for the moment.

2.0.0 A high intensity polarized positron source

In flat circular e^+e^- colliders the beams become polarized vertically due to an asymmetry in the spin-flip rates in the synchrotron radiation process. However, owing to depolarizing effects resulting from misalignments the equilibrium polarization can be small if no special orbit and optical correction schemes are applied. In addition the rotation of the spin into the longitudinal direction calls for great effort.
In a linear collider it is relatively easy to collide longitudinally polarized beams once polarized particle sources are available.
Polarized electrons can be produced by means of photoemission from a photocathode which is illuminated by circularly polarized laser light. A source of this kind is in operation at the SLC and R & D efforts show significant progress, so that we can assume that a reliable, highly polarized electron source is available for the next linear collider [ref. 37].
The physics potential of polarized beams can be demonstrated - without going into details - by means of the spin dependence of the weak interaction. An overview of physical problems which can be attacked with polarized beams in linear colliders is given in ref. 38.
The polarization P of an electron or positron beam is defined as:

$$P = \frac{N^+ - N^-}{N^+ + N^-}$$

where N^+ and N^- denote the number of particles with spin +1/2 and -1/2, respectively.
Hence we find the number of particles with spin +1/2 in a polarized beam to be:

$$\frac{N^+}{N^+ + N^-} = \frac{1}{2}(1+P)$$

and the number of particles with spin -1/2:

$$\frac{N^-}{N^+ + N^-} = \frac{1}{2}(1-P)$$

We consider neutral current interactions of electron-positron annihilation at high energies. Electrons can anihilate on positrons with a virtual intermediate state being either a photon or a Z^0 boson.
One can write neutral current parameters in the form of vector, g_V, and axial vector, g_A, couplings:

$$g_V = g_R + g_L$$

$$g_A = g_R - g_L$$

g_R and g_L refer to the right-handed and the left-handed part of the coupling, respectively.

The production rate of left-handed electrons with right-handed positrons is proportional to g_L^2, and for right-handed electrons with left-handed positrons proportional to g_R^2.
We denote the longitudinal polarization of the electron and positron beam with P_1 and P_2, respectively and find the number of left-handed and right-handed particles in the beam to be:

$$Ne_L = \frac{1}{2}(1+P_1) \qquad Ne_R = \frac{1}{2}(1-P_1)$$

$$Np_L = \frac{1}{2}(1-P_2) \qquad Np_R = \frac{1}{2}(1+P_2)$$

where e and p refer to electrons and positrons, respectively.
The production rate of the reaction is proportional to:

$$R^+ \sim Ne_L \cdot Np_R \cdot g_L^2 + Ne_R \cdot Np_L \cdot g_R^2 =$$

$$\frac{1}{4}(1 + P_1 + P_2 + P_1 \cdot P_2) \cdot g_L^2 + \frac{1}{4}(1 - P_1 - P_2 + P_1 \cdot P_2)\, g_R^2$$

$$\sim \frac{1}{2}(1+P_1P_2)(g_V^2 + g_A^2) - (P_1+P_2)\, g_V g_A$$

In the case of the opposite polarization of both beams we find:

$$R^- \sim \frac{1}{2}(1+P_1P_2)(g_V^2 + g_A^2) + (P_1+P_2)\, g_V g_A$$

Moreover we are interested in the asymmetry A:

$$A = R^+ - R^- \sim P_1 + P_2$$

Here contributions from background-reactions which are not sensitive to polarization cancel within the statistical probability. The statistical error $\Delta A/A$ of the asymmetry term is proportional to:

$$\frac{\Delta A}{A} \sim \frac{1}{P_1 + P_2} * \frac{1}{\sqrt{N}}$$

$N \equiv$ number of events

Hence, to obtain a given accuracy, the number of events to be measured is proportional to:

$$N \sim \frac{1}{(\Delta A/A)^2 \cdot (P_1 + P_2)^2}$$

and the figure of merit for the operation of a linear collider with polarized beams is:

$$L \cdot (P_1 + P_2)^2$$

$L \equiv$ Luminosity

We conclude that polarized positrons - even if there would be no new physics accessible (if polarized electrons are already available) - offer a great potential for the reduction of background problems and power consumption. Since background problems, luminosity and power consumption are the most crucial problems for linear colliders even a big effort for a polarized positron source seems to be worthwhile.
The basic idea for a polarized positron source was proposed by V.E. Balakin and A.A. Mikhailichenko in 1979 [ref. 9]. In contrast to the unpolarized source (see fig. 1.0), a helical undulator is used instead of the planar wiggler to produce circularly polarized photons. Since only the photons near the optical axis of the undulator are circularly polarized, a scraper collimates the photon beam. Therefore an overproduction of photons is necessary and the length of the undulator has to be larger than the wiggler of the unpolarized source. The polarized photons are converted into polarized electron-positron pairs in the converter target.
Before we investigate this scheme in more detail, we recall some of the basic properties of polarized photon and positron/electron beams.

2.2.0 Classical polarization and quantum mechanical spin formalism

The polarization state of a classical electromagnetic wave is completely characterized by four independent quantities, for example:

- the intensity of the wave
- the polarization with respect to a set of two orthogonal states (transversal or circular)
- the phase-relation of these states
- the coherence of the wave.

A more convenient parameter set are the so called Stokes parameters (G. G. Stokes 1852) which are directly related to four measureable quantities, i. e. intensities:

- The first Stokes parameter ξ_0 is the total intensity I_0 of the wave: $\xi_0 = I_0$
- A combination of the intensity behind a polarizator in x direction I_x and the respective intensity in the orthogonal direction $I_y = I_0 - I_x$ gives the second Stokes parameter ξ_1:

$$\xi_1 = \frac{I_x - I_y}{I_0}$$

$$-1 \leq \xi_1 \leq +1$$

- The third Stokes parameter ξ_2 is related to the linear polarization in a coordinate system rotated by 45° with respect to the one used above:

$$\xi_2 = \frac{I_{45} - I_{135}}{I_0}$$

$$-1 \leq \xi_2 \leq +1$$

- By introducing a phase shift of $\lambda/4$ between the wave components in x and y direction (quarter wave plate) and measuring again the linear polarization at 45^0, the longitudinal polarization, related to the fourth Stokes parameter ξ_3, can be determined:

$$\xi_3 = \frac{I_L - I_R}{I_0}$$

$$-1 \leq \xi_3 \leq +1$$

$\sqrt{\xi_1^2 + \xi_2^2 + \xi_3^2} \leq 1$ is a measure of the coherence of the wave, while for the coherent part of the wave the phase α between the orthogonal components in the x and y directions may be obtained from:

$$\tan \alpha = \frac{\xi_1}{\xi_2}$$

Now we consider the mathematical description of a wave:

$$\mathbf{E}(\omega,\mathbf{z},t) = (E_x(\omega,\mathbf{z},t) , E_y(\omega,\mathbf{z},t)) \qquad (2.1)$$

with

$$E_x(\omega,\mathbf{z},t) = A_x(t) * e^{i(\omega t - \mathbf{kz})}$$
$$E_y(\omega,\mathbf{z},t) = A_y(t) * e^{i(\omega t - \mathbf{kz})}$$

where $A_x(t)$ and $A_y(t)$ denote time dependent complex amplitudes.
The intensity averaged over time (denoted $\langle\ \rangle$) is obtained by:

$$I_0 = \xi_0 = \langle |\mathbf{E}(\omega,\mathbf{z},t)|^2 \rangle = \langle \mathbf{E}\,\mathbf{E}^* \rangle = \frac{1}{2}\langle A_x A_x^* \rangle + \frac{1}{2}\langle A_y A_y^* \rangle$$

The effect of a polarizator can be applied to equation 2.1 by multiplying it by the matrix T_x (or T_y):

$$T_x = \begin{bmatrix} 1 & 0 \\ 0 & 0 \end{bmatrix} \qquad T_y = \begin{bmatrix} 0 & 0 \\ 0 & 1 \end{bmatrix}$$

We obtain:

$$I_x = \langle | T_x \cdot \mathbf{E}(\omega,\mathbf{z},t)|^2 \rangle = \frac{1}{2}\langle A_x A_x^* \rangle$$

$$I_y = I_0 - I_x = \frac{1}{2}\langle A_y A_y^* \rangle$$

$$\xi_1 = \frac{\langle A_x A_x^* \rangle - \langle A_y A_y^* \rangle}{\langle A_x A_x^* \rangle + \langle A_y A_y^* \rangle} \qquad (2.2)$$

For the measurement at 45° we need in addition the rotation matrix T45:

$$T45 = \frac{1}{\sqrt{2}} \begin{bmatrix} 1 & 1 \\ -1 & 1 \end{bmatrix}$$

$$I45 = \langle | Tx \cdot T45 \cdot \mathbf{E}(\omega,z,t) |^2 \rangle$$

$$\xi 2 = \frac{\langle AxAy^* \rangle + \langle Ax^* Ay \rangle}{\langle AxAx^* \rangle + \langle AyAy^* \rangle} \qquad (2.3)$$

Finally for the phase shift we need the matrix $T_{\frac{\pi}{2}}$:

$$T_{\frac{\pi}{2}} = \begin{bmatrix} 1 & 0 \\ 0 & i \end{bmatrix}$$

$$IL = \langle | Tx \cdot T45 \cdot T_{\frac{\pi}{2}} \cdot \mathbf{E}(\omega,z,t) |^2 \rangle$$

$$\xi 3 = \frac{i(- \langle AxAy^* \rangle + \langle Ax^* Ay \rangle)}{\langle AxAx^* \rangle + \langle AyAy^* \rangle} \qquad (2.4)$$

These results may be expressed in a different form. We introduce the density matrix ρ:

$$\rho = \frac{1}{Io} \begin{bmatrix} \langle AxAx^* \rangle & \langle AxAy^* \rangle \\ \langle Ax^* Ay \rangle & \langle AyAy^* \rangle \end{bmatrix} = \frac{1}{2} \begin{bmatrix} 1 + \xi 1 & \xi 2 - i\xi 3 \\ \xi 2 + i\xi 3 & 1 - \xi 1 \end{bmatrix}$$

By means of the Pauli spin matrices:

$$\Sigma 1 = \begin{bmatrix} 1 & 0 \\ 0 & 1 \end{bmatrix} \qquad \Sigma 2 = \begin{bmatrix} 0 & 1 \\ 1 & 0 \end{bmatrix} \qquad \Sigma 3 = \begin{bmatrix} 0 & -i \\ i & 0 \end{bmatrix}$$

the polarization states may now be obtained by:

$$\xi n = Tr (\rho \cdot \Sigma n)$$

This is equivalent to the usual description of polarization in quantum mechanics, where Ax and Ay represent field operators.
The formalism is the same for photons and electrons exept for one substantial difference. For a mass-less particle like the photon, only the projections of the field operator on the direction of motion are gauge invariant and hence observable properties. Therefore the coordinate system has to be chosen in a way such that Ax and Ay are perpendicular to the direction of propagation. Then $i(-\langle AxAy \rangle + \langle Ax\ Ay \rangle)$ has the form of a spin operator and can be interpreted as the projection of the angular momentum on the direction of

motion [ref. 39]. Thus one can say that the spin of the photon is always oriented in the direction of propagation [1].
The components ξ_1 and ξ_2 are defined only with respect to the chosen coordinate system, i. e. they can be transformed into a new system, rotated by an angle ψ with respect to the direction of motion.
The vector $P = (I_o, \xi_1, \xi_2, \xi_3)$ transforms into P' in the new system, by means of: $P' = T_\Psi * P$ with the transfer matrix

$$T_\Psi = \begin{bmatrix} 1 & 0 & 0 & 0 \\ 0 & \cos 2\psi & \mp\sin 2\psi & 0 \\ 0 & \pm\sin 2\psi & \cos 2\psi & 0 \\ 0 & 0 & 0 & 1 \end{bmatrix}$$

For an electron exists no preference direction. Hence the spin, i. e. the projection of the angular momentum on a reference axis, may be defined with respect to an arbitrary coordinate system, without regarding the motion of the particle. (The angle between the spin axis of an ensemble of electrons and the direction of propagation can even be changed by means of ' spin rotators' , i. e. special arrangements of electromagnetic fields. This is impossible in case of photons.)

We define:

ξ_1 = spin component in x direction
ξ_2 = spin component in y direction
ξ_3 = spin component in z direction

where x,y,z represent an orthogonal coordinate system. The transformation into a new coordinate system can be performed with the transfer matrices:

$$T_\varphi = \begin{bmatrix} 1 & 0 & 0 & 0 \\ 0 & \cos\varphi & 0 & \mp\sin\varphi \\ 0 & 0 & 1 & 0 \\ 0 & \pm\sin\varphi & 0 & \cos\varphi \end{bmatrix} \qquad T_\Theta = \begin{bmatrix} 1 & 0 & 0 & 0 \\ 0 & \cos\Theta & \mp\sin\Theta & 0 \\ 0 & \pm\sin\Theta & \cos\Theta & 0 \\ 0 & 0 & 0 & 1 \end{bmatrix}$$

$T_\varphi \equiv$ rotation about y axis
$T_\Theta \equiv$ rotation about z axis

Orthogonal spin states describe states with an angle of 180° in ordinary space, while the transverse polarization states of the photon differ only by 90°. Therefore the angle in the transfer matrix of the photon T_Ψ has to be 2Ψ.

---

1 The angular momentum of a circular polarized photon beam has been measured by R. A. Beth [ref. 40].

2.2.1 Calculation of polarized electromagnetic showers

The obvious way to calculate electromagnetic cascades is to simulate the shower by means of Monte-Carlo methods, i.e. particles are tracked through a material while processes occur with a probability given by their cross section.
The development of the shower is nearly unaffected by polarization effects. Only negligibly small asymmetries in the angular distribution may occur in case of polarized primary particles.
The processes of an electromagnetic cascade are of quantum mechanical nature and describe the interaction of *particles* with each other. A single particle is always completely polarized with respect to any direction and the expectation value determines the probability of finding the particle in one of two orthogonal states. The Monte-Carlo approach would be to generate randomly the spin state of the particles with respect to the expectation value and calculate the processes with completely polarized particles.
This way has to be chosen if, for example, the asymmetry of the angular distribution should be calculated.
However, we are only interested in the *mean* polarization of the particles emerging from the target. Thus it is sufficient to calculate the polarization properties of the single processes using the quantum mechanical expectation value which is equivalent to the classical polarization of a wave.
A convenient form for the description of polarization properties is a matrix formalism developed by H. Mc. Master [ref. 41, 42]. Any process can be described by a matrix T by means of:

$$P' = T * P \qquad (2.5)$$

with $P' = (\sigma_0, \sigma_{\xi 1}, \sigma_{\xi 2}, \sigma_{\xi 3})$ ≡ cross sections for the states of the outgoing particles

$P = (1, \xi_1, \xi_2, \xi_3)$ ≡ polarization of the incoming particle

The element $T_{1,1}$ is the total cross section for the process.
$\sigma_{\xi n}/T_{1,1}$ gives the expectation value for the polarization as a function of the polarization of the oncoming particle.
We make use of a reduced formalism where the matix of eq. 2.5 is divided by $T_{1,1}$, hence:

$$P' = (1, \xi_1', \xi_2', \xi_3')$$
$$P = (1, \xi_1, \xi_2, \xi_3)$$
$$T_{1,1} = 1$$

Since we have introduced polarization into an already existing Monte-Carlo program the production of the particles is predicted by the program and we have only to calculate the associated polarization states which can be done with the reduced matrix.

2.2.1 The Electron-Gamma-Shower code EGS 4

The EGS code [ref. 18] is a general purpose package for the Monte-Carlo simulation of electromagnetic showers. It has been developed by R. L. Ford and W. R. Nelson based on a work of H. H. Nagel [ref. 43]. Since its formal introduction in 1978 it has been extended and improved and a lot of comparisons with experiments have been performed [ref. 44, 45].
A blockdiagram of EGS4 is shown in fig. 2.1. The program consists of two parts, the user-written program (Main) with the subroutines Howfar and Ausgab and the actual EGS code which is a large subroutine with a number of sub-subroutines.
In the Main program some initialization takes place and the EGS code is called. The geometry of the problem that should be calculated has to be introduced in the subroutine Howfar, while in Ausgab the information which the user needs, have to be extracted.
In the EGS code itself the bookkeeping for the particles of the shower is performed and various processes are calculated in sub-subroutines e.g. bremsstrahlung in BREMS and pairproduction in PAIR.
An important feature of the EGS code is that additional calls to Ausgab can be ' switched on ' by the user by means of some statements in the Main program (optional calls in fig. 2.1).

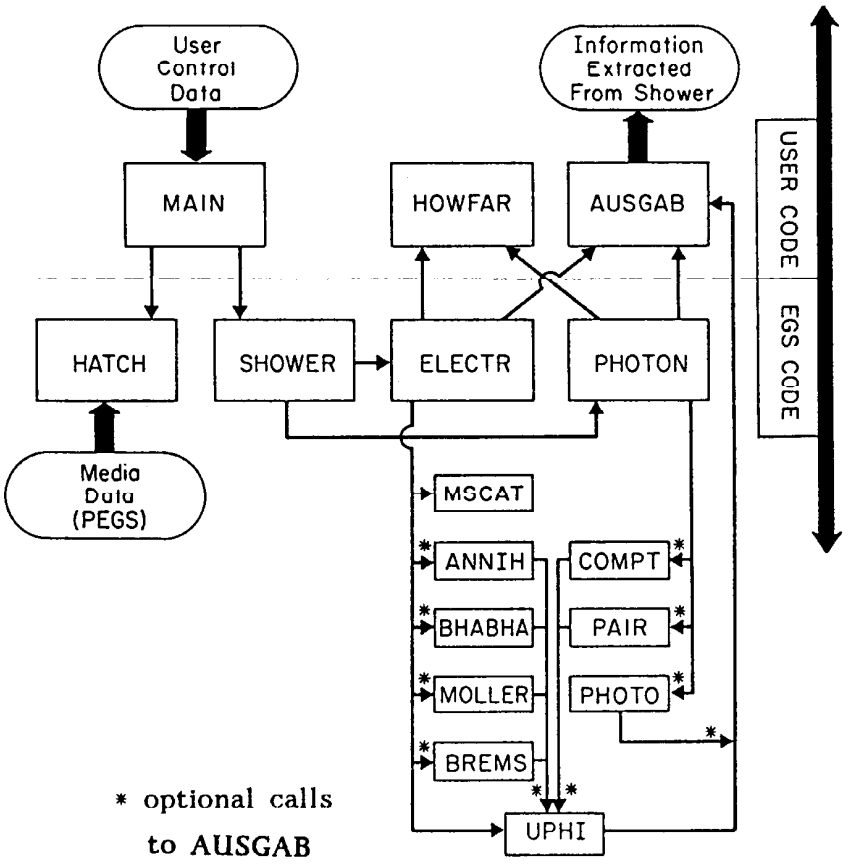

Fig. 2.1 Blockdiagram of EGS 4. Boxes represent subroutines and arrows indicate calls to subroutines.

Therefore the calculation of the polarization states can be done in Ausgab, without affecting the performance of the actual EGS code:
A first call to Ausgab has to be made before a process starts. Here the properties of the incoming particle, i.e. energy, angles and polarization are extracted.
After the process has finished Ausgab is called for a second time. Now the properties of the outgoing particles are extracted and their polarization states are calculated.
For the calculation of the polarization states we make use of various coordinate systems which are defined as follows.

- The geometry of the target, the direction of motion of the particles etc. are defined within a fixed coordinate system X.Y.Z.
- Each particle carries its own coordinate system with the z axis in the direction of propagation of the particle. The y and x axis are orientated in a way that the Y axis of the fixed system is parallel to the y-z plane of the moving system (X axis parallel to the x-z plane).
- We consider only two body reactions which take place in a plane (scattering plane). For the calculation of the processes we need a third coordinate system. Here the y and z axis are within the scattering plane, while the x axis is perpendicular to it.

The calculation for the polarization states is done in steps. The general sequence of these steps may be explained by the example of bremsstrahlung:
The coordinate system of the process is determined by the scattering plane and the direction of motion of the *outgoing* photon. Both are predicted by EGS 4.
At first the polarization of the incoming electron is transformed into this system by means of the matrices $T\varphi$ and $T\Theta$.
Than the calculation of the polarization of the outgoing photon and electron take place.
Finally the polarization is transformed into the particle coordinate systems by means of $T\Psi^{-1}$ or $T\varphi^{-1}$ and $T\Theta^{-1}$ for the photon and the electron, respectively.

Behind the target we average over the polarization of the particles emerging from the target in their respective coordinate systems. This differs from the usual way of defining the polarization of a beam, where a common coordinate system, i.e. the beam axis for the longitudinal polarization, is used. However, since the angles of the accepted positrons are only small and due to symmetry effects the result differs by less than 2%. In addition the projection angle of the spin might be changed in the adiabatic matching device.

2.3.0 Polarization effects in electromagnetic cascades - Discussion of individual processes

We will now consider the polarization effects in the basic processes of an electromagnetic shower. Since only the longitudinal polarization has a long term stability in the shower development, we will concentrate on this.
In the energy band of interest for our purpose (≥ 2 MeV) only pairproduction, bremsstrahlung and compton scattering have significant cross section (see fig. 1.1 and 1.3). Therefore only these processes have been introduced in our code up to now.
Scattering asymmetries which may occur for states of transverse polarization are neglegted. However, transverse polarization is calculated in all processes, to be able to introduce scattering asymmetries if desired.
ξ_3 denotes the longitudinal polarization for all particles, while ξ_2 denotes for electrons the polarization perpendicular to the scattering plane and in case of photons the polarization with respect to the orthogonal states in the scattering plane and perpendicular to the scattering plane, respectively. Thus ξ_1 denotes the polarization in the scattering plane for electrons and 45° to the plane for photons.

2.3.1 Bremsstrahlung & Pairproduction

Bremsstrahlung and pairproduction are essentially inverse processes, as can be seen from the Feynman graphs (fig. 2.2). Hence one can derive the cross section for pair production from the cross section for bremsstrahlung by multiplying both the energy and polarization vector of the outgoing electron by -1, keeping all other variables unchanged [ref. 46].

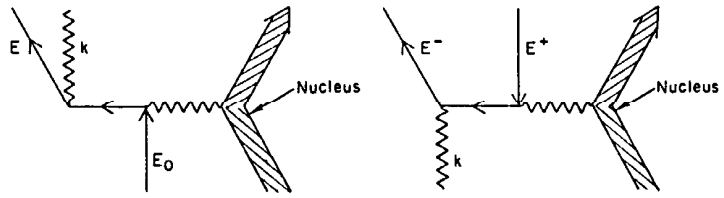

Fig. 2.2 Feynman graphs for bremsstrahlung (left) and pairproduction (right)

We use the cross section which has been calculated by H. Olsen and L. C. Maximon [ref. 46][1]. Using the reduced matrix formalism the polarization of the outgoing particle (electron or positron) can be calculated by means of

1 It should be mentioned, that a sign error occurs in a previous paper of Olsen and Maximon [ref. 47] and in Mc Masters paper [ref. 42], which is corrected in the later paper ref. 46.

the transfer matrix:

$$T = \begin{bmatrix} 1 & 0 & D & 0 \\ 0 & 0 & 0 & E \\ 0 & 0 & 0 & 0 \\ 0 & 0 & 0 & L \end{bmatrix}$$

$$I = (\varepsilon^2 + (\varepsilon - k)^2)(3 + 2\Gamma) - 2\varepsilon(\varepsilon - k)(1 + 4u^2\zeta^2\Gamma)$$
$$D = \{8\varepsilon(\varepsilon - k)\, u^2\zeta^2\Gamma\}/I$$
$$E = \{4k(\varepsilon - k)\,\zeta u(1 - 2\zeta)\Gamma\}/I$$
$$L = k\{(\varepsilon - (\varepsilon - k))(3 + 2\Gamma) + 2(\varepsilon - k)(1 + 4u^2\zeta^2\Gamma)\}/I$$

ε = energy of the outgoing electron/positron in units of mc^2
$k \equiv$ energy of the photon in units of mc^2
$u = |\vec{u}|$
$\vec{u} \equiv$ component of $\vec{p}$ perpendicular to $\vec{k}$
$\vec{p} \equiv$ electron/positron momentum in units of mc
$\vec{k} \equiv$ momentum of the photon in units of mc
$\zeta \equiv 1/(1 + u^2)$

Γ contains the Coulomb and screening effects:

$$\Delta \equiv \frac{12\, Z^{\frac{1}{3}}\varepsilon(\varepsilon - k)\zeta}{121\, k} \qquad Z = \text{atomic number}$$

$$\delta \equiv \frac{k}{2\varepsilon(\varepsilon - k)}$$

$$\Gamma = \ln(1/\delta) - 2 - f(Z) + \mathcal{F}\left(\frac{\zeta}{\delta}\right) \qquad \text{for } \Delta \leq 120$$

$$\Gamma = \ln\left(111/(\zeta Z^{\frac{1}{3}})\right) - 2 - f(Z) \qquad \text{for } \Delta > 120 \text{ (complete screening)}$$

$f(Z)$ is the Coulomb correction term that was derived by Davies, Bethe and Maximon [ref. 48]. We use an approximative formula given in ref. 18 (Eq. 2.7.17).

$\mathcal{F}\left(\frac{\zeta}{\delta}\right)$ contains the screening effects and is zero for $\Delta < 0.5$ (No screening). For $0.5 \leq \Delta \leq 120$ (intermediate screening) it is a slowly decreasing function. Tabulated values for $\mathcal{F}\left(\frac{\zeta}{\delta}\right)$ are used [ref. 49] with a linear interpolation in between.

The term D in the transfer matrix leads to an asymmetry in the angular distri-

bution if the photon is transversely polarized. This effect is neglected in our calculations.

Fig. 2.3 shows the longitudinal polarization of the produced particle (electron or positron) as a function of its fractional energy ε/k (incoming γ-beam: 20 MeV, $\xi_3 = +1$).

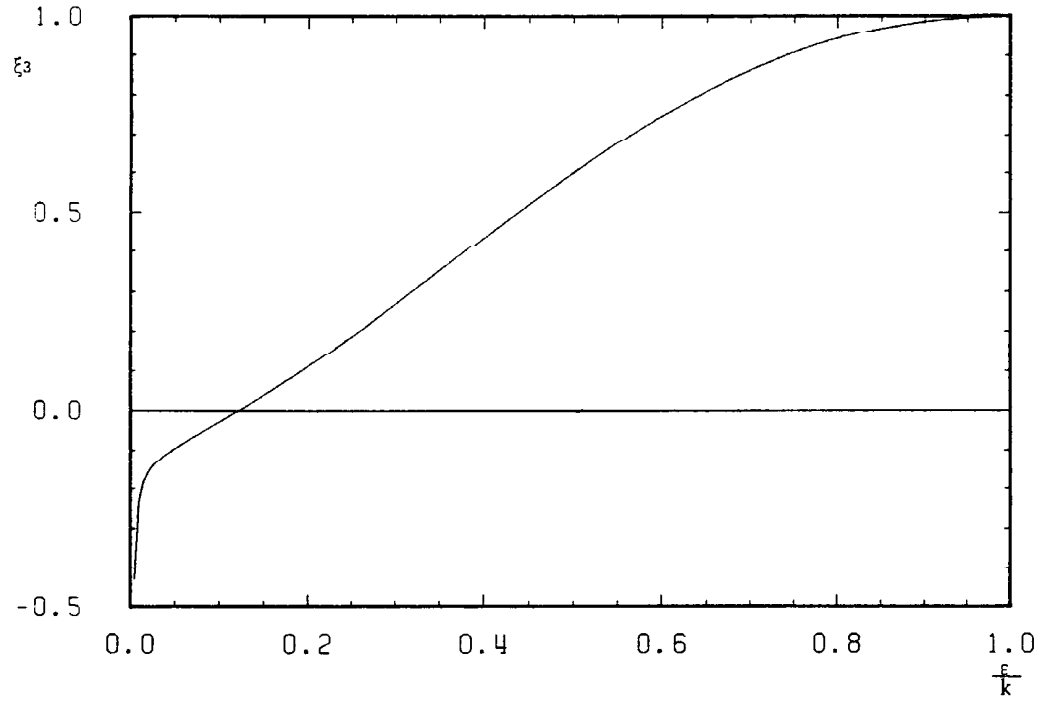

Fig. 2.3 Circular polarization of particles produced in pairproduction process as a function of the fractional energy

(The plot differs from the plots in ref. 46 where the polarization for a fixed emission angle is shown, while here the emission angle is a function of the fractional energy which is calculated by EGS.)

The polarization of the photon is transfered to the particles with the highest energy, while it has the opposite sign for low energy particles. The production probability as function of the fractional energy is plotted in fig. 1.2. It shows a roughly flat distribution for all particle energies.

Due to the inverse nature of bremsstrahlung and pairproduction, the transfer matrix for the photon generated in a bremsstrahlung process is given by:

$$T = \begin{bmatrix} 1 & 0 & 0 & 0 \\ 0 & 0 & 0 & 0 \\ D & 0 & 0 & 0 \\ 0 & E & 0 & L \end{bmatrix}$$

$$I = (\varepsilon_1^2 + \varepsilon_2^2)(3+2\Gamma) - 2\varepsilon_1\varepsilon_2\,(1+4u^2\zeta^2\Gamma)$$
$$D = \{8\varepsilon_1\varepsilon_2\,u^2\zeta^2\Gamma\}/I$$
$$E = \{4k\varepsilon_2\zeta u(2\zeta-1)\Gamma\}/I$$
$$L = k\{(\varepsilon_1+\varepsilon_2)(3+2\Gamma) - 2\varepsilon_2(1+4u^2\zeta^2\Gamma)\}/I$$

$\varepsilon_1 \equiv$ energy of the incoming electron/positron in units of mc^2
$\varepsilon_2 \equiv$ energy of the outgoing electron/positron in units of mc^2
$\mathbf{p} \equiv$ electron/positron initial momentum in units of mc
$k \equiv$ energy of the photon in units of mc^2
$u = |\vec{u}|$
$\vec{u} \equiv$ component of $\vec{p}$ perpendicular to $\vec{k}$
$\vec{p} \equiv$ electron/positron momentum in units of mc
$\vec{k} \equiv$ momentum of the photon in units of mc

As in the case of pairproduction the high energy photons carry the longitudinal polarization of the incoming particle.
For our purpose the polarization of the electron/positron after the bremsstrahlungs process is of even greater interest than the polarization of the generated photon. This cross section is not explicitly given in the paper of Olsen and Maximon, however, it can be derived from the cross section $d\sigma(\mathbf{p}, \zeta_1, \zeta_2, \mathbf{k}, \mathbf{e})$ (eq. 5.7 in ref. 46) which still contains the polarization states of all particles involved.
The relation:

$$\overline{(\vec{a}\cdot\vec{e})\,(\vec{b}\cdot\vec{e}^{*})} = \frac{1}{2}\left\{\vec{a}\cdot\vec{n} - (\vec{a}\cdot\vec{n})\,(\vec{b}\cdot\vec{n})\right\} \quad [\text{ref. 50}]$$

$\vec{e} \equiv$ polarization vector of the photon
$\vec{a}, \vec{b} =$ vectors
$\vec{n} \equiv$ unit vector in the direction of motion of the photon

is needed to sum over the polarization states of the outgoing photon.
We found the following transfer matrix:

$$T = \begin{bmatrix} 1 & 0 & 0 & 0 \\ 0 & M & 0 & E \\ 0 & 0 & M & 0 \\ 0 & F & 0 & M+P \end{bmatrix}$$

$$I = (\varepsilon_1^2 + \varepsilon_2^2)(3+2\Gamma) - 2\varepsilon_1\varepsilon_2\,(1+4u^2\zeta^2\Gamma)$$
$$F = \varepsilon_2\{4k\,\zeta u(1-2\zeta)\Gamma\}/I$$
$$E = \varepsilon_1\{4k\,\zeta u(2\zeta-1)\Gamma\}/I$$
$$M = \{4\varepsilon_1\varepsilon_2(1+\Gamma-2u^2\zeta^2\Gamma)\}/I$$
$$P = \{k^2(1+8\Gamma(\zeta-0.5)^2\}/I$$

Fig. 2.4 shows the longitudinal polarization of an 20 MeV electron as function of its energy $\varepsilon_2 = \varepsilon_1 - k$ after bremsstrahlung as produced by EGS. It can be seen that even if the particle loses half of its energy, the polarization loss is below 20%.

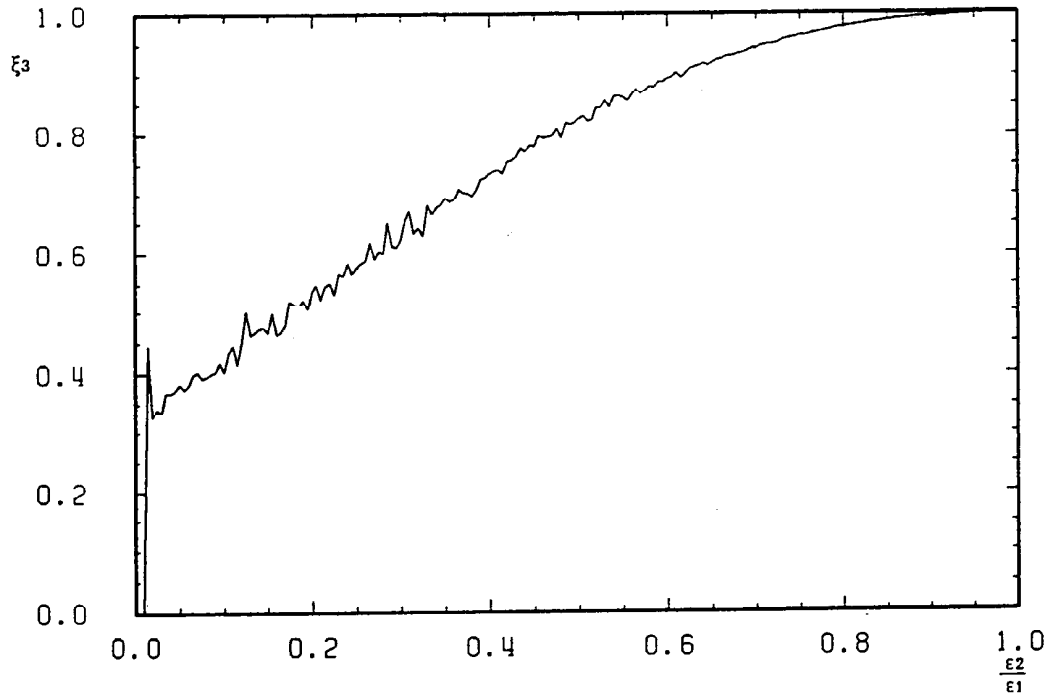

Fig. 2.4 Longitudinal polarization of positrons after bremsstrahlung as a function of the fractional energy loss

2. 3. 2 Compton scattering

The ratio of the cross section for Compton scattering to the pair production cross section scales inversely with the atomic number Z. Hence it is somewhat larger in a light material ($Z_{tungsten} / Z_{titanium} \sim 3$). However, the Compton cross section scales for $E_\gamma > 1\,MeV$ roughly proportional to $1 / E_\gamma$. Thus the overlap with the pair production cross section is only small. (See fig. 1.1 for comparison.)

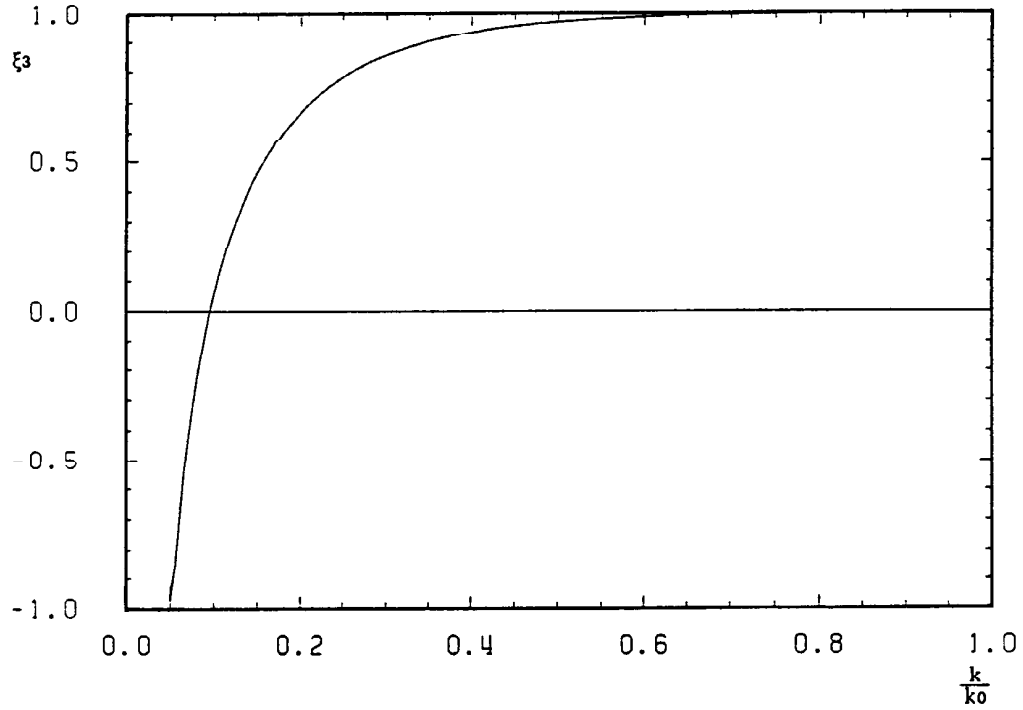

Fig. 2.5 Circular polarization of Compton scattered photons as function of the fractional energy loss

Complete cross sections for Compton scattering have been worked out by F. W. Lipps and H. A. Tolhoek [ref. 51]. For unpolarized target electrons the polarization transfer matrix for the outgoing photon is given by:

$$T = \begin{bmatrix} 1 & 0 & \frac{\sin^2\vartheta}{I} & 0 \\ 0 & \frac{2\cos\vartheta}{I} & 0 & 0 \\ \frac{\sin^2\vartheta}{I} & 0 & \frac{1+\cos^2\vartheta}{I} & 0 \\ 0 & 0 & 0 & \frac{2\cos\vartheta}{I} + \frac{(k_0-k)\cos\vartheta(1-\cos\vartheta)}{I} \end{bmatrix}$$

$$I = 1+\cos^2\vartheta + (k_0 - k)(1-\cos\vartheta)$$

$\vec{k}_0$ = momentum of the incoming photon; $k_0 = |\vec{k}_0|$

$\vec{k}$ = momentum of the outgoing photon; $k = |\vec{k}|$

$$\cos\vartheta = \frac{\vec{k}_0 * \vec{k}}{k_0 * k}$$

Fig. 2.5 shows the longitudinal polarization of the photon after Compton scattering as function of its fractional energy. The polarization remains unchanged even for large energy losses.

2.4.0 Results
- Polarized positrons formed by monoenergitc photons

Before we investigate the polarization effects in a positron source based on undulator radiation, we study the influence of the target thickness and the target material by means of a monoenergetic photon beam. These material dependent effects are not so prominent in the case of undulator radiation due to the complicated spectrum with varying polarization.
In fig. 2.6 the polarization of the positrons emerging from the titanium target is plotted for various target thicknesses. As primary beam 20 MeV photons with longitudinal polarization $\xi_3 = 1$ have been used. A comparison with fig. 2.3 and fig. 2.4 shows that only for very thin targets the spectrum of the polarization is determined by the production process, while for targets of 0.4 X_0 it is equivalent to the polarization obtained after bremsstrahlung. Particles which are produced with only a small fraction of energy get lost in the thicker target, while these energy bands are repopulated with positrons which were produced with a higher energy and higher polarization. Hence the *mean* polarization is higher for a thicker target!
From the pair production process (fig. 2.3) one might conclude that one has to select the high energy part of the positron spectrum to get a higher polarization. However, this is not the case and the effect of a selective capture optics is only small as will be shown later.
Fig. 2.7 shows the polarization of positrons emerging from a 0.4 X_0 thick target for various materials. The mean polarization is $\xi_3 = 0.71$ for titanium, and $\xi_3 \equiv 0.66$ for tungsten which might be regarded as the maximum polarization which can be obtained with a target thickness of 0.4 X_0 and no special capture optics.

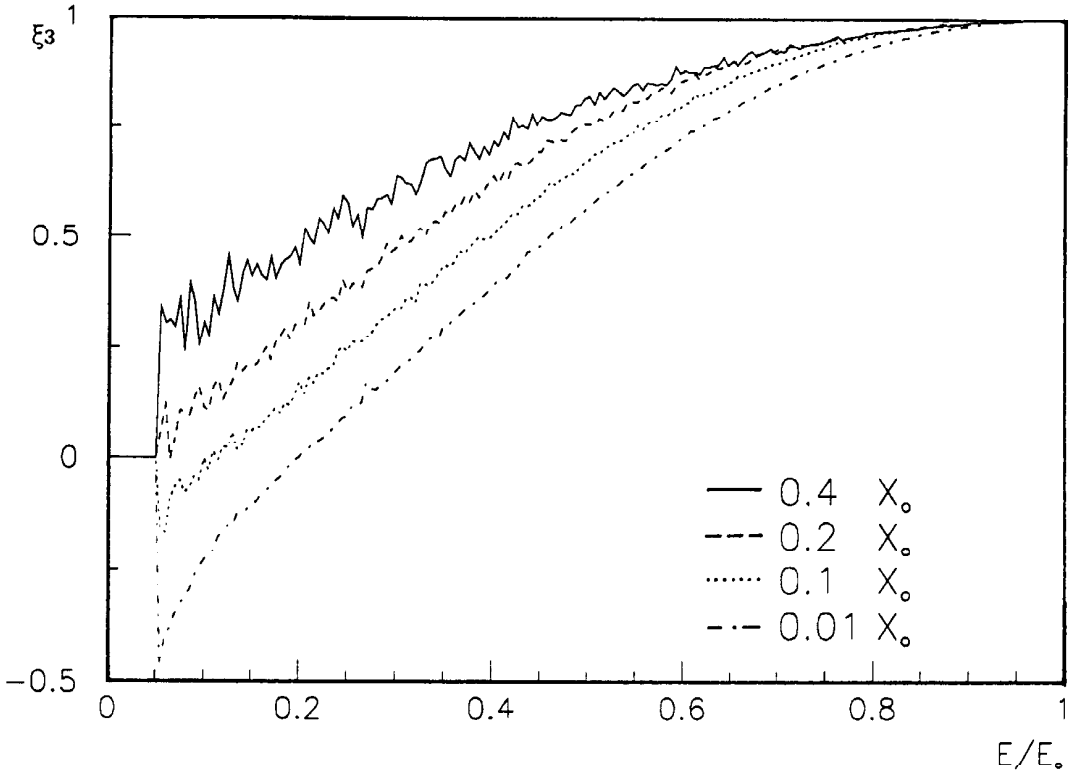

Fig 2.6 Influence of the target thickness on the polarization of positrons emerging from a titanium target

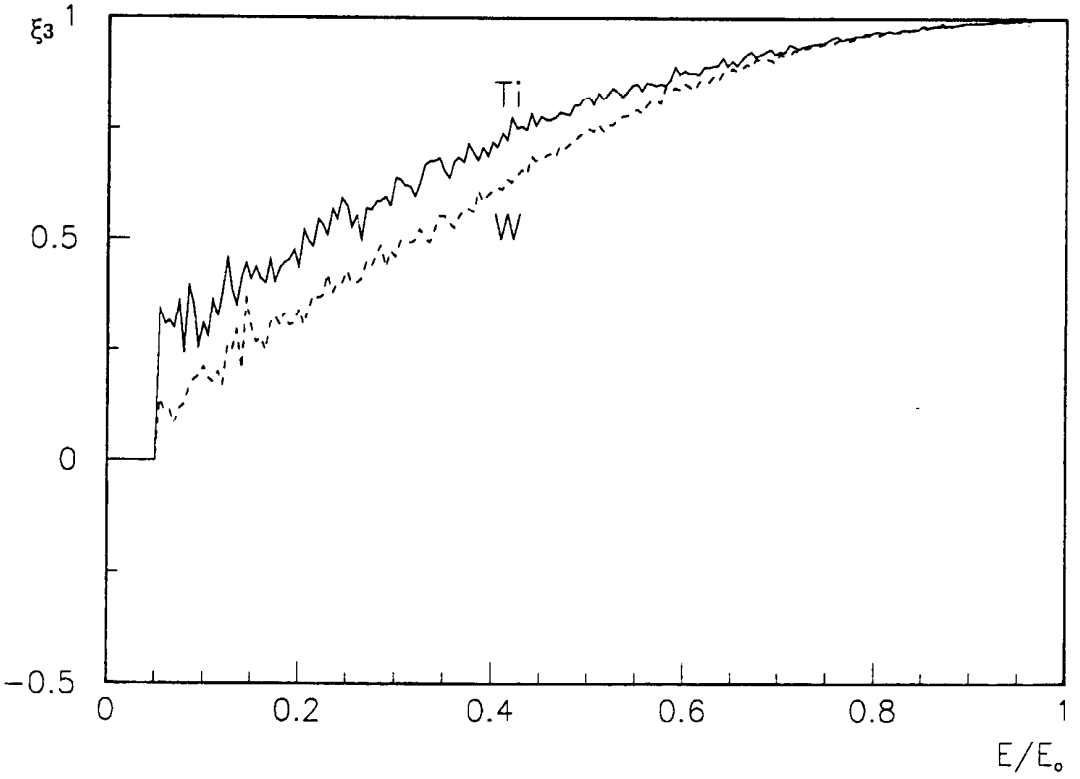

Fig. 2.7 Influence of the target material on the polarization of positrons emerging from a target of thickness 0.4 X_0.

Polarization characteristics of helical undulator radiation

In extension of the discussion in chapter 1.2.2 we will now consider the polarization characteristics of helical undulator radiation.
The Lienard-Wiechert integral (see eq. 1.5) has the general form:

$$I(\omega,\Omega) = \frac{c}{4\pi^2} \left| \int R(t) \cdot Ex(t) \cdot e^{i\omega t} dt \right|^2 \left| \int R(t) \cdot Ey(t) \cdot e^{i\omega t} dt \right|^2$$

$$= \left| Ix(\omega,\Omega) \right|^2 + \left| Iy(\omega,\Omega) \right|^2$$

$Ex(\omega,\Omega)$ and $Ey(\omega,\Omega)$ represent complex field amplitudes of the radiation field and $R(t)$ is the distance between the observer and the emitter at the retarded time. We will consider the far field approximation now, where the distance D from the end of the undulator to the observer is much larger than the length L of the undulator itself: $D \gg L$. (Near field effects will be discussed in ch. 5.2.1.)
Here R can be treated as a constant and the polarization can be calculated by setting:

$$|Ix|^2 = \frac{1}{2} \langle Ax Ax^* \rangle$$

$$|Iy|^2 = \frac{1}{2} \langle Ay Ay^* \rangle \qquad \text{see eq. 2.1}$$

The Stokes parameters can now be calculated by means of the formulae 2.2, 2.3 and 2.4 .
For the helical undulator we obtain for the field amplitudes (see ch. 1.2.2 for comparison):

$$Ix(E) = \sum_{n=1}^{\infty} \left[\frac{10^6 e^3}{4\pi\varepsilon_0 \hbar^2 c^2} \right]^{1/2} \frac{K}{\gamma} * \left[\frac{\alpha_n}{K} - \frac{n}{x} \right] J_n(x) * \delta(\gamma^2\Theta^2 - \alpha_n^2)$$

$$Iy(E) = i \sum_{n=1}^{\infty} \left[\frac{10^6 e^3}{4\pi\varepsilon_0 \hbar^2 c^2} \right]^{1/2} \frac{K}{\gamma} * J'_n(x) * \delta(\gamma^2\Theta^2 - \alpha_n^2) \qquad (2.6)$$

$$\alpha_n^2 = \left[n * \frac{\omega_1 (1+K^2)}{\omega} - 1 - K^2 \right]$$

$$x = 2 * K * \frac{\omega}{\omega_1 (1+K^2)} * \alpha_n$$

$$\omega_1 = \frac{4\pi\gamma^2 c}{(1+K^2)\lambda_u}$$

$J_n \equiv$ Bessel functions

$\Theta \equiv$ observation angle with respect to the undulator axis.

i.e. Ix has only a real component, while Iy has only an imaginary component.

In this case the calculation of the Stokes parameters is further simplified and we get for the circular polarization:

$$\xi_3 = \frac{2\,I_x\,I_y}{I_x^2 + I_y^2}$$

The natural line shape of the radiation has the form $\sin^2 N\pi\,(\frac{\omega - n\omega_1}{\omega_1}) \Big/ (\frac{\omega - n\omega_1}{\omega_1})^2$ (N ≡ number of undulator periods, $\omega_1 = \omega_1(\Theta)$) and is approximated by a δ-function.
From

$$\gamma^2\Theta^2 - \alpha_n^2 = 0$$

we obtain the half opening angle of the radiation cone Θ to be:

$$\Theta = \frac{\alpha_n}{\gamma} = \frac{1}{\gamma} * \left[n * \frac{\omega_1\,(1+K^2)}{\omega} - 1 - K^2 \right]^{1/2} \qquad (2.7)$$

Beside these complex formulae an instructive way of viewing the radiation pattern of the helical undulator radiation is to consider the motion of the electron in the laboratory frame and in a moving frame which moves with the velocity of the electron in the direction of the undulator axis (see fig. 2.8).
In a weak undulator with the undulator parameter $K \simeq B[T] * \lambda u[cm] << 1$ (eq. 1.6) the electron moves with non relativistic velocity on a circle and radiates a dipole pattern like it is sketched in fig. 2.8 . The intensity has a maximum in the forward and backward direction and a minimum radial to the circle of motion ($\Theta' = \pi/2$). In the laboratory frame the radiation is boosted into the forward direction and we observe the radiation spectrum, plotted in fig. 2.9 (first harmonic), with a maximum intensity at its highest energy (from the photons in forward direction) and at its lowest energy (from the photons in backward direction). The highest energy of this spectrum is the characteristic energy of the spectrum as defined in eq. 1.7 .
In an undulator with increasing K-value the motion of the electron in the moving frame becomes more and more relativistic and the radiation forms a synchrotron radiation pattern.
Obviously only harmonics of the fundamental frequency i.e. the rotation frequency occur. However, due to the angular distribution of the radiation we observe harmonic bands rather than a line spectrum in the laboratory frame. Since the radiation of the higher harmonics is radiated more and more radial to the circle of motion in the moving frame ($\Theta' = \pi/2$), the maximum intensity is more and more concentrated at the middle energy of the harmonic bands in the laboratory frame. Fig 2.9 shows examples of harmonics for K = 0.7 .

The harmonic bands of the radiation are represented in equations 1.8 and 2.6 by single terms of the sum. Adding all harmonics we obtain the spectrum of fig. 1.5.

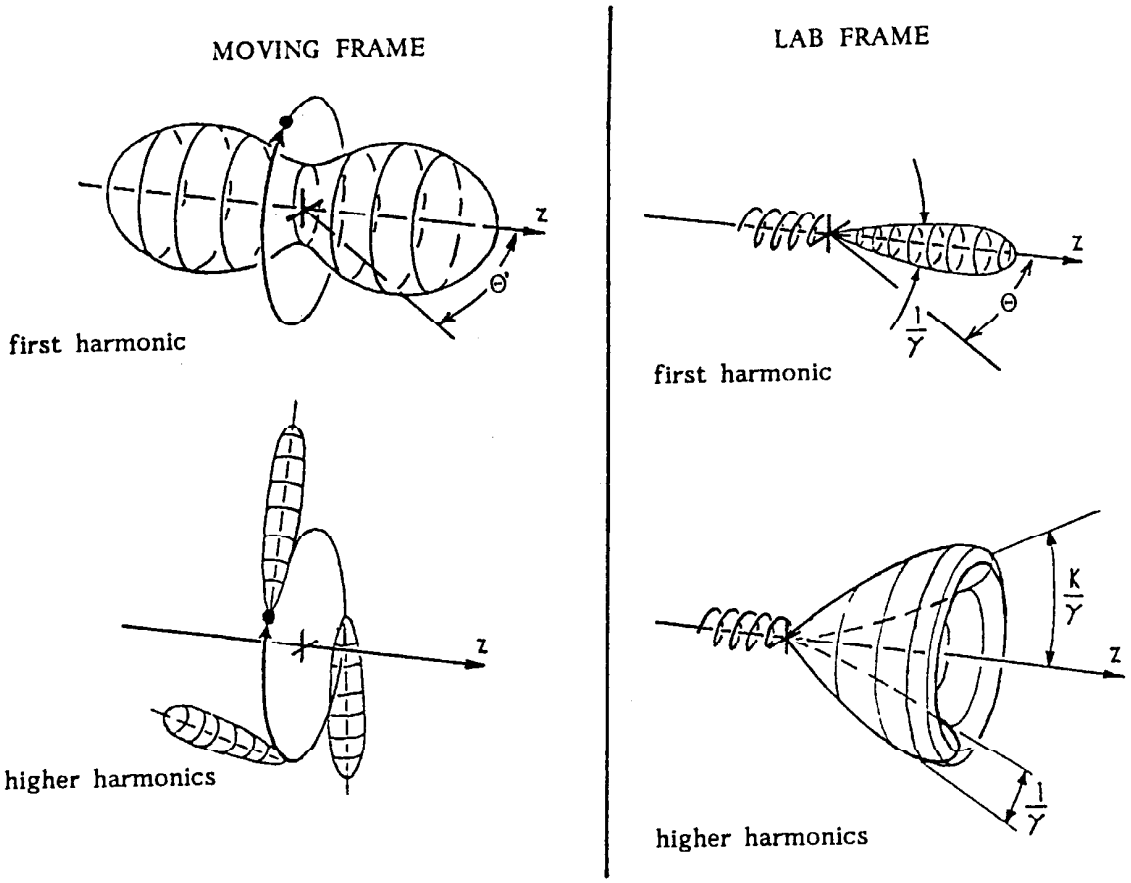

Fig. 2.8 Radiation pattern of a helical undulator in a moving frame and in the laboratory frame

The lower scale in fig. 2.9 shows the emission angle of the radiation which is connected to the energy according to eq. 2.7. The maximum energy $n\omega_1$ is radiated on the undulator axis, while the lower energies are radiated into a cone with increasing opening angle.
However, since only the first harmonic has the maximum of radiation at the upper energy limit, we can conclude that only the first harmonic radiates a significant part of its intensity on the undulator axis.
In fig. 2.10 the circular polarization ξ_3 and the transverse polarization ξ_1 are plotted versus the fractional energy, while fig. 2.11 shows the polarization state versus the emission angle. (ξ_2 is always zero in our coordinate system.)
The polarization distribution of the individual harmonics is nearly independent of the harmonic number and, apart from the normalisation of the emission angle, nearly independent of the K-value.
The functional dependence can be explained by means of the transformation properties from the moving frame into the laboratory frame. The highest energy corresponds to the emission in the forward direction in the moving frame. Here we see the particle moving on a circle, hence the radiation is circularly polarized. The mean energy corresponds to the radiation emitted radial to the circle of

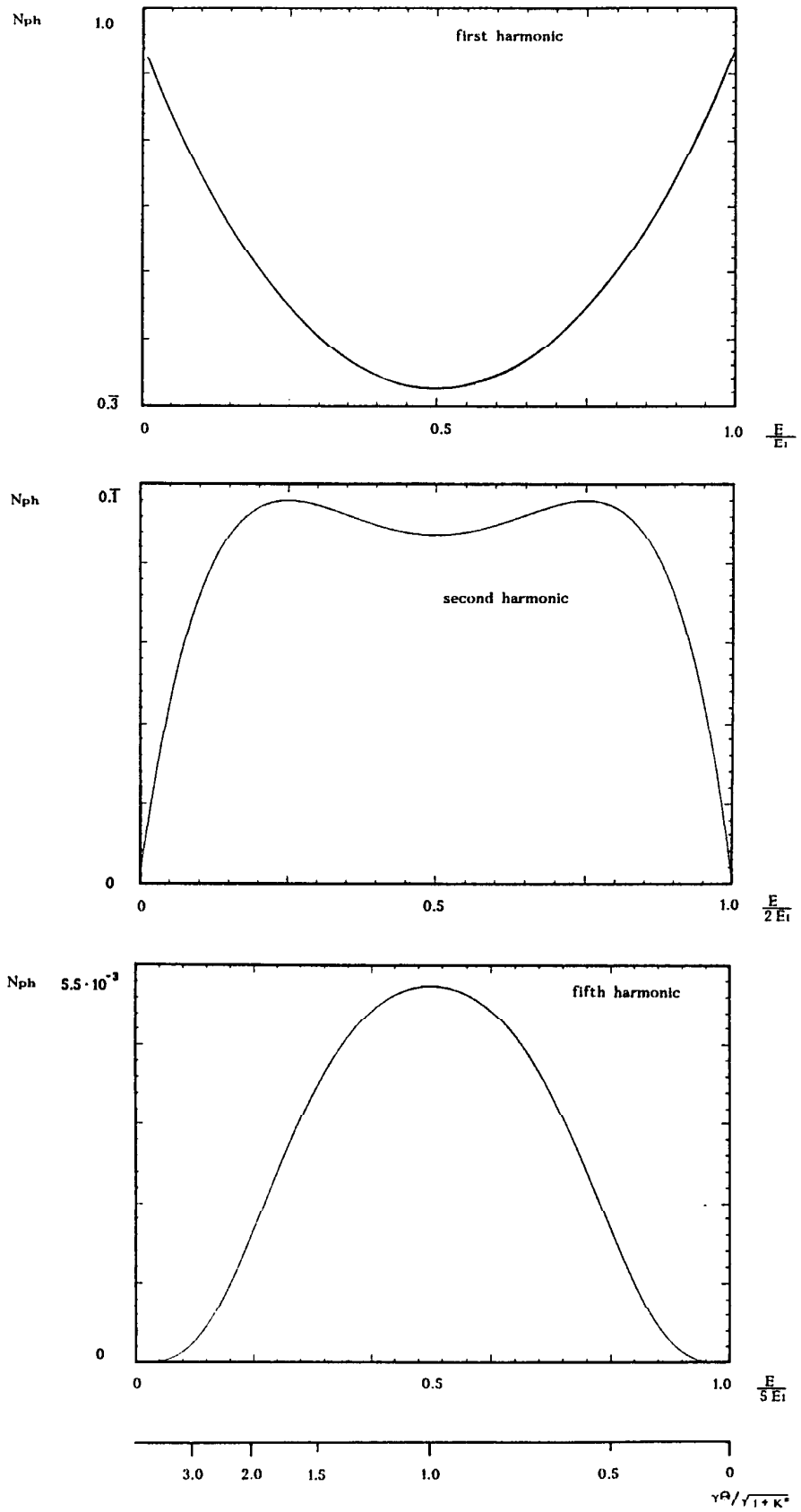

Fig. 2.9 First harmonic, second harmonic, and fifth harmonic of helical undulator radiation, K = 0.7, vertical axis in arbitrary units. Lowest scale: normalized emission angle. See fig. 1.5 for comparison.

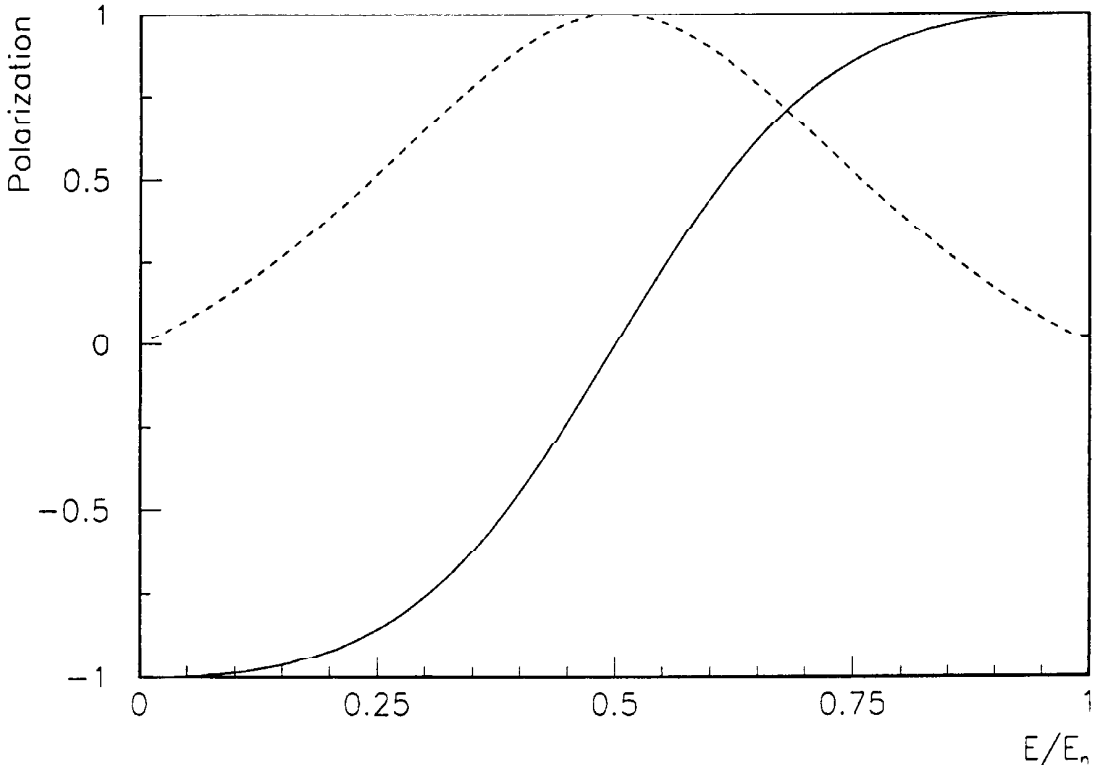

Fig. 2.10 Circular (solid line) and transverse (broken line) polarization versus fractional energy, K = 0.7

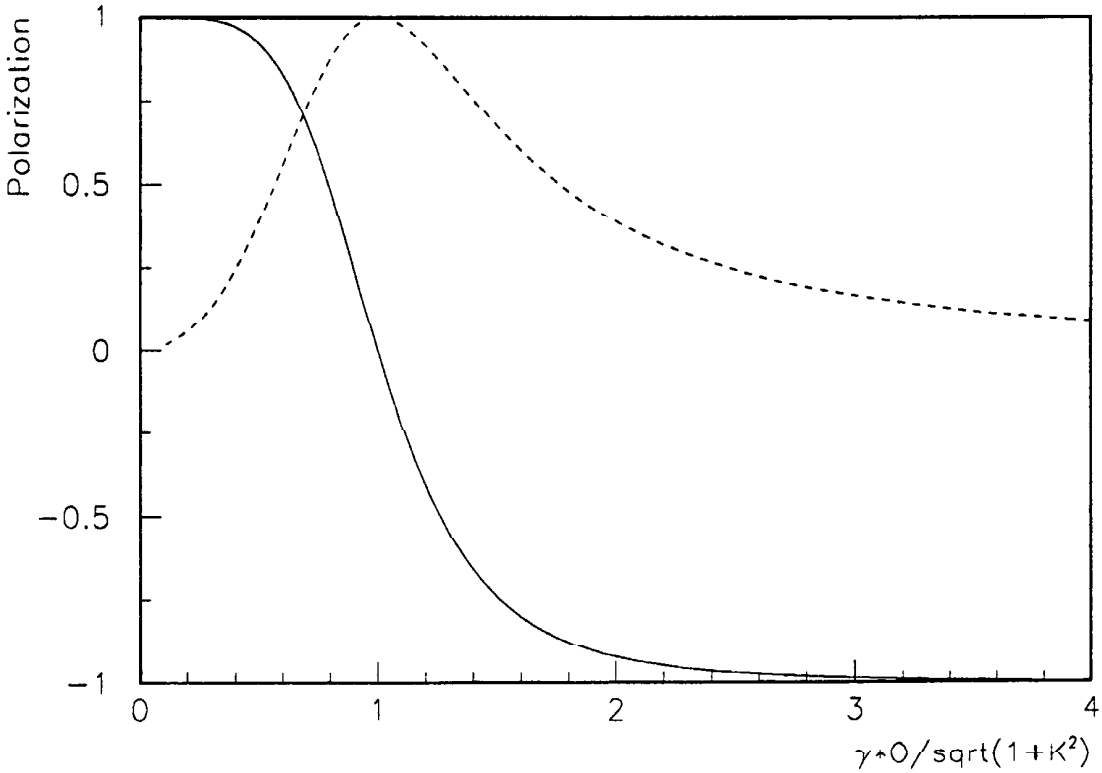

Fig. 2.11 Circular (solid line) and transverse (broken line) polarization versus normalized emission angle, K = 0.7

motion in the moving frame. Here we see the particle moving up and down, hence the circular polarization is zero, but the transverse polarization ξ_1 is one.

Going further down in energy we see the particle from the backside. It moves again on a circle, but in the opposite direction, hence the polarization goes down to -1.
We can neglect the negative polarization of the low energy photons of the first harmonic, since they anyway take no part in pair creation. The higher harmonics, however, radiate at maximum at their mean energy where the circular polarization is zero. Therefore we have either to use an undulator with low K-value to suppress the higher harmonics or scrape the unpolarized photons off. This is possible since they are not emitted along undulator axis. A scraped undulator beam also becomes more and more monoenergetic with decreasing scraper angle and the positron production will be simillar to the simulations with the monoenergetic photon beam.

2.5.1 Near field effects

If the distance D between observer and undulator is of the order of the undulator length, the undulator can no longer be treated as a point like source.
For $D \geq L$ we consider the undulator assembled out of pieces of length l, so that on the one hand $D \gg l$ is fulfilled for every piece, but on the other hand there is still a large number of periods in every piece. Since we are interested in a long undulator with small period length ($L \sim 100\,m$, $\lambda u \sim 1\,cm$, $N \sim 1 \cdot 10^4$) both conditions can be fulfilled.
The geometrical line width given by $\sin^2 N\pi \left(\frac{\omega - n\omega_1}{\omega_1}\right) \Big/ \left(\frac{\omega - n\omega_1}{\omega_1}\right)^2$ is even for smaller N ($N = 50 - 100$) well approximated by a δ-function, so that every piece of the undulator emits a line spectrum into a given direction.
At the observation point contributions from the various undulator pieces add up. However, due to their different angles they have different frequencies and the polarizaton is not changed due to a coherent superposition of waves with the same frequency.
Hence the polarization can be approximated by:

$$\xi_3(\omega, x, D) = \int_{\Theta_1}^{\Theta_2} \xi_3(\omega, \Theta) \cdot I(\omega, \Theta)\, d\Theta \Big/ \int_{\Theta_1}^{\Theta_2} I(\omega, \Theta)\, d\Theta$$

$x \equiv$ distance of the observation point from the undulator axis

$\Theta_1, \Theta_2 \equiv$ emission angle with respect to the beginning and the end of the undulator

Obviously the near field effect for $D \geq L$ is zero on the axis and only small as long as $x/D < 1/\gamma \sqrt{1 + K^2}$.
Since the condition $D \geq L$ can be fulfilled in case of our positron source, we will not consider the case $D < L$, where the polarization may be changed due to a coherent superposition of waves with the same frequency.

2.4.0 Results
- Polarized positrons formed by helical undulator radiation

We will now investigate the polarization properties of a positron source based on the radiation of a helical undulator. In order to increase the polarization of the positrons, we will discuss the effect of an energy scraping of the positron beam and a geometric scraping of the photon beam, respectively.
Fig. 2.12 shows the longitudinal polarization of the positrons emerging from the target (0.4 Xo titanium) and behind the capture optics as a function of energy.

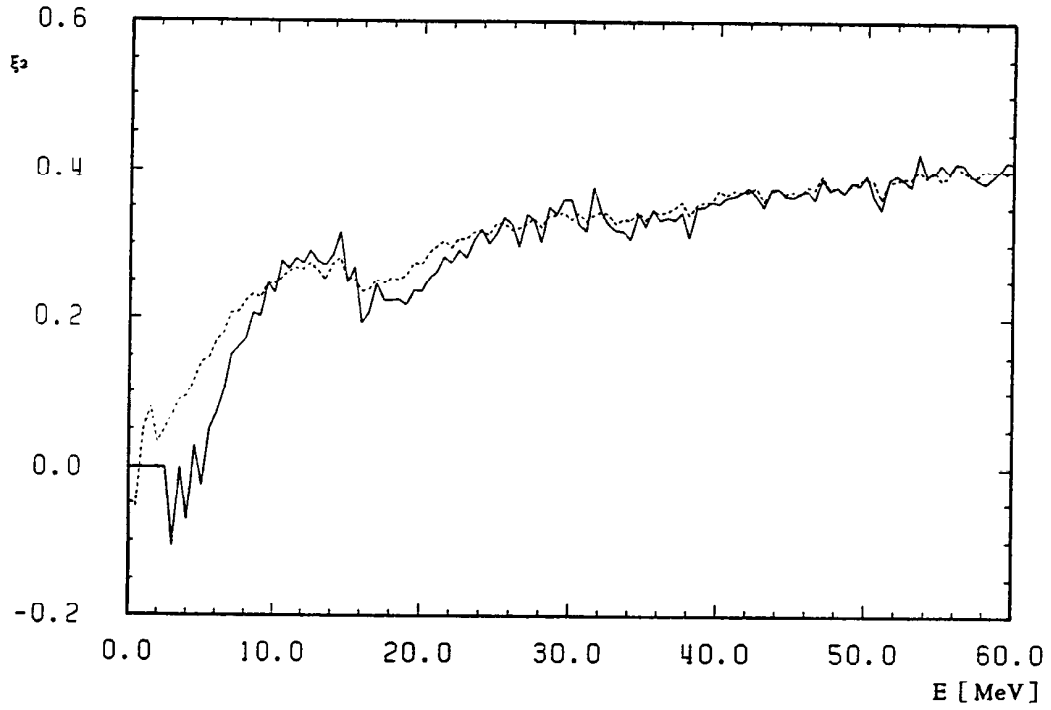

Fig. 2.12 Circular polarization of positrons versus energy emerging from the target (dotted line) and behind the capture optics (solid line), K = 1, E_1 = 20 MeV

Owing to a correlation of the energy loss due to bremsstrahlung and large scattering angles which is caused by the path-length of the charged particle in the target, the effect of the bremsstrahlung on the polarization is somewhat compensated by the capture optics, because here only particles with small scattering angles are collected. Hence the polarization which is equilized by the bremsstrahlung process, is structured again by the capture optics (see fig. 2.3 and 2.4 for comparison). The mean polarization is, however, not significantly affected by the capture optics.
The polarization at low energy is formed by a superposition of positrons which are produced from low energy, highly polarized photons (from the first harmonic), from low energy, weakly polarized photons (from the higher harmonics) and from high energy, highly polarized photons either via production at low energy (fig. 2.3) or by energy loss due to bremsstrahlung (fig. 2.4).

In total the polarization is highest for the high energy positrons. However, the maximum number of particles is at lower energy (see fig. 1.17). Therefore the effect of a spectroscopic optics which offers the possibility to scrape off low energy particles is only small, if a reasonable yield is required.
Fig. 2.13 shows the capture efficiency of a spectroscopic optics as a function of the cut off energy Eb and the respective polarization.

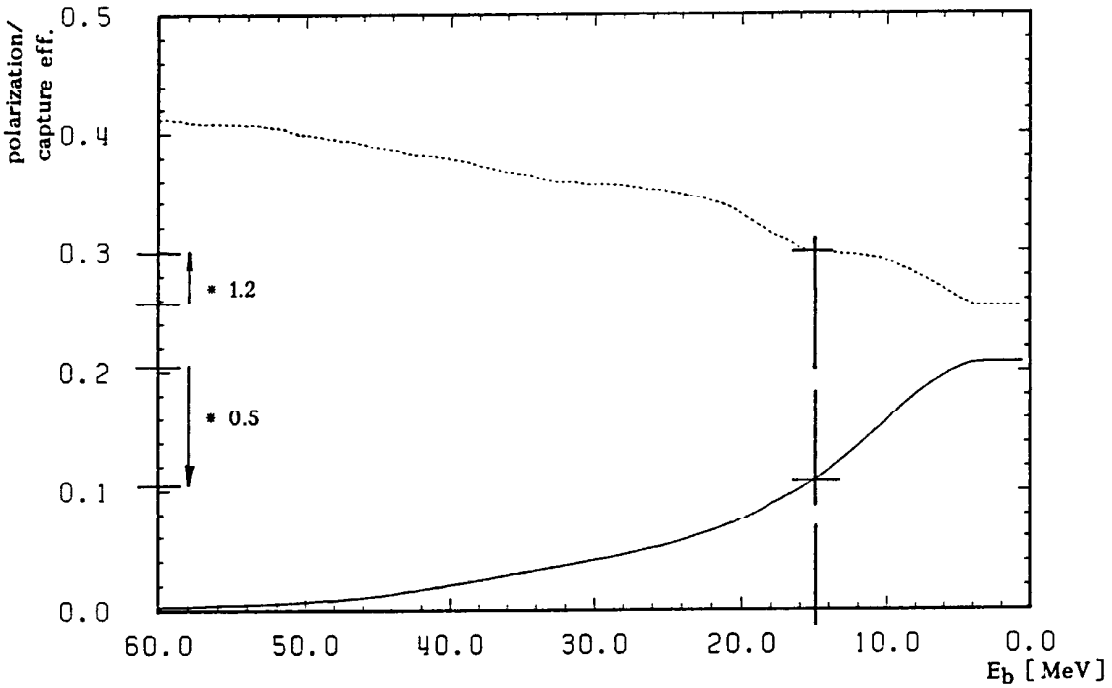

Fig. 2.13 Effect of a cut off energy Eb on the capture efficiency (solid line) and on the polarization (dotted line). The arrows indicate the loss in the capture efficiency and the gain in the polarization, respectively.

If we introduce a cut off at ~15 MeV, so that particles with E>15 MeV are collected, the capture efficiency decreases by a factor of 2 from about 20% to ~10%, while the polarization of the beam is increased by a factor of only 1.2 from ~25% to ~30%.
The effect is shown in fig. 2.14 for various K-values. Here the polarization is plotted versus the capture efficiency. The slope of the curves is roughly independent of the K-value. As expected, the polarization increases with decreasing undulator parameter, however, even for K = 0.5 the polarization stays below the polarization of positrons formed by monoenergetic photons. In addition the undulator has to be very long in the case of low K-values, roughly 1000 m for K = 0.5 (see eq. 1.9 and fig 1.6).

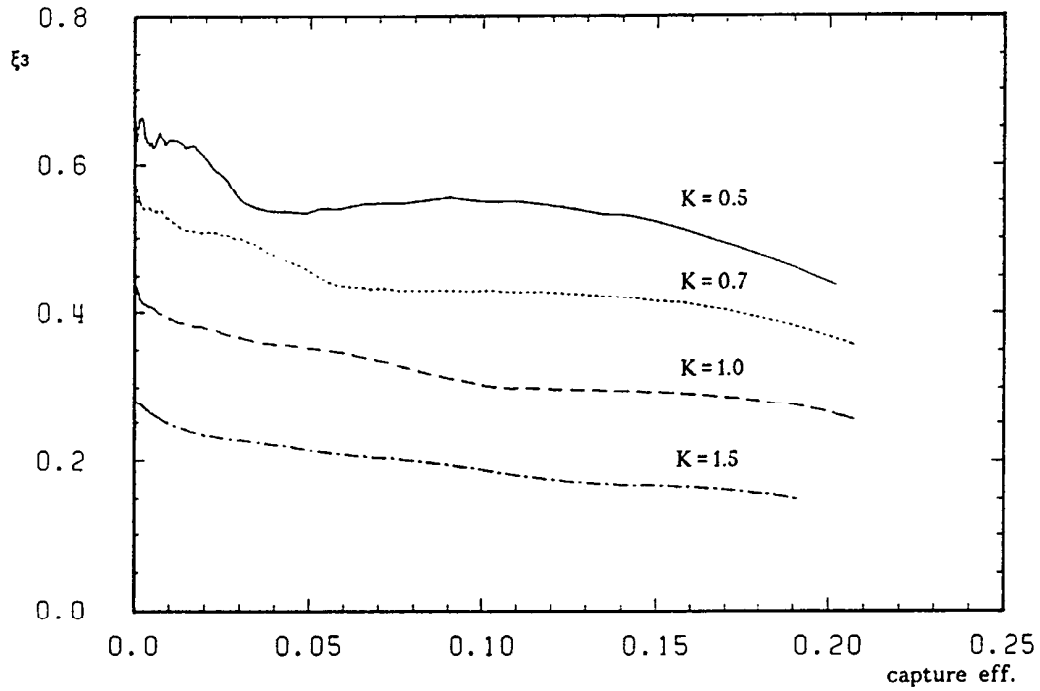

Fig. 2.14 Polarization versus capture efficiency for various undulator parameters K

Variation of the energy of the first harmonic E_1 has no significant effect on the polarization within the range of E_1 = 10 MeV up to 30 MeV, but as already mentioned it does affect the yield (fig. 1.8).
We discuss now the effect of scraping the undulator radiation on the positron polarization. We will neglect the influence of the beam emittance of the primary beam here. That will be discussed in ch. 2.7.0.
The opening angle of the radiation of the helical undulator is $\sim 1/\gamma$ for $K \leq 1$. Therefore the rms-spot size of the radiation σ_{rad} is approximatively:

$$\sigma_{rad} \simeq \frac{1}{\gamma} \left(\frac{L}{2} + D \right)$$

In order to reduce the thermal stress in the target to a reasonable level, the spot size has to be of the order of

$$\sigma_{rad} \approx (0.5 - 1.0) \cdot 10^{-3} \text{ m}$$

We get $\left(\frac{L}{2} + D \right) \approx 250 - 500$ m

In addition $D > L$ should be fullfilled in order to reduce near field effects and allow an efficient scraping of the γ-beam.
For the following calculations we have chosen L = 100 m and D = 350 m. Near field effects are included in the simulation as a statistical mixture of polarized photons starting at various points in the undulator.

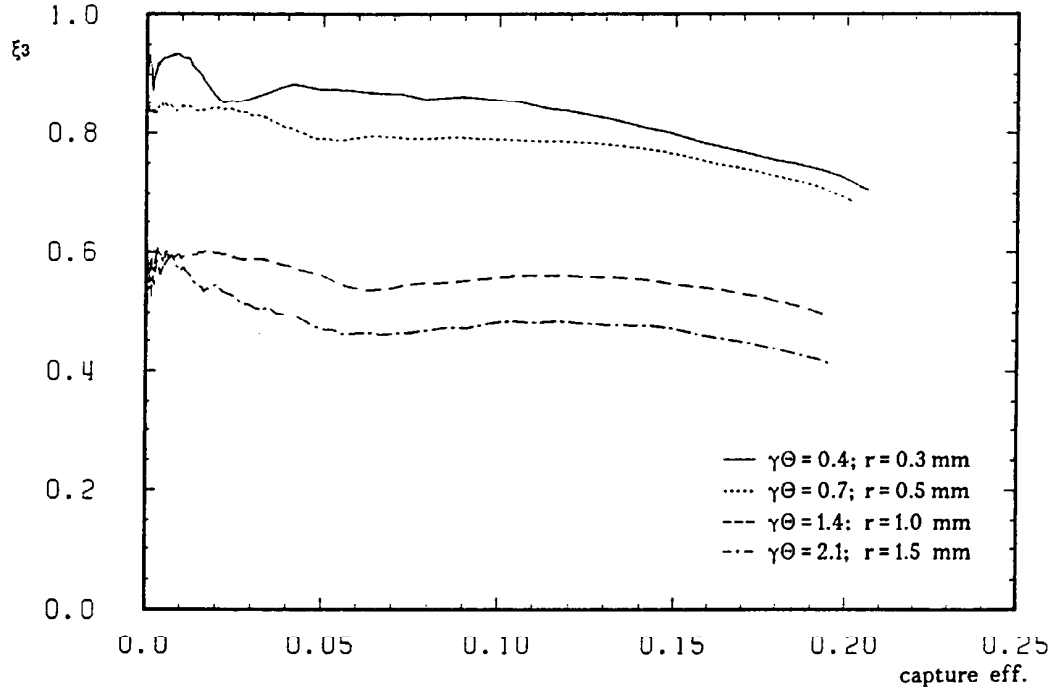

Fig. 2.15 Influence of the scraper angle on the polarization, K = 0.7

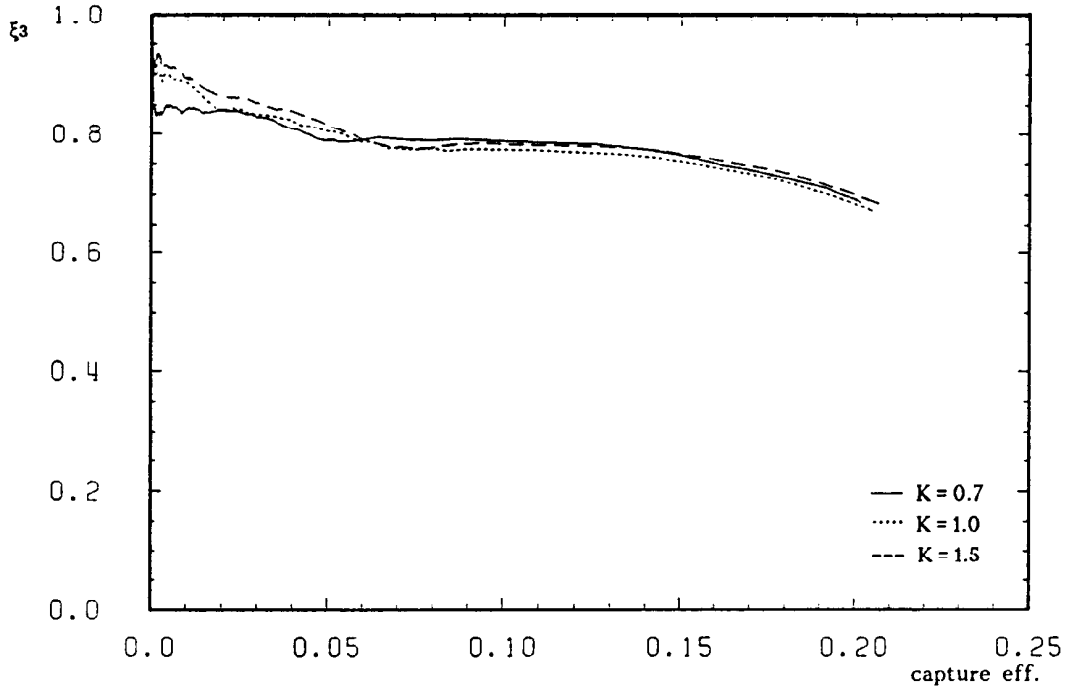

Fig. 2.16 Influence of scaper angle $\gamma\Theta$ = 0.7 for various undulator parameters K on the polarization

In fig. 2.15 the effect of a scraper iris is shown for scraper radii from 0.3 mm to 1.5 mm. The corresponding normalized emission angles $\gamma\Theta$ refer to the middle of the undulator and can be compared with fig. 2.11. For small radii the polarization obtained is roughly independent of the K-value as can be seen from fig. 2.16. The efficiency of the spectroscopic optics is not affected by the scraper. In fig. 2.17 the polarization at maximum capture efficiency is plotted for various undulator parameters.
A polarization of nearly 70%, corresponding to the polarization which we have obtained with a monoenergetic photon beam can be achieved even with a high undulator parameter. However, with increasing undulator parameter more and more photons have to be scraped off. Fig. 2.18 shows the positron yield per meter of undulator versus the undulator parameter for a non-scraped beam and for a scraper angle of $\gamma\Theta / \sqrt{1 + K^2} = 0.5$.
The power deposition in the scraper reaches levels of 80% of the photon beam power at high K-values and small scraper radii. The photon beam power is ~3% of the electron beam power ($L = 100$ m), i.e. ~170 kW and ~400 kW for the S-band and the TESLA approach, respectively.
Since the particle density scales roughly with 1/r, we can assume that the temperature rise in a titanium alloy scraper during a shot is below that in the target. (Remember that the particle density reaches its maximum at a depth of 0.4 X_0; see fig. 1.11.) However, the power deposition is much higher in the scraper than in the target and in addition it is difficult to rotate a scraper, so that the energy has to be lead away between subsequent shots. Hence the collimation has to be done in steps or with a long tapered scraper, in order to provide a large surface for cooling.

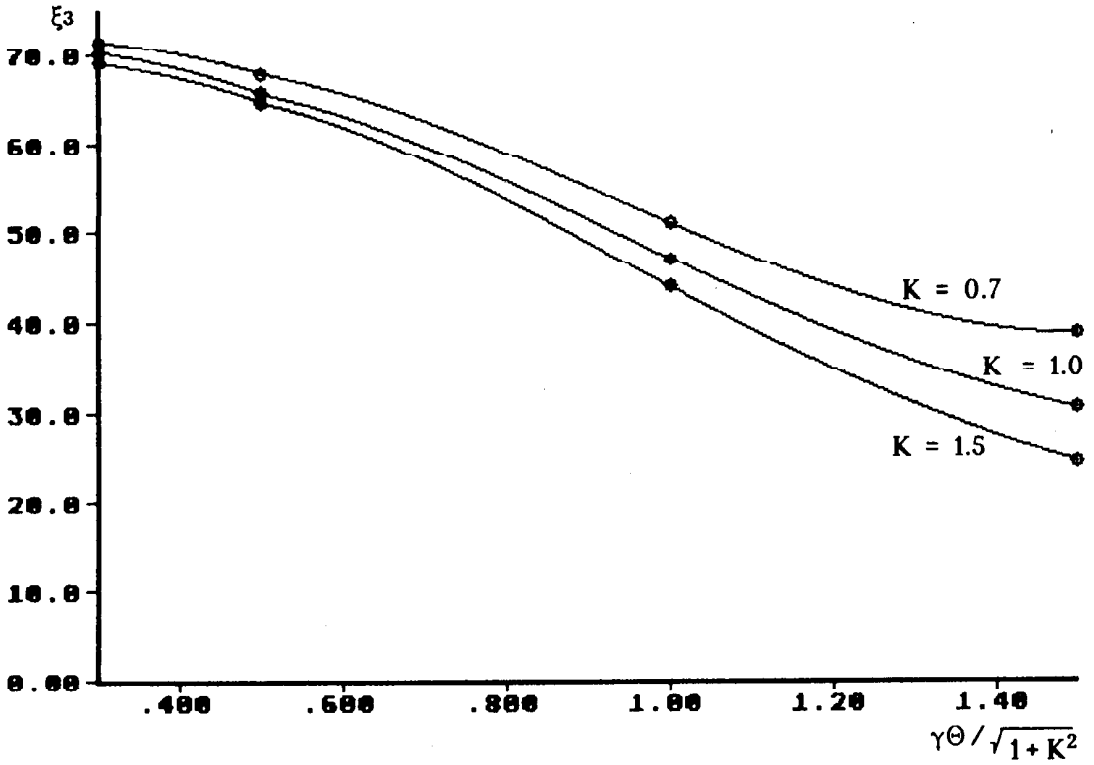

Fig. 2.17 Polarization versus scraper angle for various undulator parameters K

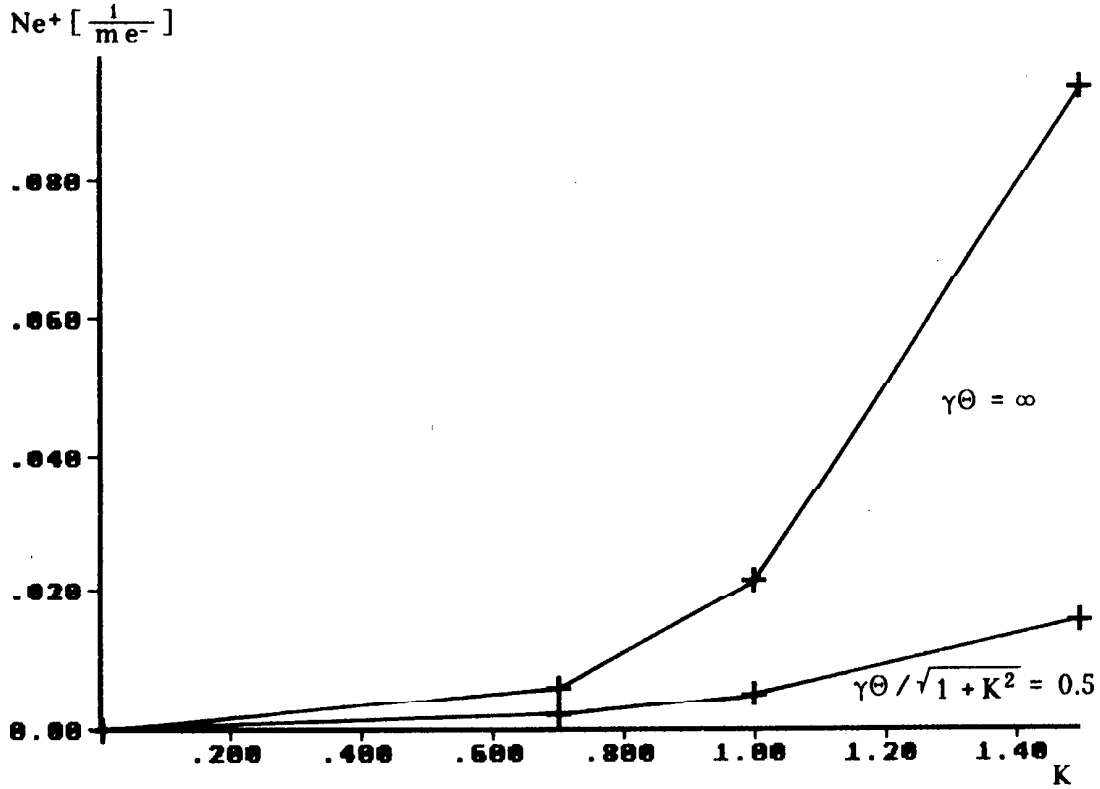

Fig. 2.18 Positron yield with and without scraper

2.7.0 Design parameters of a high intensity, polarized positron source

In order to produce a high number of photons, the undulator has to be very long in case of a small K-value. To suppress near field effects and allow an efficient scraping, the distance between undulator and target has to be even longer ($D \geq L$). Then, however, the spot size of the radiation becomes too large and the capture efficiency will drop. Hence a higher undulator parameter is desirable.
On the other hand the undulator parameter is limited due to technical problems. Higher K-values call for both higher fields and shorter undulator periods if the energy of the first harmonic is to be kept constant. Table 10 compares magnetic fields and undulator periods for various K-values with a fixed energy of the first harmonic of $E_1 = 20$ MeV for a 250 GeV electron beam.

K	B [T]	λ [cm]
0.5	0.23	2.4
0.7	0.38	2.0
1.0	0.72	1.5
1.2	1.06	1.2
1.5	1.76	0.9

Tab. 10 Undulator parameter K, magnetic field B, and undulator period λ for $E_1 = 20$ MeV, $E = 250$ GeV

A. A. Mikhailichenko has investigated various design options for an undulator with small period length and high field [ref. 25]. An attractive solution is an undulator with superconducting coils wound as sketched in fig.1.4.
According to ref. 52 the field on the undulator axis is given by (no iron yoke):

$$B[T] = 2.385 \cdot 10^{-5} \cdot I \cdot \lambda u \left[e^{\frac{-5.68 \cdot r_i}{\lambda u}} - e^{\frac{-5.68 \cdot r_o}{\lambda u}} \right]$$

$r_i / r_o \equiv$ inner/outer radius of the coil

$I \equiv$ current density [A/cm^2]

An axial width of $1/3\,\lambda u$ is assumed for the coil.
We set:

$$e^{\frac{-5.68 \cdot r_o}{\lambda u}} = (1-\varepsilon)\, e^{\frac{-5.68 \cdot r_i}{\lambda u}}$$

$$\varepsilon \leq 1$$

and get:

$$r_o = r_i + \frac{-\ln(1-\varepsilon)}{5.68} \cdot \lambda_u$$

The maximum field is obtained with an infinite outer radius ($\varepsilon = 1$). If we ask for 90% of this theoretical maximum, we find with $\varepsilon = 0.9$:

$$r_o = r_i + 0.4 \cdot \lambda_u$$

In order to optimize the undulator with respect to the yield and with respect to the field dependence as function of λ_u and r_i, we have fitted the yield, given at points (λ_u, B) with a two dimensional function of second order. We found:

$$\begin{aligned} \Upsilon_{e^+}(\lambda_u, B) = & -2.98 \cdot 10^{-3} + 0.022 \cdot B + 1.73 \cdot 10^{-3} \cdot B^2 \\ & + (1.55 \cdot 10^{-3} - 8.82 \cdot 10^{-3} \cdot B - 5.73 \cdot 10^{-3} \cdot B^2) \cdot \lambda_u \\ & + (-3.46 \cdot 10^{-4} + 1.93 \cdot 10^{-3} \cdot B + 2.00 \cdot 10^{-5} \cdot B^2) \cdot \lambda_u^2 \end{aligned}$$

The formula approximates the positron yield per meter undulator (including an assumed capture efficiency of 20%[1]) for a scraper angle of $\Upsilon\Theta/\sqrt{1+K^2} = 0.5$ within the range of $E_i = 10 - 30$ MeV and $K = 0.7 - 1.5$ with an accuracy of a few percent. Since the scraper radius is adjusted according the K-value the polarization varies only slightly around 66% (see fig. 2.17).

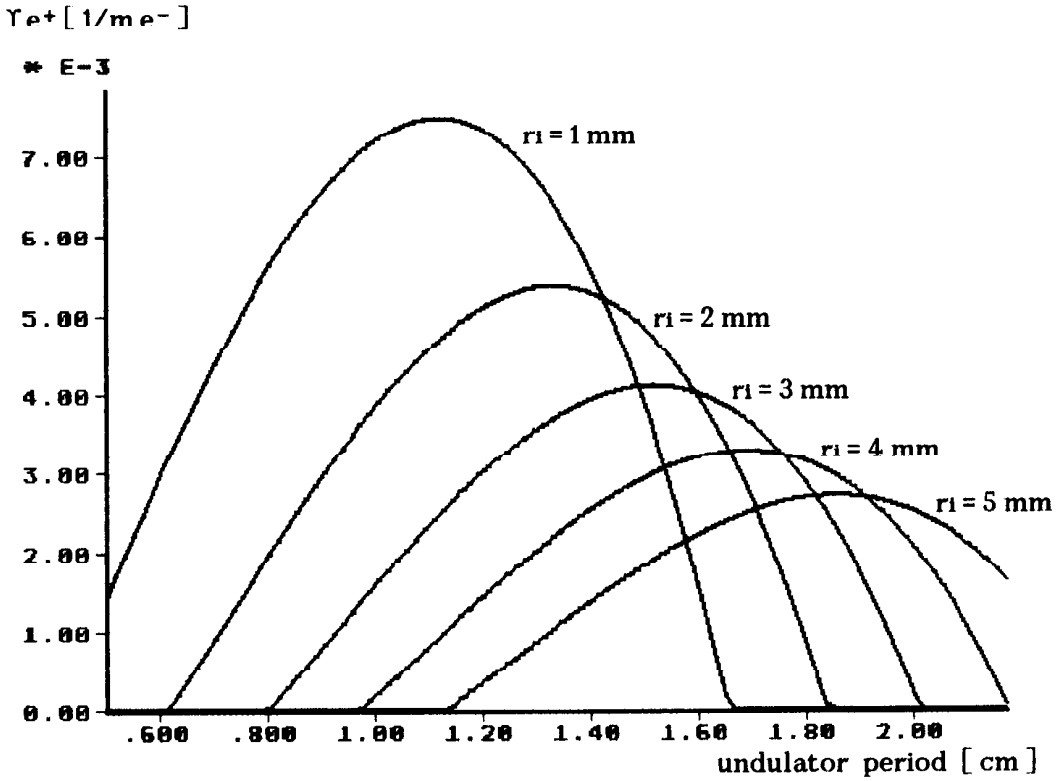

Fig. 2.19a Positron yield per meter undulator versus undulator period; current density $I = 600$ A/mm^2

1 Since the high energy photons are scraped off, the capture efficiency is somewhat higher than in case of the unpolarized source.

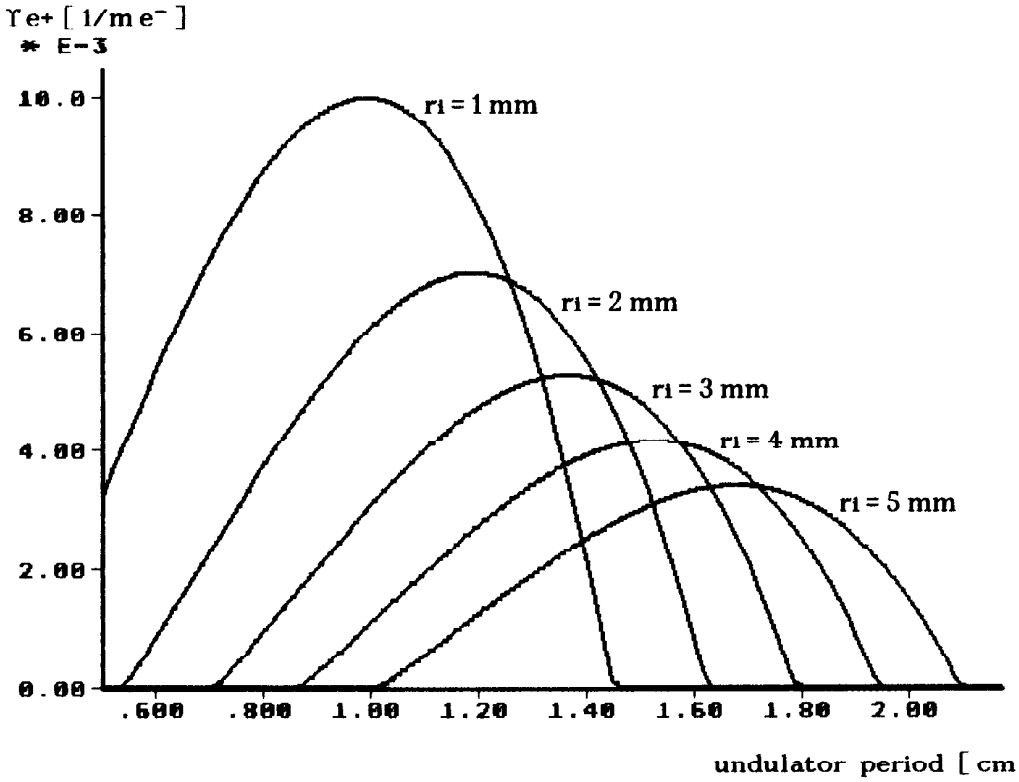

Fig. 2.19b Positron yield per meter undulator versus undulator period; current density I = 900 A/mm^2

We insert:

$$B = \varepsilon \cdot 2.385 \cdot 10^{-5} \cdot I \cdot \lambda u \cdot e^{\frac{-5.68 \cdot r_1}{\lambda u}}$$

and get the yield as function of λu and r_1: $Ye^+(\lambda u, r_1)$.
This function is plotted in fig 2.19a for a current density of 600 A/mm^2 and in fig. 2.19b for a current density of 900 A/mm^2 in the superconducting coils corresponding to 4 K and 2 K temperature, respectively.
Table 11 summarizes the yield Ye^+ at optimum undulator period and corresponding parameters. (The values for K and E_1 are within the range which is covered by the approximated yield function, while they are out of range at points $(\lambda u, r_1)$ far from the optimum.
The maximum yield corresponds to a K-value of 0.9-1.0. In order to maximize the yield we have to choose a small period length and small coil radii.
Apart from technical problems of winding a coil with small radius, we have to worry about operational problems, because the high power electron beam (some mega watts of beam power) has to clear the undulator bore.
Before we can discuss the operational problems connected with a small aperture in more detail, we need some information about the beam optics in the undulator.

r_1 mm	λ cm	Y $\cdot 10^{-3} m^{-1}$	Y^{-1}* m	K	E_1 MeV	B T	x' μrad
	I = 600 A/mm^2		ε = 0.9				
1	1.12	7.43	135	0.90	29.0	0.87	7.4
2	1.34	5.33	188	0.93	23.9	0.74	10.4
3	1.52	4.08	245	0.91	21.4	0.64	12.2
4	1.70	3.26	307	0.91	19.0	0.58	13.0
5	1.87	2.69	372	0.92	17.2	0.53	13.5
	I = 900 A/mm^2		ε = 0.9				
1	0.99	9.99	100	1.0	29.5	1.08	10.0
2	1.19	7.01	143	0.98	25.3	0.88	14.0
3	1.37	5.28	189	0.98	22.2	0.76	15.8
4	1.54	4.16	240	0.98	19.7	0.68	16.6
5	1.69	3.40	294	0.96	18.3	0.61	17.0

* length of undulator without safety margin

Tab. 11 Optimized undulator parameters for various coil radii. x' denotes the geometrical opening angle of the undulator $x' = r_1/L$

We assume an undulator of length L = 200 m, a distance of D = 350 m between the target and the undulator, K = 1 and E_1 = 20 MeV for the following calculations.

Following an argumentation similar to that of the case of near field effects, we expect that the polarization of the photon beam is affected by the electron beam emittance only by virtue of an incoherent mixture of photons emitted into different solid angles. This effect is minimized, if the electron beam is focused onto the target, as proposed also for the unpolarized positron source (see ch. 1.6.0 for details). Hence we have to compare the virtual spot size of the electron beam on the target σ^* with the spot size of the undulator radiation σ_{rad} given by:

$$\sigma_{rad} \simeq \frac{1}{\gamma} \left(\frac{L}{2} + D \right) = 0.9 \text{ mm}$$

Results of numerical simulations are shown in fig. 2.20, where the polarization as a function of the scraper angle is plotted for various beam parameters. The minimum attainable beam width at the entrance of the undulator is $\sigma_e = 0.74$ mm for an emittance of $\varepsilon = 5 \cdot 10^{-10}$ m. (For simplicity we consider round beams.) As can be seen, the polarization is strongly affected. Hence, we have either to increase the beam width to $\sigma_e = 1$ mm, or to decrease the emittance. (For larger emittances the beam width has to be even larger.) With $\varepsilon = 1 \cdot 10^{-10}$ m the beam width can even be reduced to $\sigma_e = 0.5$ mm. The β-function on the target is $\beta^* = 165$ m and $\beta^* = 128$ m for $\varepsilon = 5 \cdot 10^{-10}$ m, $\sigma_e = 1$ mm and $\varepsilon = 1 \cdot 10^{-10}$ m, $\sigma_e = 0.5$ mm, respectively. Hence, the spot size of the electron beam on the target is σ^* = 0.3 mm and 0.11 mm, respectively which has to be

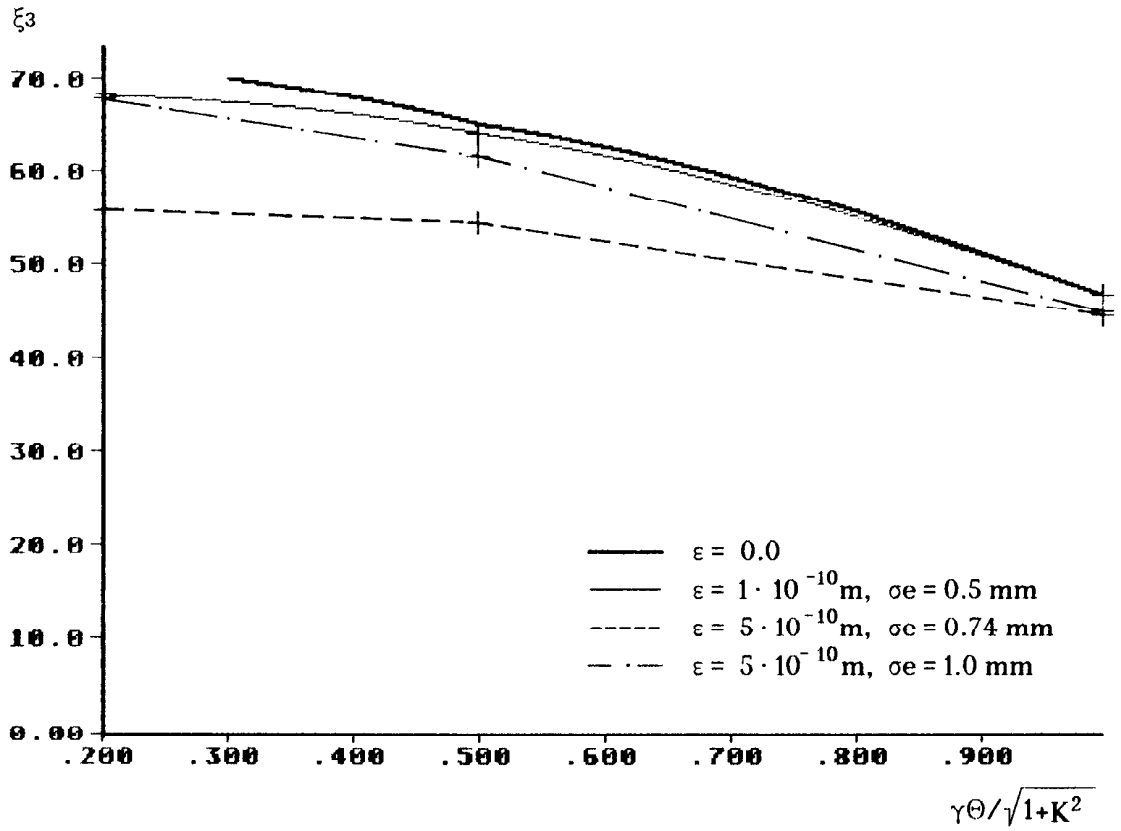

Fig. 2.20 Polarization versus scraper angle for various electron beam emittances ε and beam dimensions in the undulator σe

compared with the spot size of the undulator radiation. We conclude that:

$$\sigma^* \simeq \frac{1}{5}\,\sigma_{rad}$$

has to be fulfilled.

The emittance requirements are obviously much stronger for the polarized source than for the unpolarized source, i.e. by two orders of magnitude in the horizontal plane (compare with ch. 1.6.0). Hence, a more refined optics is necessary to match the disrupted electron beam to the undulator than we have required for the unpolarized source. As already mentioned, R. Brinkmann has designed an optics which collects approximtely 90% of the particles within an emittance of $\varepsilon x \simeq 10^{-9}$ m and $\varepsilon y \simeq 10^{-11}$ m [ref. 30] for TESLA. A similar optics should fulfill the emittance requirements even for the S-band study at a reduced capture efficiency.

We will now discuss the operational problems connected with the small aperture of the helical undulator.

In order to avoid a varying positron intensity, the offset of the photon beam with respect to the axis of the capture optics behind the target has to be

controlled to a level of $\Delta r \leq 0.1$ mm, as in the case of an unpolarized source. This corresponds to an offset in each dimension of the electron beam at the entrance of the undulator of $\Delta x \leq 0.1/\sqrt{2}$ mm or, alternatively, an angular deviation of $\Delta x \leq 0.18/\sqrt{2}$ μrad for D + L = 550 m.
However, due component failure or during start up we have to expect much larger deviations which might penetrate into the undulator and cause damage or at least a quench, if it is not protected.
To avoid this, the maximum allowable anglular deviation for a point like beam on axis is given by:

$$x' = \frac{r_i}{L} \sim r_i * \Upsilon e^{+}(\lambda u, r_i)$$

corresponding to an error emittance of $\varepsilon = x'^2 \cdot \beta$.
Using the Courant-Snyder invariant we can set:

$$\gamma \hat{x}^2 + 2\alpha \hat{x}\hat{x}' + \beta \hat{x}'^2 \leq \varepsilon = x'^2 \cdot \beta$$

with $\gamma\beta - \alpha^2 = 1$

$\hat{x}$ and $\hat{x}'$ denote the accumulated orbit errors at the entrance of the undulator. Since we focus the beam onto the target, the optical functions at the distance s from the target are given by:

$$\beta = \frac{s^2}{\beta^*} + \beta^*$$

$$\alpha = \frac{s}{\beta^*}$$

$$\gamma = \frac{1}{\beta^*}$$

Deviations in x and x' can be caused by various objects at various points in the beam transport line. In the average, contributions in x and x' to the error emittance are equal. With:

$$\gamma \hat{x}^2 = \frac{\hat{x}^2}{\beta^*} = \left(\frac{s^2}{\beta^*} + \beta^*\right)\hat{x}'^2 = \beta \hat{x}'^2$$

we get:

$$\hat{x} < \frac{1}{\sqrt{2}}\, x' \sqrt{\beta^{*2} + s^2}$$

$$\hat{x}' < \frac{1}{\sqrt{2}}\, x'$$

With geometrical opening angles of the undulator taken from table 11 the angular deviations $\hat{x}'$ cover the range from 5 μrad up to 11 μrad, while the corresponding offsets $\hat{x}$ extend from 3 mm up to 6 mm (β^* = 140m, s = 550m). (Since the undulator length was 200 m in our calculations, these numbers are only valid for r_i = 1 - 3 mm. For larger apertures a longer undulator is required, see tab. 11.)

Thus the required aperture of a protection system is dominated by orbit offset requirements rather than by angular orbit requirements.
In table 12 parameters of a highly polarized, high intensity source are summarized. (Parameters of the target and the capture optics are similar to the unpolarized source.)
The calculations in this section are only valid for an undulator without an iron yoke. Since the optimum fields are comparatively low, the situation might be improved by means of an iron yoke. This requires, however, numerical calculations to derive the dependence of the field amplitude on the undulator period and the coil radius.

inner coil radius	2 - 3 mm
current density	900 A/mm^2 at 2 K
undulator period	~1.4 cm
undulator field	~0.8 T
undulator parameter K	0.98
length of undulator	140 - 190 m
opening angle r_i/L	< 15 μrad
max. polarization*	66 %
power in photon beam	~4 % of electron beam power
max. power deposition in collimator	~80 % of P_γ

* not included: depolarization due electron beam emittance

Tab. 12 Parameters of a highly polarized, high intensity positron source

2.8.0 Alternative sources for circular polarized photons - The asmmetric wiggler and the elliptical wiggler

The helical undulator represents, from the physical point of view, the optimum device to produce monoenergetic, highly circularly polarized photons, but from the technical point of view has its difficulties. We will now discuss a device which is more easy to realize, since it is based on permanent magnet technology, but will not produce monoenergetic photons.
The circular polarization of the radiation of a bending magnet can be approximated by [ref. 53]:

$$\xi_3 = \frac{F^+ - F^-}{F^+ + F^-}$$

with

$$F^{\pm} = \frac{7 + 12\,\gamma\Theta^2}{2\,(1+\gamma\Theta^2)^{7/2}} \pm \frac{32\,\gamma\Theta}{\pi\sqrt{3}\,(1+\gamma\Theta^2)^3}$$

In fig. 2.21 the circular polarization and the radiation intensity is plotted versus the observation angle $\gamma\Theta$ (perpendicular to the bending plane).

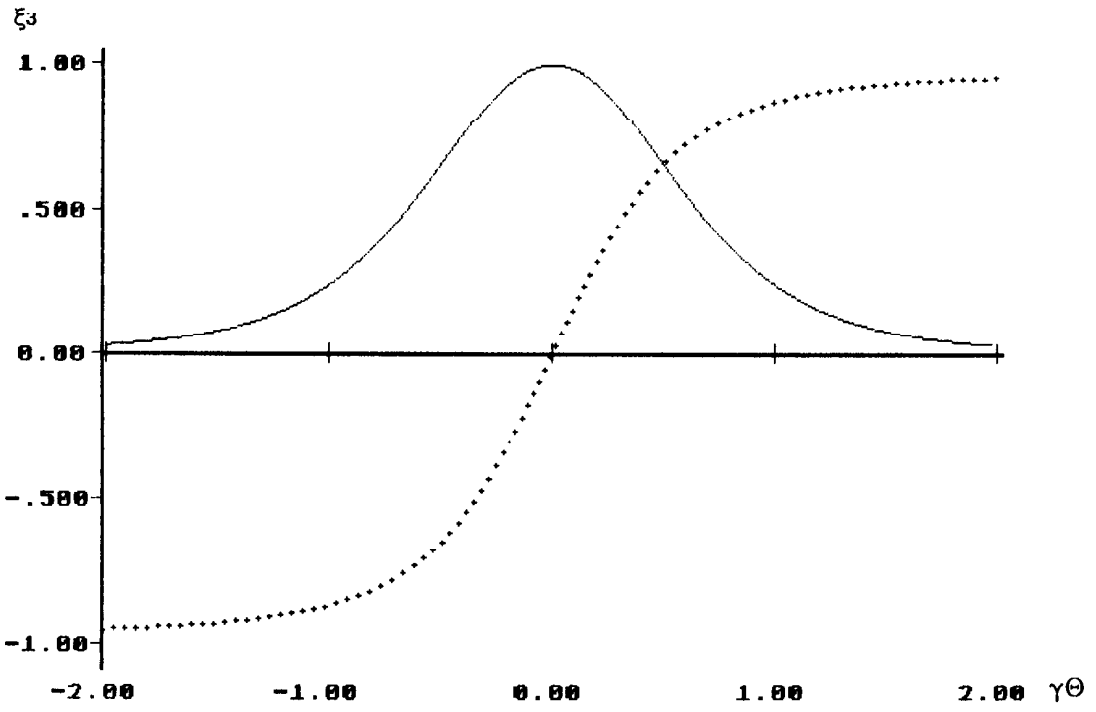

Fig. 2.21 Circular polarization (dotted line) and intensity (solid line, in arbitrary units) of the radiation of a bending magnet versus observation angle $\gamma\Theta$

The sign of the polarization is reversed if the magnetic field is reversed. Hence the circular polarization of a planar wiggler with its alternating magnetic fields is zero.

Two devices have been proposed to utilize the circular polarization of a bending magnet: the asmmetric wiggler and the elliptical wiggler [ref. 54, 55].

In the asymmetric wiggler short strong magnets alternate with weak, long magnets. Since the radiation from the weak magnets has a lower intensity and a shifted spectrum, it cannot compensate the radiation from the strong magnets. However, the mean field amplitude of this device is only small and hence the total photon intensity per meter of wiggler is reduced.

The elliptical wiggler is basically the superposition of a strong horizontal planar wiggler ($K_H \simeq 10$) with a weak vertical planar wiggler ($K_V \simeq 1$). The purpose of the vertical wiggler is not to produce additional radiation, but to sweep the radiation of the horizontal wiggler over the range of $\gamma\Theta = \pm 1$. With a phase shift of 90° between horizontal and vertical plane, the main intensity of the positive horizontally bending magnets is radiated into the upper half plane, while the radiation of the negative bending magnets is radiated into the lower half plane. On the axis circular polarized radiation with equal sign adds up.

To estimate the polarization of the positrons formed by radiation of an elliptical wiggler we consider the radiation of the upper half plane of a bending magnet. As in the case of a helical undulator ξ_3 is given by:

$$\xi_3 = \frac{2\,Ix\,Iy}{Ix^2 + Iy^2}$$

with

$$Ix(E) = \left[\frac{10^6 e^3}{4\pi\varepsilon_0 \hbar^2 c^2} * \frac{E}{2\pi^2 \gamma^2 Ec}\right]^{1/2} * (1+\gamma\Theta^2) \; * \; K_{2/3}\left(\frac{1}{2}\frac{E}{Ec}(1+\gamma\Theta^2)^{3/2}\right)$$

$$Iy(E) - i\left[\frac{10^6 e^3}{4\pi\varepsilon_0 \hbar^2 c^2} * \frac{E}{2\pi^2 \gamma^2 Ec} * (1+\gamma\Theta^2)\right]^{1/2} * \gamma\Theta * K_{1/3}\left(\frac{1}{2}\frac{E}{Ec}(1+\gamma\Theta^2)^{3/2}\right)$$

Ec = critical energy of radiation

By means of a scraper the mean polarization can be increased, as can be seen from fig. 2.21.

Fig. 2.22 shows the photon spectrum integrated over the solid angle for various scraper angles $\gamma\Theta_{min}$. ($\gamma\Theta_{min} = 0$ refers to the integration over the upper half plane of the radiation, see fig. 2.21.)

The corresponding polarization is plotted in fig. 2.23.

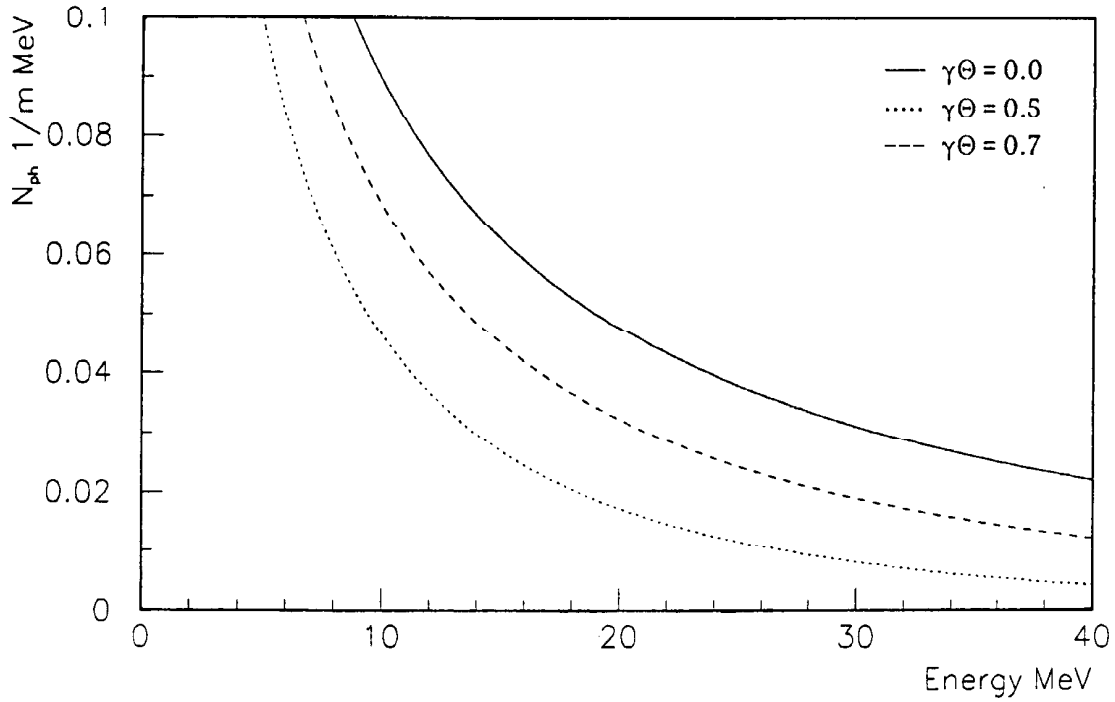

Fig. 2.22 Photon spectrum of a bending magnet for various scraper angles, compare with fig. 2.21

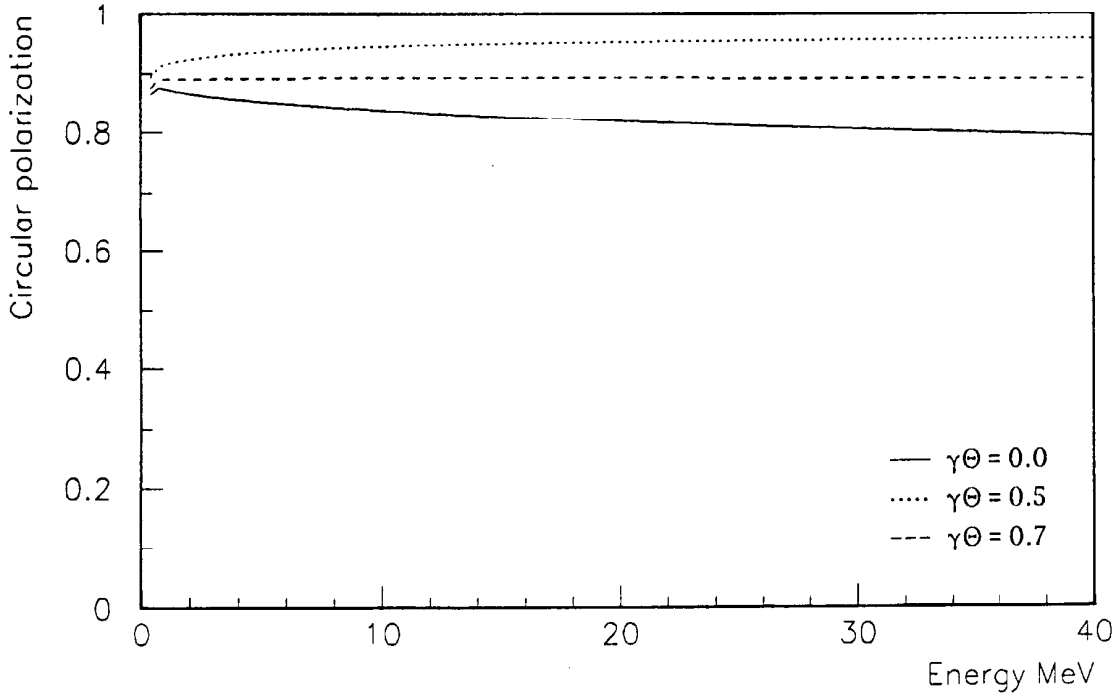

Fig. 2.23 Polarization versus energy for synchrotron radiation for various scraper angles, compare with fig. 2.21

With increasing scraper angle the polarization reaches a high level over the whole energy range. Since the high energy photons are emitted with only small opening angles more high energy photons than low energy photons are absorbed in the scraper. Hence the positron yield decreases even more strongly with the scraper angle than the photon number does.
Tab. 13 compares the number of photons, the positron yield and the polarization for various scraper angles $\gamma\Theta$min. Even with large scraper angles the polarization of positrons formed by monoenergetic photons is not reached, since high energy photons produce low or even negatively polarized positrons at low energies.

$\gamma\Theta$min	Nph m^{-1}	Nph %	Ne^+ m^{-1}	Ne^+ %	P %
$-\infty$	9.0	100	0.4	100	0
0	4.5	50	0.2	50	37
0.5	3.2	36	0.09	24	55
0.7	2.8	31	0.06	16	58

Tab. 13 Photon number, positron yield and positron polarization from radiation of a bending magnet for various scraper angles.

The radiation of an elliptical wiggler is not as highly polarized as the radiation of a simple bending magnet, because the vertical deflection has the form of a sine wave and not the form of a step function. Hence, in order to obtain a higher polarization, a larger fraction of the photons have to be scraped off and the yield as function of the polarization is even lower.
The photons produced in the elliptical wiggler form an elliptical spot size with aspect ratio K_V/K_H which does not match to the axial-symmetric acceptance of the matching device. In order to reduce near field effects which might be stronger in case of the elliptical wiggler since no line spectrum is emitted and to reduce the thermal stress in the target, the distance D between wiggler and target has to be sufficiently large. Then the horizontal width of the spot size given by $K_H/\gamma\ (D+L/2)$ is too large and the capture efficiency drops.
Taking everything into account we conclude that an elliptical wiggler can be utilized only for a positron source with a lower polarization level and eventually reduced yield. However, since it takes only a small investment to modify the planar wiggler of the unpolarized source to obtain an elliptical wiggler, this might be an attractive way to do first experiments with polarized positrons and get experience with a polarized positron source.

2.9.0 Summary and outlook

In this work we have attacked some problems which have to be considered in more detail before a positron source based on wiggler or undulator radiation might be realized.
Concerning the unpolarized high intensity source, the advantages of the soure based on wiggler radiation are obvious: Due to the smaller positron beam emittance the capture efficiency can be considerably improved, while the application of a titanum alloy as target material allows a higher particle density in the target.
The requirements of the DESY/THD study ($3.6 \cdot 10^{12}$ positrons with 50 Hz rep. rate) can be achieved with a source based on wiggler radiation. In addition a rotating target wheel will be required, in order to meet the demands of TESLA ($4 \cdot 10^{13}$ positrons with 10 Hz rep. rate). A planar wiggler of roughly 40 m length is necessary, to produce 2 positrons per incident electron. (Factor 2 as safety margin.)
More detailed investigations are needed to solve problems connected with the electron beam after the interaction. An optics to guide the particles out of the interaction region and to transport them through the wiggler has to be developed in detail and the stability of the source has to be studied in more detail. In addition a protection system for the wiggler should be investigated. This is of even greater interest for the polarized source, where a superconducting undulator might be used.
Concerning the polarized source, the results of this work might be summarized as follows: From the physical point of view a polarized source is possible and useful, but it requires some effort for its technical realization. Hence one of the next steps should be to study the technical feasibilty of a short period helical undulator. We refer here to the work of A. A. Mikailichenko [ref. 25], who invented the polarized positron source together with V. E. Balakin and has investigated various types of helical undulators.
In addition the spectrum and angular dependence of alternative photon sources like the elliptical wiggler should be studied in more detail.
With a helical undulator of ~150 m length a polarization above 60% can be achieved. Since only the on-axis part of the undulator radiation is circularly polarized, the photon beam has to be collimated, in order to increase the polarization.
The results for polarized electromagnetic showers which we have derived by means of an extended version of the Monte-Carlo program EGS 4 might be verified with an experiment based on Compton back-scattering:
Low energy circular polarized photons of a laser can be converted into high energy circular polarized photons by Compton scattering with high energy electrons. If for example photons of a carbon dioxide laser (E_L = 0.117 eV) collide with the electron beam of DORIS (E = 3.5 GeV), the back-scattered photons reach an maximum energy of:

$$E\gamma = \frac{4\gamma^2 E_L}{1 + \frac{4\gamma E_L}{m_e c^2}} = 21.8 \text{ MeV}$$

Since the field of a helical undulator in the rest frame of the electron is equivalent to the field of a circularly polarized, monochromatic electromagnetic wave, the spectrum of back-scattered photons is nearly equivalent to the first harmonic of helical undulator radiation (fig. 2.9). Hence the radiation of a helical undulator can also be regarded as a Compton back-scattering process of virtual photons (Weizsäcker-Williams-Method). Radiation at higher harmonics is connected to multi-photon effects which could also be observed in back scattered laser light if a laser of extreme intensity would be available.
The back scatted photons can be converted into positrons in a thin target and the measured polarization can be compared with a prediction of the Monte-Carlo program.

Acknowledgements

I would like to thank J. Roßbach for his support, encouragement, numerous helpful discussions and for his continued interest in the progress of my work.

I am indebted to a lot of people at DESY for stimulating discussions, kind help and co-operation. Among these are:
M. Böge, R. Brinkmann, O. Brüning, W. Decking, A. Febel, J. Feikes, K. Heinemann, N. Holtkamp, A. Pauluhn, J. Pflüger.

Special thanks to G. A. Voss for his support and various stimulating conversations.

Finally, I am grateful to D. Barber, E. Lohrmann, J. Roßbach and S. Wipf for the careful reading of the manuscript and for several useful suggestions.

References

[1] J. Roßbach *An Overview of Linear Collider Plans,* Invited talk given at the 1992 Linear Accelerator Conference, Ottawa, DESY M-93-01 (1992)

[2] J. Roßbach *Positron recycling in high energy linear colliders,* Nuc. Inst. and Meth. A309, (1991) 25-31

[3] K. Flöttmann, J. Roßbach *Emittance Damping considerations for TESLA* DESY 93-023 (1993)

[4] J. Roßbach *A positron source for TESLA,* unpublished, presented at LC92, Garmisch-Partenkirchen (1992)

[5] K. Flöttmann, N. Holtkamp, J. Roßbach *Positron source considerations for TESLA,* DESY TESLA 93-21 (1993)

[6] DESY/THD Study Group *Status Reprt of a 500 GeV S-Band Linear Collider Study,* DESY-91-153 (1991)

[7] SLAC *Linear Collider Conceptual Design Report,* SLAC 229 (1980)

[8] E. M. Reuter, J. A. Hodgson *3D Nummerical Thermal Stress Analysis of the High Power Target for the SLC Positron Source,* SLAC-PUB-5370 (1991)

[9] V. E. Balakin, A. A. Mikhailichenko *The Conversion System for obtaining high polarized electrons and positrons,* Preprint INP 79-85 (1979)

[10] U. Amaldi, C. Pellegrini *Energy recovery in superconducting colliding linacs without particle recovery,* Proc. 2nd ICFA Workshop on Possibilities and Limitations of Accelerators and Detectors, Les Diablerets (1979)

[11] K. Flöttmann, J. Roßbach *A High Intensity Positron Source for Linear Colliders,* DESY M-91-11 (1991)

[12] K. Flöttmann, J. Roßbach *A High Intensity Positron Source for Linear Colliders,* High Energy Accelerator Conference, Hamburg (1992) 142-144

[13] R. B. Neal et.al. *The Stanford Two-Mile Accelerator,* W. A. Benjamin Inc.; New York (1968) 711

[14] G. Z. Molière *Theorie der Streuung schneller geladener Teilchen II. Mehrfach und Vielfach Streuung,* Z. Naturforscher 3a (1948)

[15] Particle Data Group *Review of Particle Properties,* Physics Letters B239 (1990)

[16] J. D. Jackson, *Klassische Elektrodynamik*, W. de Gruyter (1982)

[17] B. M. Kincaid *A short-period helical wiggler as an improved source of synchrotron radiation*, Journal of Applied Physics, Vol. 48; No 7 (1977) 2684-2691

[18] W. Nelson, H. Hirayama, D. Rogers *The EGS4 Code System*, SLAC-265 (1985)

[19] R. D. Walz, private communication

[20] R. H. Helm *Adiabatic Approximation for Dynamics of a Particle in the Field of a Tapered Solenoid*, SLAC-4 (1962)

[21] R. Brinkmann *A Study of Low-Emittance Damping Ring Lattices*, DESY M-90-09 (1990)

[22] M. N. Wilson, K. D. Srivastava *Design of Efficient Flux Concentrators for Pulsed High Magnetic Fields*, The Review of Scientific Instruments; vol. 36, 8 (1965) 1096-1100

[23] A. V. Kulikov, S. D. Ecklund, E. M. Reuter *SLC Positron Source Pulsed Flux Concentrator*, Particle Accelerator Conference, San Francisco (1991) Vol. 3, 2005-2007

[24] A. Kulikov, private communication

[25] A. A. Mikhailichenko *Conversion System for obtaining Polarized Electrons and Positrons at High Energy*, Novosibirsk INP (1986) Thesis (In Russian)

A. D. Bukin, A. A. Mikhailichenko *Optimized target strategy for polarized electrons and positrons production for linear collider*, Budker INP 92-76, Novbosibirsk (1992)
E. G. Bessonov, A. A. Mikhailichenko *Some aspects of undulator radiation forming for conversion system of the linear collider*, Budker INP 92-43, Novosibirsk (1992)

[26] H. Braun *Application of Plasma Lenses in Positron Sources*, European Particle Accelerator Conference, Berlin (1992) 1650-1652

[27] R. Brinkmann *Optimization of a Final Focus for large Momentum Bandwidth*, DESY M-90-14 (1990)

[28] P. Sievers, M. Höfert *A Mega Watt Electron Positron Conversion Target - A Conceptual Design*, European Particle Accelerator Conference, Rom (1988) 133-135

[29] E. M Reuter et. al. *Mechanical Design and Development of a High Power Target System for the SLC Positron Source*, Particle Accelerator Conference, San Francisco (1991) Vol. 3, 1999-2001

[30] R. Brinkmann, private communication

[31] J. E. Clendenin *High-Yield Positron Systems for Linear Colliders*, SLAC-PUB-4743 (1989)

[32] P. Krejcik, V. Ziemann *A simple Model for SLC Positron Stability Issues*, SLAC-PUB-5725 (1992)

[33] B. L. Berman, S. C. Fultz *Measurements of the giant dipole resonance with monoenergetic photons*, Reviews of Modern Physics, Vol. 47, No. 3 (1975); 713-761

[34] M. Barbier, A. Copper *Estimate of Induced Radioactivity in Accelerators*, CERN 65-34 (1965)

[35] W. R. Nelson, R. A. Shore *Pi-Decay Muons from the SLC Positron Source*, SLAC CN-300 (1985)
W. R. Nelson, R. C. McCall *Additional Muon Calculations for the SLC Positron Source*, SLAC CN-295 (1985)

[36] F. Ciocci, G. Dattoli, K. Flöttmann, J. Roßbach *Undulator-Wiggler Radiation and Electron Beam Distribution*, DESY M-93-03 (1993)

[37] C. Prescott *Experience with Cathodes for Polarized Guns*, presented at Workshop for RF Guns & TESLA Collaboration Meeting, FNAL March 8-12, (1993)

[38] JLC Group *JLC I*, KEK Report 92 16 (1992)

[39] J. M. Jauch, F. Rohrlich *The Theory of Photons and Electrons*, Springer (1976)

[40] R. A. Beth *Mechanical Detection and Measurement of the angular Momentum of Light*, Physical Review 50, 115 (1936)

[41] W. H. McMaster *Polarization and the Stokes Parameters*, Journal of Physics 22, 351 (1954)

[42] W. H. McMaster *Matrix Representation of Polarization*, Reviews of Modern Physics 33, 8 (1961)

[43]H. H. Nagel *Elektron-Photon-Kaskaden in Blei: Monte-Carlo Rechnungen für Primärelektronenenergien zwischen 100 und 1000 MeV,* Zeitschrift für Physik 186, 319 (1965)

[44]Y. Namito, W. R. Nelson *The EGS 4 Code System: Solution of Gamma-Ray and Transport Problems,* SLAC-PUB 5193 (1990)

[45]T. M. Jenkins, W. R. Nelson, A. Rindi (Editors) *Monte Carlo Transport of Electrons and Photons,* Plenum Press, New York (1988)

[46]H. Olsen, L. C. Maximon *Photon and Electron Polarization in High-Energy Bremsstrahlung and Pair Production with Screening,* Physical Review 114, 887 (1959)

[47]H. Olsen. L. C. Maximon *Electron and Photon Polarization in Bremsstrahlung and Pair Production,* Physical Review 110, 589 (1958)

[48]H. Davis, H. A. Bethe, L. C. Maximon *Theory of Bremsstrahlung and Pair Production. II. Integral Cross Section for Pair Production,* Physical Review 93, 788 (1954)

[49]H. W. Koch, J.W. Motz *Bremsstrahlung Cross-section Formulas and Related Data,* Reviews of Modern Physics 31, 920 (1959)

[50]L. D. Landau, E. M. Lifschitz *Lehrbuch der theoretischen Physik, Band IV,* Akademie Verlag Berlin (1980)

[51] F. W. Lipps, H. A. Tolhoek *Polarization Phenomena of Electrons and Photons. I General Method and Application to Compton Scattering,* Physica XX, 85 (1954)
F. W. Lipps, H. A. Tolhoek *Polarization Phenomena of Electrons and Photons II Results for Compton Scattering,* Physica XX, 395 (1954)

[52]J. P. Blewett, R, Chasman *Orbits and fields in the helical wiggler,* Journal of Applied Physics, 48, (7) 2692 (1977)

[53]I. M. Ternov, V. V. Mikhailin, V. R. Khalilov *Synchrotron Radiation and Its Applications,* harwood academic publishers (1985)

[54]H. Onuki, N. Saito, T. Saito *Undulator generating any kind of elliptically polarized radiation,* Appl. Phys. Let. 52 (3) 173 (1988)

[55]V. I. Alekseev, E. G. Bessonov *On some methods of generating circularly polarized hard undulator radiation,* Nuc. Instr. Meth. A308 140 (1991)

[56]M. James, R. Donahue, R. Miller, W.R. Nelson *A new target design and capture strategy for high-yield positron production in electron linear colliders*, SLAC-PUB 5215 (1990)

[57]*The status of positron beam of BEPC linac*, BIHEP-A-90-92 (1990)

[58]J. H. Hubbell, H. A. Gimm, I. J. Øverbø *Pair, Triplet, and total atomic cross sections for photons*, J. Phys. Chem. Ref. Data 9 No. 4 (1980) 1023

[59]H. Messel, D. F. Crawford *Electron-Photon Shower Distribution Function Tables for Lead, Copper and Air Absorbers*, Pergamon Press (1970)

[60]J. Pflüger, private communication

[61]K. Halbach, J. Phys., Coll. C1. Suppl. no 2, vol. 44 (1983)